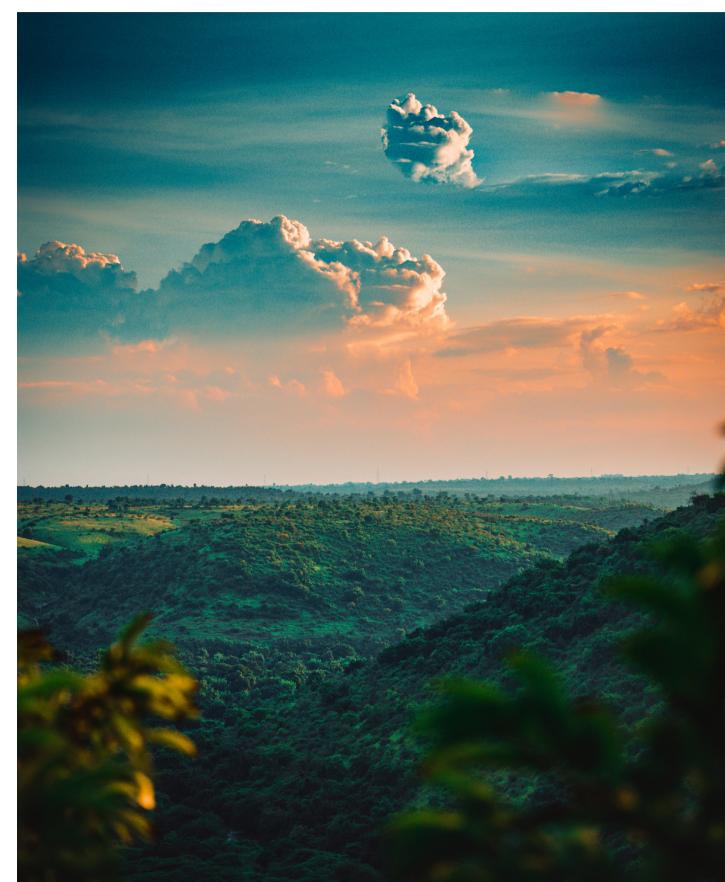# Assessment of the GPM IMERG and CHIRPS precipitation estimations for the steppe region of the Crimea

Victor F. Popovych (iD)

Research Institute of Agriculture of Crimea, e-mail: water@crimea.com

Ielizaveta A. Dunaieva (iD)

Research Institute of Agriculture of Crimea, e-mail: water_crimea@hotmail.com

## Abstract

This paper compares the spatial distribution datasets on monthly precipitation totals derived from the Famine Early Warning System Network FEWS NET service (CHIRPS 2.0 product) and the International Mission of the Global Precipitation Measurement GPM (IMERG v06 product) with ground-based observations of a stationary weather stations located in the steppe region of the Crimean Peninsula in order to assess the representativeness of the precipitation spatial distribution and the applicability of the datasets for water balance calculations and agricultural crop dynamics modeling. A close convergence was observed between the estimated monthly precipitation totals and the precipitation gauge data during the study period (January 2017 – July 2020), with mean correlation coefficients of 0.75 and 0.73 for the GPM IMERG and CHIRPS, respectively. Both products generally overestimated the precipitation values compared to the measured data, with GPM IMERG (final run) exhibiting the greatest overestimations (1.3-2.1 times the weather station values). Our results demonstrate the requirement of GPM-derived precipitation estimations (particularly those from the GPM_3IMERDL v06 daily accumulated late run dataset) to be additionally verified and calibrated based on data from regional weather stations or the CHIRPS 2.0 product (if available).

## 1. Introduction

The amount of precipitation over a certain period of time is the principle limiting factor for crops growing in rainfed agriculture conditions across arid zones. The level of initial moisture content in a particular field (at sowing or seedling emergence) is typically employed as an initial parameter in crop modeling and is determined via field surveys (estimated moisture from soil samples or soil moisture sensors), water balance calculations based on the agrohydrological modeling of the preceding period and remote sensing (RS) data. The spatial resolution of the data services that provide soil moisture information from the upper 3-5 cm soil layer and the layer up to 1 m are currently relatively low, at approximately 25 × 25 km and 10 × 10 km respectively, with data delays from 3 days up to 3 months (Karthikeyan et al. 2017; Yee et al. 2017). Such resolutions allow for the application of the datasets in global modeling, but not for their direct usage in the monitoring and forecasting of tasks in the field. Furthermore, in arid zones, particularly in rainfed conditions, precipitation can be highly variable, the measurement accuracy of which, its spatial and temporal variation, often determines the accuracy of water balance calculations and crop growth simulation results.

One of the most significant achievements of the last two decades in global precipitation measurements has been the Tropical Rainfall Measuring Mission (TRMM) (Liu et al. 2012), a joint project between NASA and the Japan Aerospace Exploration Agency (JAXA). TRMM was originally intended to run for 3 years, yet it was deployed for more than 15 years (1997-2015). During this mission, many developments, basic algorithms and global approaches were determined to assess the interrelation of the atmospheric processes connected with the water cycle, including the application of microwave radiometers for precipitation measurements (Ebert et al. 2007; Huffman et al. 2007; Liu, Zipser 2015). Despite the significant raster size of the precipitation fields (spatial resolution 0.25° or approx. 500 km² for the steppe territory of the Crimean Peninsula, with a temporal resolution of 3 hours), numerous studies have been performed to assess the accuracy of satellite-derived precipitation data (Chokngamwong, Chiu 2008; Scheel et al. 2011; Chen et al. 2020). A particularly important area of research is the application of satellite data to solve hydrological tasks (i.e., river water resource management) using the basin approach (Kidd et al. 2009; Liu et al. 2015).

The scientific and technological developments of the TRMM mission were subsequently employed during the preparation of the new Global Precipitation Measurement (GPM) mission (Hou et al. 2014), which began in 2014. The satellites and data integration methods used in this mission increased the spatial and temporal accuracy of the data, with corresponding resolutions of 0.1° and 30 min, respectively (Wang et al. 2018). This spatial resolution (grid area 85.8 km²) is comparable to the average area of a rural settlement in the steppe Crimea (95 km²) and exceeds the average area per stationary weather station in the Crimea (i.e., on an area of approx. 1,700 km²). This allows for (considering data availability), more than 20 additional geo-referenced precipitation estimations averaged for the area of each grid across the central Crimea district.

Primary raster precipitation data decomposition using data from satellite imagery was developed within the Famine Early Warning System Network (FEWS NET) project and can represent fields of estimated precipitation distributions with a raster size of 0.05° (Funk et al. 2014). This spatial resolution surpasses that of the GPM mission (GPM IMERG dataset). The technology has been developed since 1999 by scientists from the University of California in collaboration with the U.S. Geological Survey (USGS) in order to produce precipitation geo-referenced grids, which are particularly important in sparse data regions. The current version of the methodological approach includes data from weather stations and precipitation gauge posts, spatial variation modelling of precipitation interrelated with the terrain, and data from the satellite monitoring of precipitation. This methodology is primarily focused on the monitoring and forecasting periods of severe drought or floods in order to develop measures to mitigate their impact. Its application range is wide and the supported geospatial database of numerous meteorological parameters, including precipitation, continues to be verified in various regions across the world (Funk et al. 2015; Paredes-Trejo et al. 2017; Dinku et al. 2018; Saeidizand et al. 2018).

Multiple approaches are used to test the Integrated Multi-satellitE Retrievals for GPM (IMERG) and FEWS – the Climate Hazards Group InfraRed Precipitation with Station (CHIRPS), including direct comparisons with ground-based data on measured precipitation (Ning et al. 2016; Nashwan et al. 2019;

Satgé et al. 2019); cross-comparisons with other products and ground-based data (Wang et al. 2018; Beck et al. 2019; Xiao et al. 2020); and indirect estimations obtained by assessing the accuracy of runoff models (Pang et al. 2020). The generalized analysis of these publications demonstrates that in most cases, several factors (topographic features, wet or arid regions, winter or summer periods, frequency of extreme precipitation events, etc.) prevent the selection of the optimal database or methodology (Tang et al. 2020; Xiao et al. 2020).

The technologies for remote precipitation measurements are constantly improving, with sampling times of 30 min (and more) and high spatial resolutions of 0.05-0.1°, allowing their application in seasonal planning and regional analysis tasks, as well as their integration with additional ground-based observations for technological decisions at the field level. The necessity of such information is primarily caused by the low number of stationary and automated weather stations in some regions, as well as the practical impossibility of obtaining regular spatial data of measured precipitation from "field" precipitation gauges (particularly in winter with snowfall).

The aim of this study is to compare the accuracy of spatial field precipitation estimations obtained via the GPM IMERG and FEWS CHIRPS products, with gauge-based precipitation data employed for spatial agro-technological monitoring and planning. We hypothesize the potential difference in the relationship between the precipitation data of the RS products and the ground observations of the weather stations, which have different levels of data accessibility for end users (free open access or limited by price, continuity, etc.).

The level of applicability of the products for agricultural areas within the steppe region of the Crimean Peninsula is demonstrated by comparing the usage of gauge precipitation data from weather stations, GPM mission data (GPM IMERG v06 products – GPM_3IMERGM, final run and GPM_3IMERGDL late run datasets) and the early warning system of extreme situations FEWS NET (CHIRPS 2.0 product).

## 2. The study area

The Crimean Peninsula is located between 44°38' and 46°15' latitude, 32°48' and 36°65' longitude and is surrounded by the Black and Azov seas almost from all sides. According to the integrated indicators of agro-climatic resources, the territory of the peninsula is divided into 4 zones: steppe; foothills; mountain; and southern coast. The Crimean steppe region occupies almost 75% of the peninsula territory and is characterized as semiarid prairie land. This zone is located between temperate (the northern and central part of the Crimea) and subtropical (the southern part of the peninsula, which is protected from a colder climate by the Crimean mountains) climate belts. The climate of the steppe plains is continental and moderately warm. The average annual air temperature is 11.0°C, ranging from 10.3 to 11.8°C, while the average annual precipitation in the central zone of the steppe is approximately 450 mm (Klepynine weather station, no. 6 in Fig. 1). The amount of precipitation throughout the steppe varies (spatially) from 366 to 484 mm on average per year, and from 200 to 773 mm over the years for the weather stations of the steppe zone.
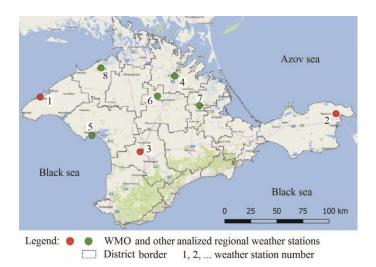
Fig. 1. Location of the weather stations used for analysis in the territory of the Crimean Peninsula.

A total of 8 weather stations were selected to carry out a comparative analysis of the RS-estimated precipitation with ground-based observations. Their zone of representativeness covers almost the entire territory of the Crimean steppe zone (Fig. 1). Data from 3 weather stations are available (free open access to long-term continual daily data) from the databases associated with the World Meteorological Organization (WMO). Table 1 reports the details of the weather stations used in the analysis.

Table 1. Weather stations characteristics.

| No | Station ID* | Name | Elevation [m] | Data availability status |
|----|-------------|------|---------------|--------------------------|
| 1 | 339240 | Chornomorske | 7 | Free open access through the WMO network |
| 2 | 339830 | Kerch | 45 | |
| 3 | 339460 | Simferopol | 177 | |
| 4 | 339340 | Dzhankoy | 9 | Partially available as free open access data through weather informer |
| 5 | 339290 | Yevpatoriya | 5 | |
| 6 | 339390 | Klepynine | 36 | |
| 7 | 339620 | Nyzhniohirsk | 20 | |
| 8 | 339220 | Razdolnoe | 17 | |

* National Climatic Data Center (NCDC) weather station number.

The weather stations listed in Table 1 are grouped as "WMO" and "regional' stations. Note that "regional" stations also have ID station numbers and use the same equipment for precipitation measurements as the "WMO" stations.

## 3. Materials and methods

GPM datasets on the spatial distribution of monthly precipitation totals for Crimea territory collected between January 2017 and July 2020 were downloaded using the Giovanni service[1], according to the FEWS

---

[1] https://giovanni.gsfc.nasa.gov/ GPM_3IMERGM v06 merged satellite-gauge precipitation monthly dataset, the final run; and the late run for last 3 months of the analyzed period used daily accumulated precipitation estimations – GPM_3IMERDL v06, spatial resolution 0.1°.

Network[2], ground data of daily precipitation totals are taken from the data of the open archive of the Rp5 weather informer[3] and WMO related the National Climatic Data Center database[4].

Raster images of precipitation distribution fields for the Crimean Peninsula derived from GPM IMERG and CHIRPS were read in GeoTIFF format. The numerical values of precipitation were read from the grids corresponding to the weather stations locations and written to the vector weather station layer (using the QGIS 3.10 point sampling plugin).

In order to analyze the convergence between the weather station data and the estimated values of the GPM_3IMERG and CHIRPS products, we employed the following statistics for monthly precipitation totals across January 2017 – July 2020: the bias, which represents the overestimation (>1) or underestimation of the measured parameter (<1); the mean error (ME) or difference, where positive/negative values indicate the average overestimation/underestimation per month compared to the basic parameter (mm); the root mean square error (RMSE) or standard deviation shows the level of precipitation variation in physical units (mm) over the months; the Pearson correlation coefficient ($r$) and coefficient of determination ($r^2$) characterize the strength of relation or dependence between compared parameters (commonly used qualitative characteristics for different $r$ levels are 0.40-0.59 "moderate", 0.60-0.79 "strong", 0.80 and higher "very strong", or "functional" if $r = 1.0$); the Nash–Sutcliffe efficiency coefficient (NSe) is used for the accuracy estimation of the RS products compared to the ground based observations, where the closer the value is to one the higher the association between the measured precipitation and satellite estimations, and a zero value indicates that the predictive properties of the satellite estimations are equal to the forecast (Dembélé, Zwart 2016).

The average (AVG) and maximum and minimum (MAX and MIN) values of the measured and estimated monthly precipitation totals were also employed to analyze the differences in their absolute values during the analyzed period. The aforementioned statistics were calculated as follows:

$$Bias = \sum P_{RS} / \sum P_M , \tag{1}$$

$$ME = \frac{\sum P_{RS} - \sum P_M}{n} , \tag{2}$$

$$RMSE = \left( \frac{\sum (P_i - P_{av})^2}{n-1} \right)^{0.5} , \tag{3}$$

$$r = \frac{\sum (P_{RS} - P_{av}^{RS}) \cdot (P_M - P_{av}^M)}{\left( \sum (P_{RS} - P_{av}^{RS})^2 \cdot \sum (P_M - P_{av}^M)^2 \right)^{0.5}} , \tag{4}$$

$$NSe = 1 - \frac{\sum (P_{RS} - P_M)^2}{\sum (P_M - P_{av}^M)^2},$$ (5)

$r = \frac{\sum (P_{RS} - P_{av}^{RS}) \cdot (P_M - P_{av}^M)}{\left( \sum (P_{RS} - P_{av}^{RS})^2 \cdot \sum (P_M - P_{av}^M)^2 \right)^{0.5}}$ where $P_i$ and $P_{av}$ are the sum precipitation per month $i$ and the aver-

aged value of monthly precipitation totals, respectively [mm]; $P_M$ and $P_{RS}$ are the monthly precipitation totals, measured and estimated by RS, respectively [mm]; $P^M_{av}$ and $P^{RS}_{av}$ are the averaged value of the monthly precipitation totals measured and estimated by RS, respectively [mm]; and $n$ is the total number of months.

The determination coefficient ($r^2$) was determined as the square of the correlation coefficient. The least-squares method was applied for the calculation of the linear regression coefficients.

## 4. Results

We compared the monthly precipitation total for the period of January 2017 – July 2020 in order to assess the strength of the association between the precipitation data derived from the RS methods (GPM IMERG and CHIRPS) and the ground-based observation data from the weather station network. Figure 2 presents the relationship between the measured and estimated values of monthly precipitation totals. The blue and green weather stations denote those with freely available data through the WMO network and several other regional weather stations of the steppe region in the Crimea, respectively. The y-axis provides information on the RS monthly precipitation totals while the x-axis presents the equivalent data from the weather stations.

Both RS products exhibit a significantly higher correlation with the WMO network weather station data (average determination coefficients are 0.65 and 0.62) than with other regional stations, with average $r^2$ values of 0.51 and 0.49 for the GPM IMERG and CHIRPS products, respectively.

The GPM IMERG product exhibits the highest correlation with the ground-based data, with $r^2$ values of 0.67 and 0.71 ("very strong") for the Kerch and Simferopol stations, respectively. The lowest correlations were determined between CHIRPS and the Dzhankoy station ($r^2 = 0.29$, "moderate" level). The remaining stations exhibited a "strong" correlation, with coefficients of determination ranging from 0.41 to 0.63.

A direct comparison between the ground data (measured at the individual points of the rain gauge location) with model estimations of the precipitation values averaged over the pixel area (0.1° or approx. 85.8 km², and 0.05° or 21.4 km² for GPM IMERG and CHIRPS, respectively) is not entirely correct. However, taking into account that the same approach is used to compare the correlation between both products, this disadvantage in the methodological approach can be neglected. Table 2 reports the resulting statistical indicators of the analysis.
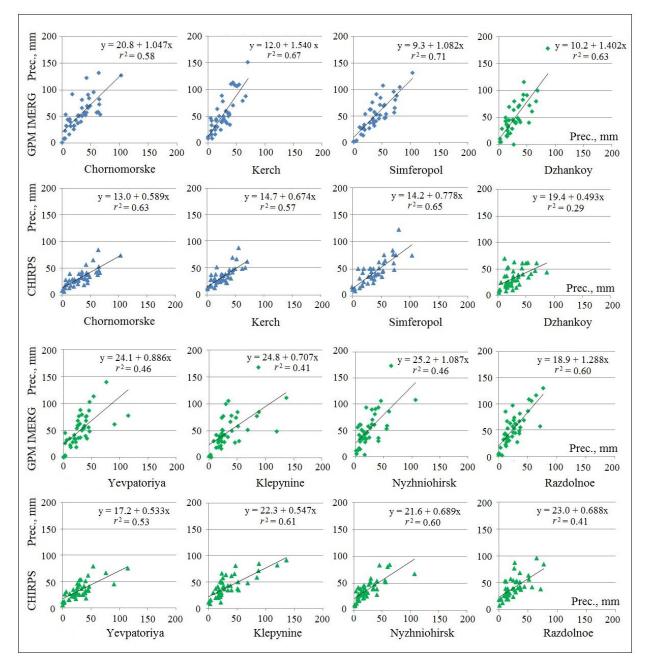
Fig. 2. Relationship between weather station precipitation data and equivalent RS estimations (GPM MERG, final run and CHIRPS). Blue – WMO network; green – regional stations.

The average amounts of the monthly precipitation for the entire study period across weather stations determined by the stations, GPM IMERG and CHIRPS were 30.4 mm, 52.0 mm and 37.2 mm, respectively, while the latter two overestimated the ground-based measurements by 21.6 and 6.8 mm (ME) per month.

The absolute deviations of the minimum RS monthly precipitation estimations from the equivalent weather station values (MIN) are low, ranging from 0.4 to 8.3 mm and 4.0 to 9.7 mm for GPM IMERG and CHIRPS, respectively. Moreover, the minimum values determined from CHIRPS exceed those of the ground-based and GPM values for all weather stations.

The absolute deviations of the maximum RS monthly precipitation estimations from those measured at weather stations (MAX) are significant for both products, varying within 25.0–91.5 mm and 15.4–45.1 mm for GPM IMERG and CHIRPS, respectively. The CHIRPS product exhibits both positive and negative deviations, while the GPM IMERG product presents consistent excess values. This can be observed in Figure 3, which depicts the variations in the measured and estimated monthly precipitation totals.

Table 2. Comparison of satellite and ground-based precipitation estimations between January 2017 and July 2020.

| Station no. | Data source | Precipitation statistics [mm] | | | | | r | Bias | NSe |
|---|---|---|---|---|---|---|---|---|---|
| | | AVG | MAX | MIN | RSME | ME | | | |
| 1 | Station | 33.2 | 103.0 | 0.0 | 22.2 | - | - | - | - |
| | GPM | 55.5 | 132.3 | 1.0 | 30.6 | 22.4 | 0.76 | 1.68 | −0.85 |
| | CHIRPS | 32.6 | 84.5 | 6.5 | 16.5 | −0.6 | 0.79 | 0.98 | 0.63 |
| 2 | Station | 27.9 | 70.7 | 0.5 | 18.0 | - | - | - | - |
| | GPM | 55.0 | 151.1 | 8.8 | 33.9 | 27.1 | 0.82 | 1.97 | −2.75 |
| | CHIRPS | 33.5 | 86.1 | 10.1 | 16.2 | 5.6 | 0.75 | 1.20 | 0.45 |
| 3 | Station | 38.5 | 103.5 | 0.0 | 23.7 | - | - | - | - |
| | GPM | 51.0 | 131.2 | 1.5 | 30,4 | 12.5 | 0.84 | 1.32 | 0.23 |
| | CHIRPS | 44.2 | 122.7 | 9.7 | 22.8 | 5.7 | 0.81 | 1.15 | 0.57 |
| 4 | Station | 28.6 | 86.4 | 1.6 | 19.0 | - | - | - | - |
| | GPM | 50.2 | 177.9 | 0.3 | 33.5 | 21.6 | 0.80 | 1.76 | −1.62 |
| | CHIRPS | 33.4 | 70.8 | 5.6 | 17.6 | 4.9 | 0.53 | 1.17 | 0.07 |
| 5 | Station | 30.3 | 114.6 | 0.0 | 23.0 | - | - | - | - |
| | GPM | 51.0 | 139.6 | 0.4 | 30.0 | 20.6 | 0.68 | 1.68 | −0.75 |
| | CHIRPS | 33.3 | 78.8 | 5.6 | 16.7 | 3.0 | 0.73 | 1.10 | 0.52 |
| 6 | Station | 34.8 | 136.3 | 0.1 | 30.0 | - | - | - | - |
| | GPM | 49.4 | 167.9 | 1.1 | 33.1 | 14.6 | 0.64 | 1.42 | −0.05 |
| | CHIRPS | 41.3 | 90.9 | 7.5 | 21.0 | 6.5 | 0.78 | 1.19 | 0.55 |
| 7 | Station | 24.3 | 106.9 | 0.9 | 20.9 | - | - | - | - |
| | GPM | 51.7 | 173.9 | 2.8 | 33.6 | 27.3 | 0.68 | 2.12 | −2.14 |
| | CHIRPS | 38.4 | 85.1 | 8.7 | 18.6 | 14.1 | 0.77 | 1.58 | 0.12 |
| 8 | Station | 26.0 | 76.8 | 0.4 | 18.5 | - | - | - | - |
| | GPM | 52.4 | 129.6 | 2.2 | 30.7 | 26.4 | 0.77 | 2.01 | −2.28 |
| | CHIRPS | 40.9 | 94.8 | 7.3 | 19.9 | 14.9 | 0.64 | 1.57 | −0.45 |
| Average | Station | 30.4 | 99.9 | 0.8 | 21.9 | - | - | - | - |
| | GPM | 52.0 | 150 | 2.3 | 32.0 | 21.6 | 0.75 | 1.75 | −1.28 |
| | CHIRPS | 37.2 | 89.3 | 7.6 | 18.7 | 6.8 | 0.73 | 1.24 | 0.31 |

The magnitude of the precipitation variations per month, characterized by the RSME value, is equal to 21.9 mm for meteorological stations on average and variations ranging between 18.0 and 30.0 mm across the study period. The CHIRPS estimations exhibit slightly lower values for 7 out of 8 stations, with an average RSME of 18.7 mm and variations within 16.2-22.8 mm. An average value of RMSE, according to the data of the GPM IMERG product, is equal to 32.0 mm (range of 30.0-33.9 mm), and exceeds the value of this parameter, calculated on the base of the gauge data, for each of all weather stations..

The average values of the correlation coefficients between the measured and estimated monthly precipitation totals are 0.75 and 0.73, with ranges of 0.64-0.84 and 0.53-0.81 for GPM IMERG and CHIRPS, respectively.

The bias parameter values confirm the overestimation of the ground-based monthly precipitation totals by the equivalent RS estimations (with the exception of the CHIRPS estimations at the Chornomorske station). The average bias values are determined as 1.75 and 1.24, with deviations 1.32–2.12, and 0.98–1.58 for GPM IMERG and CHIRPS, respectively.

The ability of the time series RS-estimations to predict the ground-based monthly precipitation totals vary across the RS products, with average efficiency coefficient NSe values of 1.28 and 0.31 and ranges of –2.75 to –0.23 and –0.45 to –0.63 for GPM IMERG and CHIRPS, respectively. The Nash–Scutliff efficiency coefficient values indicate the CHIRPS product as a more effective predictor of the ground-based observed monthly precipitation time series compared to GPM IMERG for all stations (with the exception of the Razdolnoe station, with a negative CHIRPS NSe value).
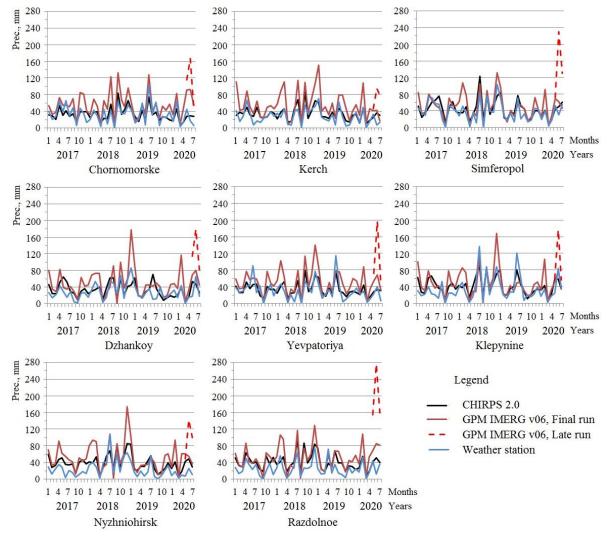


Fig. 3. Monthly variations of ground-based and RS-estimated precipitation. RS products are CHIRPS 2.0 and GPM IMERGM v06 final run across the entire study period and GPM IMERGDL v06 late run for the last three months.

The level of variation in the precipitation estimated by the CHIRPS and GPM IMERGM final run products compared to the gauge data confirms the statistical analysis presented in Table 2. However, the maximum monthly total precipitation determined by the GPM final run product (corresponding to December 2018 for 6 stations) demonstrates the requirement for additional calibration with the refinement of the resulting estimations for the region.

Considering that the final precipitation estimations determined via the GPM IMERG product have a 3 month delay in availability, the dashed line in Figure 3 allows us to estimate the magnitude of the discrepancy in monthly precipitation totals for the end of the period. The average late run overestimation compared to the final run is determined as 59.2 mm per month and 88.7 mm for the entire study period. Furthermore, the maximum deviation of 263.7 mm per month is observed for the Razdolnoe weather station in June 2020.

## 5. Discussion

The main advantage of precipitation data derived from the satellite measurements in agricultural monitoring tasks is their availability (free open access), high temporal resolution (1-5 days or higher) and improved spatial resolution (0.05 and 0.1° for CHIRPS and GPM IMERG, respectively). The weather station network available in the steppe region of the Crimea does not permit the evaluation of precipitation variations within the districts as there is approximately one station per district. The application of the RS-derived precipitation estimations as raster values allow for (taking into account the level of representativeness) an additional 25-30 raster precipitation values for the territory.

Analysis of the relationship between monthly precipitation totals determined via the weather stations and RS products reveal lower values of the determination coefficient (average of 0.52 and 0.56 for CHIRPS and GPM IMERG, respectively) than, for example, for the territory of the Cyprus (Retalis et al. 2018), where the corresponding GPM IMERG determination coefficient exceeds 0.9. A greater correlation can be induced by improving the information availability of precipitation gauge data, where the 3 Crimean WMO weather stations with free open access to data exhibited an almost 20% higher correlation than other regional stations.

Field rain gauges can aid in evaluating the accuracy of the estimated precipitation spatial distributions determined via the satellite data. However, the level of systematic error for these types of devices can reach 20-30% (WMO 2008; Villarini et al. 2008), due to the lack of metrological requirements. Moreover, in winter such simplified field rain gauges are removed from the fields. Small and automated weather stations (which often have a solar panel and batteries) have similar drawbacks. Precipitation data collected from such devices may be unavailable and have even higher errors than indicated earlier (WMO 2008) or extensive temporal shifts (via periods of negative temperatures, as well as ice/snow melting times).

The principle disadvantage of the satellite products considered in this work is the 1-1.5 months data lag on the CHIRPS monthly and 5-day precipitation totals and the 3-3.5 month lag on the GPM IMERG final calibrated data (final run). Although the GPM IMERG operational level of the precipitation estimations

(early run) and intermediate data (late run) are available, the accuracy of these datasets (Fig. 3) does not allow for their direct application in monitoring tasks or for operational and technological decision making.

## 6. Conclusions

We compared the monthly precipitation totals obtained from the GPM_3IMERGM v06 and CHIRPS 2.0 products across period January 2017 – July 2020 with ground-based observations from weather stations located in the steppe region of Crimea. The following key conclusions were made.

The CHIRPS and GPM IMERG products demonstrated, on average, an overestimation of gauged monthly precipitation totals by 6.8 mm and 21.6 mm·month$^{-1}$ (22% and 71%). Furthermore, the average deviation of the precipitation determined from the WMO weather stations were 11% and 62%, with 30% and 77% for other regional weather stations, respectively.

The correlation coefficients between the measured monthly precipitation totals and estimations were determined as 0.75 and 0.73, for GPM IMERG (final run) and CHIRPS, respectively.

The average absolute deviations of the minimum RS estimated monthly precipitation totals from the ground-based observations were 2.3 and 7.6 mm for GPM IMERG and CHIRPS, respectively. This is comparable with the accuracy of the soil moisture content measured in the field under common practice in the Crimea that enables to neglect them in agrohydrological calculations.

The two products considered in this paper have distinct advantages and disadvantages based on their spatial and temporal resolution. Synthesizing the favorable features of each products can improve their quality indicators. For example, during a 3-month absence of the GPM IMERG final run data, the CHIRPS data can be employed for 2 months. However, for the last month, further verification and calibration of the daily GPM IMERG data is required for its subsequent application in operational agro-technological decisions.

## Acknowledgments

REFERENCES

Beck H.E., Pan M., Roy T., Weedon G.P., Pappenberger F., van Dijk A.I.J.M., Huffman G.J., Adler R.F., Wood E.F., 2019, Daily evaluation of 26 precipitation datasets using Stage-IV gauge-radar data for the CONUS, Hydrology and Earth System Sciences, 23(1), 207-224, DOI: 10.5194/hess-23-207-2019

Chen S., Zhang L., Zhang Y., Guo M., Liu X., 2020, Evaluation of Tropical Rainfall Measuring Mission (TRMM) satellite precipitation products for drought monitoring over the middle and lower reaches of the Yangtze River Basin, China, Journal of Geographical Sciences, 30, 53-67, DOI: 10.1007/s11442-020-1714-y

Chokngamwong R., Chiu L.S., 2008, Thailand daily rainfall and comparison with TRMM products, Journal of Hydrometeorology, 9, 256-66, DOI: 10.1175/2007JHM876.1

Dembélé M., Zwart S.J., 2016, Evaluation and comparison of satellite-based rainfall products in Burkina Faso, West Africa, International Journal of Remote Sensing, 37(17), 3995-4014, DOI: 10.1080/01431161.2016.1207258

Dinku T., Funk C., Peterson P., Maidment R., Tadesse T., Gadain H., Ceccato P., 2018, Validation of the CHIRPS satellite rainfall estimates over eastern of Africa, Quarterly Journal of the Royal Meteorological Society, 144(51), 292-312, DOI: 10.1002/qj.3244

Ebert E.E., Janowiak J.E., Kidd C., 2007, Comparison of near real-time precipitation estimates from satellite observations and numerical models, Bulletin of the American Meteorological Society, 88(1), 47–64, DOI: 10.1175/BAMS-88-1-47

Funk C.C., Peterson P.J., Landsfeld M.F., Pedreros D.H., Verdin J.P., Rowland J.D., Romero B.E., Husak G.J., Michaelsen J.C., Verdin A.P., 2014, A quasi-global precipitation time series for drought monitoring, U.S. Geological Survey Data Series, 832, DOI: 10.3133/ds832

Funk C., Verdin J., Michaelsen J., Peterson P., Pedreros D., Husak G., 2015, A global satellite-assisted precipitation climatology, Earth System Science Data, 7, 275-287, DOI: 10.5194/essd-7-275-2015

Hou A.Y., Kakar R.K., Neeck S., Azarbarzin A.A., Kummerow C.D., Kojima M., Oki R., Nakamura K., Iguchi T., 2014, The global precipitation measurement mission, Bulletin of the American Meteorological Society, 95, 701-722, DOI: 10.1175/BAMS-D-13-00164.1

Huffman G., Bolvin D., Nelkin E., Wolff D., Adler R., Gu G., Hong Y., Bowman K. P., Stocker E., 2007, The TRMM Multisatellite Precipitation Analysis (TMPA): Quasi-global, multiyear, combined-sensor precipitation estimates at fine scales, Journal of Hydrometeorology, 8, 38-55, DOI: 10.1175/JHM560.1

Karthikeyan L., Pan M., Wanders N., Kumar D.N., Wood E.F., 2017, Four decades of microwave satellite soil moisture observations: Part 2. Product validation and inter-satellite comparisons, Advances in Water Resources, 109, 236-252, DOI: 10.1016/j.advwatres.2017.09.010

Kidd C., Levizzani V., Turk J., Ferraro R., 2009, Satellite precipitation measurements for water resource monitoring, Journal of the American Water Resources Association, 45(3), 567-579, DOI: 10.1111/j.1752-1688.2009.00326.x

Liu C., Zipser E.J., 2015, The global distribution of largest, deepest, and most intense precipitation systems, Geophysical Research Letters, 42(9), 3591-3595, DOI: 10.1002/2015GL063776

Liu J., Duan Z., Jiang J., Zhu A., 2015, Evaluation of three satellite precipitation products TRMM 3B42, CMORPH, and PERSIANN over a subtropical watershed in China, Advances in Meteorology, 2015, DOI: 10.1155/2015/151239

Liu Z., Ostrenga D., Teng W., Kempler S., 2012, Tropical Rainfall Measuring Mission (TRMM) precipitation data and services for research and applications, Bulletin of the American Meteorological Society, 1317-1325, DOI: 10.1175/BAMS-D-11-00152.1

Nashwan M., Shahid S., Wang X., 2019, Assessment of satellite-based precipitation measurement products over the hot desert climate of Egypt, Remote Sensing, 11(5), DOI: 10.3390/rs11050555

Ning S., Wang J., Jin J., Ishidaira H., 2016, Assessment of the latest GPM-era high-resolution satellite precipitation products by comparison with observation gauge data over the Chinese mainland, Water, 8(11), DOI: 10.3390/w8110481

Pang J., Zhang H., Xu Q., Wang Yujie, Wang Y., Zhang O., Hao J., 2020, Hydrological evaluation of open-access precipitation data using SWAT at multiple temporal and spatial scales, Hydrology and Earth System Science, 24, 3603-3626, DOI: 10.5194/hess-24-3603-2020

Paredes-Trejo F.J., Barbosa H.A., Kumar T.L., 2017, Validating CHIRPS-based satellite precipitation estimates in Northeast Brazil, Journal of Arid Environment, 139, 26-40, DOI: 10.1016/j.jaridenv.2016.12.009

Retalis A., Katsanos D., Tymvios F., Michaelides S., 2018, Validation of the first years of GPM operation over Cyprus, Remote Sensing, 10(10), 1520, DOI: 10.3390/rs10101520

Saeidizand R., Sabetghadam S., Tarnavsky E., Pierleoni A., 2018, Evaluation of CHIRPS rainfall estimates over Iran, Quarterly Journal of the Royal Meteorological Society, 144(51), 282-291, DOI: 10.1002/qj.3342

Satgé F., Ruelland D., Bonnet M. P., Molina J., Pillco R., 2019, Consistency of satellite-based precipitation products in space and over time compared with gauge observations and snow-hydrological modelling in the Lake Titicaca region, Hydrology and Earth System Science, 23(1), 595-619, DOI: 10.5194/hess-23-595-2019

Scheel M.L., Rohrer M., Huggel C., Villar D.S., Silvestre E., Huffman G.J., 2011, Evaluation of TRMM multi-satellite precipitation analysis (TMPA) performance in the Central Andes region and its dependency on spatial and temporal resolution, Hydrology and Earth System Science, 15(8), 2649-2663, DOI: 10.5194/hess-15-2649-2011

Tang G., Clark M.P., Papalexiou S.M., Ma Z., Hong Y., 2020, Have satellite precipitation products improved over last two decades? A comprehensive comparison of GPM IMERG with nine satellite and reanalysis datasets, Remote Sensing of Environment, 240, DOI: 10.1016/j.rse.2020.111697

Villarini G., Mandapaka P.V., Krajewski W.F., Moore R.J., 2008, Rainfall and sampling uncertainties: A rain gauge perspective, Journal of Geophysical Research, 113(D11), DOI: 10.1029/2007JD009214

Wang C., Tang G., Han Z., Guo X., Hong Y., 2018, Global intercomparison and regional evaluation of GPM IMERG Version-03, Version-04 and its latest Version-05 precipitation products: similarity, difference and improvements, Journal of Hydrology, 564, 342-356, DOI: 10.1016/j.jhydrol.2018.06.064

WMO, 2008, Guide to hydrological practices. Volume I. Hydrology – From measurement to hydrological information, 6th edition, WMO-No. 168, World Meteorological Organization, Geneva, available at
http://www.wmo.int/pages/prog/hwrp/publications/guide/english/168_Vol_I_en.pdf (data access 10.08.2020)

Xiao S., Xia J., Zou L., 2020, Evaluation of multi-satellite precipitation products and their ability in capturing the characteristics of extreme climate events over the Yangtze River basin, China, Water, 12(4), DOI: 10.3390/w12041179

Yee M.S., Walker J.P., Rüdiger C., Parinussa R.M., Koike T., Kerr Y.H., 2017, A comparison of SMOS and AMSR2 soil moisture using representative sites of the OzNet monitoring network, Remote Sensing of Environment, 195, 297-312, DOI: 10.1016/j.rse.2017.04.019

# Estimates of current and future climate change in Belarus based on meteorological station data and the EURO-CORDEX-11 dataset

Irina Danilovich

Institute for Nature Management, National Academy of Sciences, Akademycheskaya 27, 002272 Minsk, Belarus

Beate Geyer

Institute for Coastal Research, Helmholtz-Zentrum Geesthacht, Max-Planck-Straße 1, 21502 Geesthacht, Germany

Abstract

This study provides an assessment of the current and future changes (in terms of both direction and value) in air temperature, precipitation, snow, wind and their extremes over the territory of Belarus using information from 42 meteorological stations and 92 regional circulation model (RCM) simulations with the highest available horizontal resolution (EUR-11). Three representative concentration pathway scenarios, namely, RCP2.6, RCP4.5 and RCP8.5, are considered.

Results demonstrate that in recent decades, temperature has increased over the territory of Belarus by 1.3°C, with the largest increase occurring during the cold season (2.1-2.3°C). Ensemble scenarios project further increases in air temperature in the current century by +0.5-1.5°C, +2.8°C, and +5.2°C under the RCP2.6, RCP4.5 and RCP8.5 scenarios, with the largest increase during the cold season under the RCP8.5 scenario. The annual means were observed to increase (insignificantly) by 5-7% and the summer precipitation extremes exhibited a 20-25% growth in recent decades. Moreover, dry conditions have intensified in Belarus, particularly during the growing season. Further increases in precipitation of 10-15% across Belarus are projected to occur in all seasons under the RCP4.5 and RCP8.5 scenarios. Simulation models predict greater increases in single day rainfall events compared to their multiday precipitation counterparts. The greatest increases in maximal dry period length (by 1-2) are expected to occur in summer and autumn. The models project the general decrease in snowfall across Belarus to continue into the current century, with a reduction in snow precipitation days of 10-30 days. Despite the reduced wind strength (by 0.9-1.0 m·s⁻¹) since the 1970s over the territory of Belarus, the ensemble model reveals slight nonsignificant changes in seasonal and annual wind strengths until the end of the century. Significant changes of 1-3 days under varying directions of the wind regime were observed for days with a strong breeze and storms.

Keywords

Climate change, meteorological observations, projections, scenario, air temperature, precipitation, snow, wind.

## 1. Introduction

Climate change influences almost all components of the environment and human activity at the global scale. In particular, the hydrological cycle, agriculture, culture, human health and activity, and human-made infrastructure are sensitive to climate change, specifically to changes in the spatial and temporal distributions of temperature, total precipitation (rain and snow) and near-surface wind. Furthermore, contemporary climate change is characterized by the intensification of various extreme phenomena at the regional scale (Siegmund et al. 2019). Belarusian territory is highly impacted by ongoing and projected changes, and

the collaboration of geoscientists from this part of Europe is required in order to mitigate climate change in a coherent manner.

Numerous recent climate studies have assessed possible future climate changes based on numerical simulations. The model results are typically presented as deviations of different variables from historical climate conditions within the target regions. This method takes into account the bias between climate simulations and data from meteorological stations. Climate models are corrected based on in situ observations. However, in order to understand the variability of the projected climatic characteristics, the current climate changes must be assessed.

The Belarusian hydro-meteorological service collects long-term time series of observed climatic characteristics, permitting estimations of ongoing changes in climate that can subsequently be employed to understand potential future climate change trends. Podgornaya et al. (2015) established fluctuations in annual temperature within 1900-2014 to vary close to the temperature climatological norm (1881-1990). Significant variations in the Belarusian temperature regime have been observed since 1989. In particular, the current warming is unprecedented in its duration, and the higher temperatures occurring during the past 30 years (1989-2018) have exceeded the average climatic norm (1961-1990) by 1.3°C. In addition, the three warmest years in Belarus (1989, 2008 and 2015) since 1880 occurred from 1989-2015 (Melnik et al. 2018).

No significant changes have been observed in the mean annual precipitation at the end of the 20th century in Belarus, while the increased irregularity of precipitation and rise in air temperature caused twice as many periods of drought as before (climate warming period of 1989-2018). Moreover, the wind speed in Belarus has declined since the 1970s (Loginov 2008). During this period (1989-2018), extreme weather phenomena were observed more frequently in Belarus, and the World Meteorological Organization warns that climate extremities will increase in the future (Siegmund et al. 2019).

Several studies have investigated future climate change in Belarus based on climate model outputs. Due to the small size, compact configuration and location between Europe and the Russian Federation, Belarus has often been part of climatic assessments in large multi-country projects such as CMIP3, CMIP5, PRUDENCE and ENSEMBLE (Frich et al. 2002; Metzger et al. 2005; van der Linden, Mitchell 2009; Taylor et al. 2011).

Current model data with high temporal and spatial resolution are represented by the consortium EURO-CORDEX. Jacob et al. (2014) employed this data to conduct a detailed analysis of future climate changes revealing increases in air temperature of 2.0-4.2 and 4.1-6.2°C (depending on the scenario) by the end of the current century over the central European territory, including Belarus. More specifically, the rise in precipitation amount was determined as 7-18% and 19-32% under the RCP2.6 and RCP8.5 scenarios.

Research on climate change in Russia (Shkolnik et al. 2006; Govorkova et al. 2008; Meleshko et al. 2008; Mokhov, Eliseev 2012; Kokorev, Anisimov 2013) often include the territory of Belarus. The regional model outputs of the Institute of Physics of the Russian Academy of Sciences (Mokhov, Eliseev 2012)

suggest that air temperature will rise in the European part of Russia and Belarussian territory and, depending on the scenario, may increase through the end of the 21st century from 3.0-3.5°C to 4.0-4.5°C under the RCP2.6 scenario and to 4.0-8.0°C under the RCP4.5 and RCP8.5 scenarios.

Analysis of climate projections based on the 31 CMIP5 climate models under the RCP4.5 scenario revealed a significant change in key climatic characteristics through the middle of the current century within the territory of Belarus (Pavlova 2013; Snezhko et al. 2017).

Loginov et al. (2000) investigated future climate changes specifically for the territory of Belarus in the early years of the 21st century. Results confirmed the probable rises in key meteorological parameters by the end of 2100. For example, the mean, maximum and minimum air temperatures are expected to increase by up to 3.0°C, 2.7-2.9°C, and 3.2-3.3°C, respectively, depending on the concentration of greenhouse gases and the presence of sulphate substances in the air. The rise in the amount of precipitation is calculated a 0.12-0.20 kg·m$^{-2}$·day$^{-1}$ (10% every year), the increase in partial pressure of water vapour is given as 1.7-1.9 hPa, and the wind speed rise is 0.07-0.17 m·s$^{-1}$. The greatest changes in the meteorological parameters coincide with a rise in greenhouse gas concentrations, while in the presence of sulphate substances, the variations are lower.

Further research on climate change in Belarus based on CMIP5 climate projections demonstrates an increase in the warm period duration ($T_{day} \geq 0$°C) of up to 35 days from 2041-2060 and projects that the warm period will vary from 280 to 310 days. The agricultural zoning of the territory of Belarus was updated according to the projected temperature (Melnik et al. 2017).

A detailed assessment of future climatic changes in Belarus using model simulations by the EURO-CORDEX (EUR-44) consortium reveals significant changes in air temperature and precipitation by the end of the current century. The mean air temperature and precipitation are expected to rise by up to 2.4-4.7°C and 15-30 kg·m$^{-2}$ per year, respectively, through the end of the current century. The seasonal and annual values of temperature and precipitation vary depending on the chosen combination of global and regional models. The smallest changes were noted for the RCP2.6 scenario, while the most significant variations were observed for RCP8.5. The greatest changes within each scenario occurred during winter and spring (colder times of the year) (Partasenok et al. 2015; Danilovich, Geyer 2018).

Danilovich et al. (2020) analyzed the observed and projected climate changes in the Polesje region (southern area of Belarus), concluding that current climate change trends will be maintained in the near future. In particular, the air temperature will continue to rise and the variation in the minimal temperature will exceed that of the maximal and mean temperatures. A rise in precipitation events of moderate intensity will increase the precipitation amount, while the duration of the drought periods will enhanced in the summer.

In the present study, we aim to estimate the current and future changes (both the direction and value) in air temperature, precipitation (rain and snow), wind and their extremes over the territory of Belarus using

information from meteorological stations and 92 regional climate model (RCM) simulations with the highest available horizontal resolution (EURO-CORDEX, 0.11°).

The rest of the manuscript is structured as follows. Section 2 provides a description of the data and methods employed for the analysis. Section 3 details the study area, while Section 4 presents the observational data. Section 5 describes the projections of air temperature, precipitation, snow and wind, including current climate changes in Belarus, the assessment of multimodel median climate change signals under different emission scenarios, and estimates of the projected extremes. The results are discussed in Section 6 and Section 7 concludes the study.

## 2. Data and methods

A set of 92 RCM simulations from the EURO-CORDEX initiative (Jacob et al. 2014; Kotlarski et al. 2014) are analyzed. A horizontal resolution of 0.11° (~12 km, EUR-11) is used and three representative concentration pathways (i.e., aerosol and greenhouse gas emissions) (Moss et al. 2010) scenarios, namely, RCP2.6 (10 simulations), RCP4.5 (43 simulations), and RCP8.5 (39 simulations), are considered. The dataset is derived from 5 RCMs and 7 CMIP5 general circulation models (GCMs) (Taylor et al. 2011) that provide boundary and initial conditions. Table 1 provides an overview of the models. We selected all models that were publicly available via the Earth System Grid Federation archive in January 2017 and provided at least one scenario, a historical simulation, and an evaluation simulation.

Figure 1 illustrates the model orography of Belarus for the 0.11°-resolution grid used for the simulations contributed by the CLM community (~12 km, EUR-11) as an example.
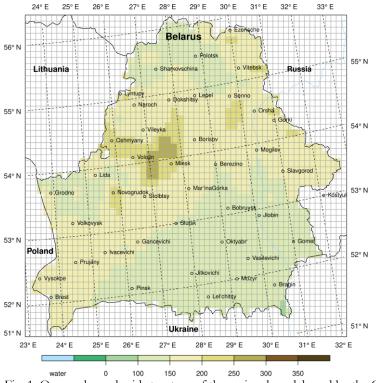


Fig. 1. Orography and grid structure of the regional model used by the CLM community in EURO-CORDEX with a 0.11°-resolution and locations of the observational meteorological stations for Belarus.

Table 1. Dataset of the EURO-CORDEX climate models used in the study.

| Model/Climate Variable | Temperature | | | | | Precipitation | | | | | | Snow | | | | | Wind | | | | |
|---|---|---|---|---|---|---|---|---|---|---|---|---|---|---|---|---|---|---|---|---|---|
| | CLMcom-CCLM4-8-17 | DMI-HIRHAM5 | KNMI-RACMO22E | MPI-CSC-REMO2009 | SMHI-RCA4 | CLMcom-CCLM4-8-17 | DMI-HIRHAM5 | KNMI-RACMO22E | MPI-CSC-REMO2009 | SMHI-RCA4 | IPSL-INERIS-WRF331F | CLMcom-CCLM4-8-17 | DMI-HIRHAM5 | KNMI-RACMO22E | MPI-CSC-REMO2009 | SMHI-RCA4 | CLMcom-CCLM4-8-17 | DMI-HIRHAM5 | KNMI-RACMO22E | MPI-CSC-REMO2009 | SMHI-RCA4 |
| ICHEC-EC-EARTH.r3i1p1[1] | | | | | | + o | | | | | | + o | | | | | | | | | |
| ICHEC-EC-EARTH.r1i1p1 | | | | | | | | | | | | | | | | | | | + o | | |
| CNRM-CERFACS-CNRM-CM5 | + o | | | | + | + o | | | | o | + | | | | + o | | + o | | | | + o |
| NCC-NorESM1-M.r1i1p1 | | + o | | | | | | | | | | | | | | | | + | | | |
| MOHC-HadGEM2-ES.r1i1p1 | | | + o | | | + | | + | | | | | + | | + | | + o | | o | | o |
| MPI-M-MPI-ESM-LR.r2i1p1 | | | | Δ + o | | | | | Δ + o | | | | | | | | | | | Δ + o | |
| ICHEC-EC-EARTH.r12i1p1 | | | | | Δ + o | + o | | + o | Δ o | + | | | Δ | | Δ + o | | + o | | | | Δ + o |
| IPSL-IPSL-CM5A-MR.r1i1p1 | | | | | + o | | | | | + o | | | | | | | | | | | + o |
| MOHC-HadGEM2-ES.r1i1p1 | | | | | + o | | | | | + o | | | | | | | | | | | + |
| MPI-M-MPI-ESM-LR.r1i1p1 | | | | | + o | + | | | Δ + o | + o | | | | | | + o | o | | | Δ + o | + o |
| RCM | | | | RCM | | | | | | RCM | | | | | | RCM | | | | | |
| Total 19 | | | | | | Total 32 | | | | | | Total 12 | | | | | Total 29 | | | | |

(Left row label: GSM)

Symbols:
Δ RCP2.6;
+ RCP4.5;
o RCP8.5;

## 3. Meteorological variables

We employed the simulated daily mean datasets of temperature, total precipitation, snow and wind speed.

Temperature is evaluated using the following variables: the mean, maximal and minimal temperatures; the number of hot (daily maximum temperature >30°C), summer (daily maximum temperature of day >25°C), frost (daily minimum temperature <0°C) and ice (daily maximum temperature <0°C) days; the number of tropical nights (daily minimum temperature >20°C); and the frost and hot period lengths.

Precipitation and snow are described by the mean precipitation; the frequencies of precipitation days (daily precipitation amount >0.1 kg·m⁻²), wet days (daily precipitation amount >1.0 kg·m⁻²), intense precipitation days (daily precipitation amount >10 kg·m⁻²), and heavy precipitation days (daily precipitation amount >20 kg·m⁻²); maximum dry and hot period lengths; the highest precipitation amount in a 5-day precipitation period; and the 95th percentile of all of the precipitation days.

---

[1] for rN, N is the number of the ensemble member; for iN, N is the number of the used initialization state; for pN, N is the number of the used physical parameterization.

The wind speed characteristics are the mean and maximal wind speeds and the numbers of light-breeze days (daily averaged wind strength $\leq 2$ m·s$^{-1}$), strong-breeze days (daily averaged wind strength $\geq 11$ m·s$^{-1}$), and storm days (daily averaged wind strength $\geq 18$ m·s$^{-1}$).

## 4. Observational data and reference period

The station meteorological dataset is based on daily observations from a set of 42 stations covering the territory of Belarus. The dataset is stored at the State Climate Cadastre of the Republic of Belarus (Belhydromet 2019). Figure 1 presents the meteorological station locations.

In order to validate the simulations, seasonal and mean values of air temperature and precipitation are calculated for every station from the meteorological observation dataset during 1971-2000.

The spatial pattern of climate change over the study area is described by a gridded meteorological dataset. The meteorological network dataset is interpolated via the kriging method (Gaussian process regression) (Lysenko et al. 2019). The spatial distribution of the gridded dataset is 0.05° (5.5 km × 3.5 km).

We compute the statistics of the meteorological variables under the following periods: (1) 1971-2000, the historical period used in the EURO-CORDEX calculations (Jacob et al. 2014); (2) 1981-2010, the period suggested by the WMO Guidelines for the calculation of climate normals (WMO 2017); and (3) 1989-2018, the period of climate change in Belarus (Loginov 2008).

The differences in the means for the aforementioned periods are as follows: 0.9°C for the mean annual temperature; 0.7-1.0°C for the mean seasonal temperature (Fig. 2, Tab. 2); and 25 kg·m$^{-2}$ or 4% for annual precipitation for 1971-2018 (Fig. 3) or 1-11 kg·m$^{-2}$ for seasons with the largest differences in winter and spring and without significant changes in summer and autumn (Tab. 3). The standard deviations of monthly mean temperature has decreased in recent decades (Tab. 2), while the standard deviations of precipitation generally has increased (Tab. 3).

The analyses of the daily data are performed for the four meteorological seasons of winter (DJF: December-February), spring (March-May), summer (JJA: June-August), and autumn (September-November). Parts of this manuscript are divided by cold (November-March) and warm (April-October) periods.

The observational data are used to analyze the current climate change trends in Belarus. Future changes in air temperature, precipitation and wind are calculated as the difference between the modelled historical data and projected data. The bias introduced by the coarse resolution of the GCMs is corrected by the application of the RCMs. We apply the common assumption that systematic model errors are equal for historical and future conditions. Thus, by analyzing the differences, the systematic errors of the models are excluded from consideration.

Present-day and future conditions are defined as those during 1971-2000 and 2021-2099, respectively. The results are determined as seasonal, annual 20-year smoothed means for the air temperature, precipitation, wind and climatological indices during the periods 2021-2040, 2041-2060, 2061-2080, and 2081-2099.
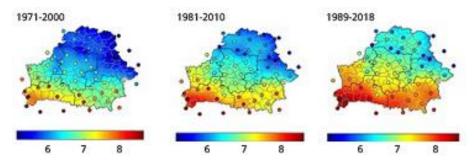
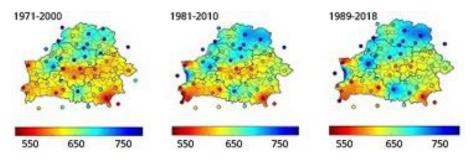Fig. 2. Climatological means of air temperature in Belarus for different periods (°C).



Fig. 3. Mean annual precipitation in Belarus for different periods (kg·m⁻²).

## 5. Location and climatology of the study area

Belarus is located in Eastern Europe or in the southwest of the East European Plain. Poland borders Belarus to the west, with Lithuania to the northwest, Latvia to the north, Russia to the northeast and the east, and Ukraine to the south (Fig. 1). The national borders occur across flat terrain, as Belarus has no significant natural boundaries.

The general landscape of Belarus is a plain dotted with hills to the north and west (Fig. 1). Only one-fifth of the country exceeds an elevation of 200 m. Central Belarus, known as the Belarusian ridge, divides the Baltic Sea (47%) and Black Sea (53%) catchment areas. The highest point is the Dzerzhinskaya mountain, reaching an elevation of 345 m. The lowest point in the territory of Belarus is located in the valley of Neman, close to the Lithuanian border, with an elevation of approximately 80-85 m.

The climate of Belarus is influenced by its midlatitude location, flat relief and relative proximity to the Atlantic Ocean. It is classified as moderately continental according to Alisov's classification system (Alisov 1936) and warm-summer humid continental climate (Dfb) according to the Köppen-Geiger classification (Beck 2018). The mean temperature (1971-2000/1989-2018) fluctuates from 5.3/6.4°C in the northeast to 6.7/7.7°C in the southwest; the mean January temperature varies from –7.1/–4°C in the northeast to –5.6/–3.6°C in the southwest, while the mean July temperature varies from 17.4/18.5°C in the northwest to 18.2/19.5°C in the southeast (Fig. 2). Table 2 reports the seasonal temperature means.

The mean annual precipitation ranges within 600-650 kg·m⁻² in the lowland plains to 700-750 kg·m⁻², and increases with elevations. Approximately 70% of the precipitation falls as rain during the warm part of the year. The mean precipitation (1971-2000/1989-2018) during the winter is recorded to be within 114/124 kg·m⁻² per season, with the mean January precipitation varying from 38/45 kg·m⁻² in the northeast to

35/37 kg·m⁻² in the southwest, and that in July averaging 87/85 kg·m⁻² per month in the northwest to
83/94 kg·m⁻² per month in the southeast (Fig. 3). Table 3 presents the mean seasonal precipitation totals.

Table 2. Air temperature climatological means (°C, numerator) and their standard deviations based on daily observations (°C, denominator) for Belarus.

| Period | Winter | Spring | Summer | Autumn | Year |
|---|---|---|---|---|---|
| 1971-2000 | −4.3 / 2.5 | 6.6 / 1.3 | 16.9 / 1.1 | 6.1 / 1.1 | 6.3 / 1.0 |
| 1981-2010 | −4.0 / 2.5 | 7.0 / 1.2 | 17.4 / 1.2 | 6.5 / 1.2 | 6.7 / 0.9 |
| 1989-2018 | −3.4 / 2.0 | 7.4 / 1.0 | 17.9 / 1.1 | 6.8 / 1.2 | 7.2 / 0.7 |

Table 3. Precipitation climatological means (kg·m⁻², numerator) and their standard deviations based on daily observations (kg·m⁻², denominator) for Belarus.

| Period | Winter | Spring | Summer | Autumn | Year |
|---|---|---|---|---|---|
| 1971-2000 | 114 / 19.2 | 129 / 27.5 | 231 / 56.5 | 156 / 41.6 | 630 / 64.8 |
| 1981-2010 | 120 / 22.5 | 136 / 31.3 | 234 / 53.6 | 157 / 38.9 | 647 / 66.0 |
| 1989-2018 | 124 / 22.9 | 140 / 28.9 | 234 / 56.7 | 158 / 44.2 | 655 / 76.3 |

## 6. Evaluation of simulation data

The evaluation of the EURO-CORDEX RCM ensemble (Kotlarski et al. 2014) confirms the ability of the models to capture the basic features of the European climate, including their variability in space and time. Moreover, no negligible deficiencies are identified for the simulations in terms of selected metrics, regions, and seasons.

The ability of the EURO-CORDEX simulations to represent air temperature, precipitation and wind for the Belarus territory is investigated relative to the meteorological station observations. The evaluation strategy is based on the mean annual and seasonal values for each GCM-RCM simulation dataset and their medians compared against the mean annual and seasonal values of every meteorological station and their mean over the territory of Belarus. The evaluation is performed across the period of 1971-2000 for both the meteorological station dataset (i.e., observations) and simulations.

Figures 4 and 5 compare the observational records of the 1971-2000 changes in surface air temperature and precipitation to the simulated data from each EURO-CORDEX model and the respective multimodel median.
The interannual variability in the majority of the EURO-CORDEX simulations is qualitatively similar to that of the observed data, although there are several exceptions. For example, the magnitude of interannual variations in the observations is larger than the multimodel median. This is because the averaging of the multiple model results acts as a filter to the simulated variability (Flato 2013).
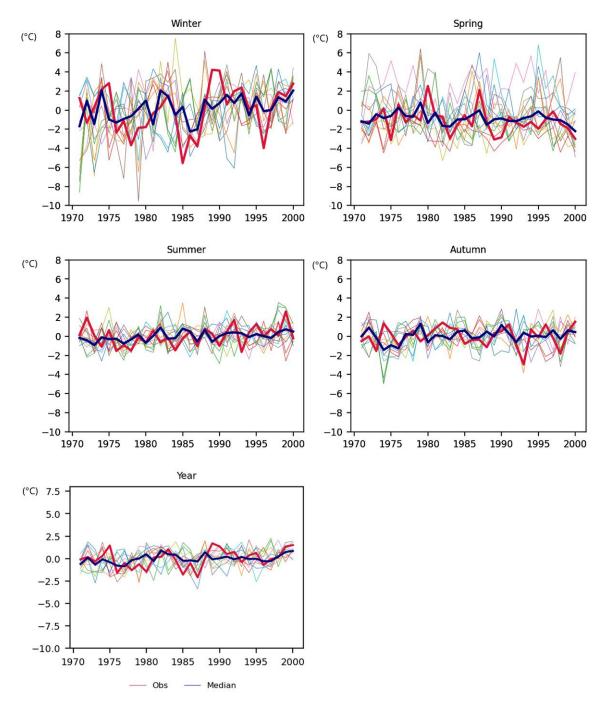
Fig. 4. Evaluation of EURO-CORDEX regional climate model (RCM) simulations over Belarus for seasonal and yearly air temperatures. The analysis is conducted for 14 historical GCM-driven RCMs (colored lines), and their median (dark blue line) and mean seasonal and yearly air temperatures aggregated across 42 stations (red line).
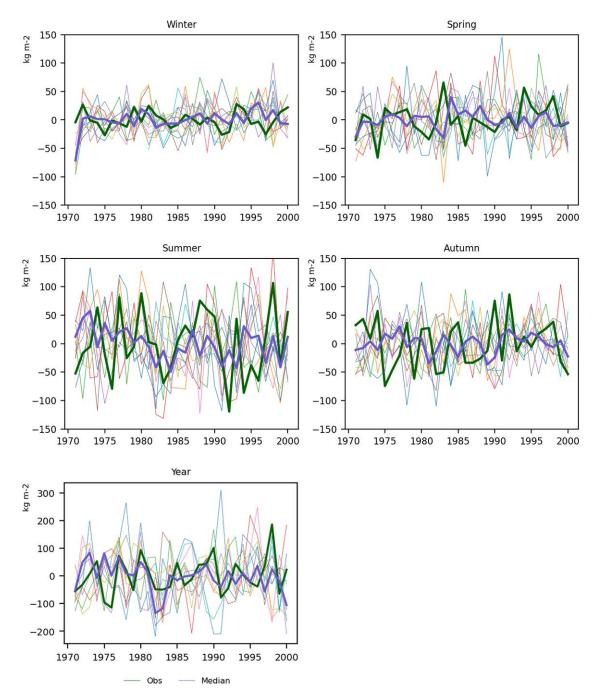
Fig. 5. Evaluation of EURO-CORDEX regional climate model (RCM) simulations over Belarus for seasonal and annual precipitation. The analysis is conducted for 14 historical GCM-driven RCMs (colored lines), and their median (dark blue line) and mean seasonal and annual precipitation aggregated across 42 stations (green line).

The quantitative performance of the models is evaluated by examining the mean error (ME), relative error (RE) and root mean square error (RMSE). Figures in Appendix A present the EURO-CORDEX model mean seasonal ME and RMSE of the surface air temperature, precipitation and wind (determined via the difference between the individual model simulations and observed station data).

According to Kotlarski et al. (2014) the EURO-CORDEX ensemble seasonally and regionally averaged temperature biases (the difference model-reference of spatially averaged climatological means) for the

European domain generally do not exceed 1.5°C. The temperature bias spread across different configurations of an individual model can be of a similar magnitude as the spread across different models, demonstrating the strong influence of the specific choices in physical parameterizations and the experimental setup on the model performance.

The mean ME of all air temperature simulations is negative in winter and spring, and positive in summer and autumn. The largest MEs are obtained for spring (–1.5°C) and winter (−0.8°C). This may be associated with the model underestimations; the smallest errors were detected in summer and autumn with 0.4-0.5°C. The yearly ME does not exceed 0.4°C and the relative error of air temperature is approximately 24% in spring and 2% in summer.

The RMSE is largest in winter, reaching 3.7°C, and gradually decreases by season to 2°C in autumn. This is explained by the higher variability in air temperature in winter due to frequent changes in atmospheric circulation and flowing air masses from the Atlantic Ocean, Siberia and Arctic.

The precipitation ME is largest in winter and spring and equals approximately 40 kg·m$^{-2}$ per season; however, the relative error is approximately 20% for winter and 30% for spring. The summer-autumn mean errors in precipitation are approximately 13-14 kg·m$^{-2}$ and do not exceed 5-10%, while precipitation biases for the entire European domain are typically in the ±40% range (Kotlarski et al. 2014). However, the RMSE indicates the largest values of more than 100 kg·m$^{-2}$ to occur in summer due to the high variability of precipitation and the complicated regime of frontal and convective precipitation during this season, which is difficult to parameterize. The smallest RMSE of 60 kg·m$^{-2}$ is obtained in winter.

The simulated seasonal and yearly wind means are in modest agreement with the observations. The wind MEs are stable within seasons and vary from 1.0 to 1.2 m·s$^{-1}$, with the largest values in autumn. However, at the relative scale, the MEs are quite large and reach 30% and 50% in winter and summer, respectively. The wind RMSE is largest in winter and autumn and corresponds to the wind speed seasonal increase.

The EURO-CORDEX simulations generally perform well in the qualitative (i.e., seasonal and geographical variations) and quantitative (i.e., errors) characterizations of the climate in Belarus. This demonstrates the ability of the EURO-CORDEX models to reproduce the general features of the annual and seasonal mean surface temperature, precipitation and wind, although the agreement between simulations and observations is limited in certain seasons.

## 7. Results

This section is structured into four subsections according to air temperature, precipitation, snow and wind. Each subsection consists of (a) the peculiarities of current climate changes in Belarus; (b) an assessment of multimodel median climate change signals for different emission scenarios; and (c) estimates of the projected extremes.

The spatial patterns associated with multimodel median projected climate changes across the territory of Belarus are not presented here due to the lack of clear spatial patterns of the meteorological characteristics per season.

## 7.1. Temperature

PECULIARITIES OF CURRENT CLIMATE CHANGES. The annual mean temperature in Belarus has exceeded the climatological norm (1961-1990) by 0.1-2.1°C almost every year since 1989. The linear trend of annual temperature for the post-WWII period varies from 0.25°C per decade in the north to 0.35°C in the south. The largest degree of warming occurs during the cold season. The trend of winter temperature change varies from 0.35°C per decade in the west and some southern regions to 0.45°C in the north and east. The trend in summer temperature changes is approximately 0.1°C per decade in the west and 0.25°C in the southern and central regions. The mean maximum temperature for the cold period has increased by 1.5-1.7°C, while that for the warm period has increased by 0.7-0.8°C. Moreover, the mean minimum temperature has increased by 1.8-2.0°C for the cold period and by 0.6-0.7°C for the warm period.

ASSESSMENT OF MULTIMODEL MEDIAN CLIMATE CHANGE. Figure 6 presents the air temperature ensemble projections as 20-year moving averages for the 2021-2099 period with respect to present conditions (1971-2000) for Belarus. The individual models project a general increase in air temperature from 1 to 7°C. Under the RCP2.6 scenario, the projected ensemble median exhibits an increase in the annual mean air temperature of up to 1.5°C by the middle of the century, followed by a subsequent decrease of 0.5°C by the end of the century.

The largest growth under RCP2.6 is detected in the winter and spring (from 0.5 to 2.0°C) in different decades of the current century, while the smallest growth is observed in the summer. For winter, spring, and autumn, the temperature is expected to rise until the middle of the century, followed by a projected decrease until the end of the century. A gradual increase in air temperature of up to 1.0°C is projected for the summer.

The RCP4.5 ensemble scenario estimates an increase in the annual mean temperature ranging from 1.0°C to 2.8°C (from the beginning to the end of the century). The RCP8.5 scenario projections show an increase in the annual mean temperature ranging from 1.2°C at the beginning of the study period to 5.2°C at the end of the century. A gradual increase in winter and spring temperatures is expected to equal 4.5-5.5°C, and that of the summer-autumn period equal to 3.5-4.2°C.

ESTIMATES OF THE PROJECTED EXTREMES. Significant changes in winter extremes were detected for frost and ice days and the maximal frost period length, and in summer extremes for hot and summer days and for tropical nights.

The number of frost days is expected to decrease from 3-9 days during the current century under the RCP2.6 scenario to 4-33 days under the RCP4.5 and RCP8.5 scenarios. The number of ice days is also projected to decrease by 3-16 days under the RCP2.6 scenario, 4-18 days under the RCP4.5 scenario and

7-31 days under the RCP8.5 scenario. The maximum frost period length decreases from 7-17 days under the RCP2.6 scenario to 9-30 days under the RCP8.5 scenario. The winter indices generally exhibit maximal values for the 2041-2050 period under the RCP2.6 scenario and at the end of the century under the RCP4.5 and RCP8.5 scenarios.
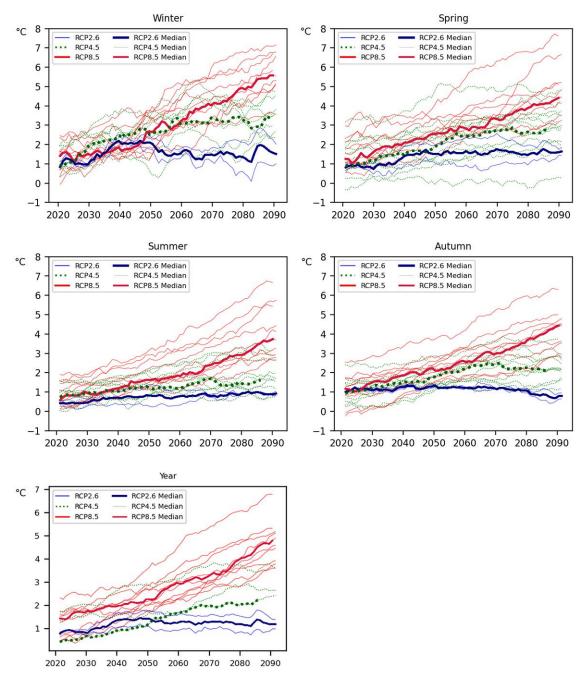


Fig. 6. Projected changes in air temperature in Belarus for the 2021-2099 period with respect to 1971-2000 as the 20-year running means.

During the summer, the number of hot days is expected to rise by a range from 1 day per season during the current century under the RCP2.6 scenario to up to 12 days under the RCP8.5 scenario. The number of summer days will increase by 3-21 days according to the RCP4.5 and RCP8.5 scenarios, while the num-

ber of tropical nights may rise by 2-8 days per season (more than twice the number under current conditions) after 2051-2060 under the RCP8.5 scenario.

The ice and frost days are projected to decrease during autumn and spring for every RCP scenario. Moreover, in autumn, an increase in summer days of up to 5 days per season is observed in the second half of the century under the RCP8.5 scenario.

## 7.2. Total precipitation

PECULIARITIES OF CURRENT CLIMATE CHANGES. The moisture regime in Belarus has changed in the recent decades. The mean precipitation exhibits a nonsignificant increase in the north (up to 5%) and southeast (up to 7%), while no changes are observed in the other regions of Belarus. The largest changes in precipitation are detected in the winter and may be explained by the atmospheric circulation peculiarities in the Atlantic-European sector (Partasenok et al. 2014). In the summer, an increase in precipitation occurred in July. Additionally, enhanced precipitation extremes are marked: the rainfall duration decreased while the absolute maximum precipitation amounts increased, particularly in the southern and central regions of the country. Despite the rise in precipitation, dry conditions are currently intensifying in Belarus, particularly during the growing season (Danilovich 2021).

ASSESSMENT OF MULTIMODEL MEDIAN CLIMATE CHANGE. The different ensemble scenarios project an increase in precipitation across Belarus in all seasons. As shown in Figure 7, individual models projected increases in the winter and spring of the 2021-2099 period with respect to present conditions (1971-2000) for Belarus. The estimated growth of the multimodel median precipitation in the winter and spring exceeds 10 kg·m$^{-2}$ (8%) under the RCP2.6 scenario, and reaches 20 kg·m$^{-2}$ (15%) and 40 kg·m$^{-2}$ (30%) under the RCP4.5 and RCP8.5 scenarios, respectively. In summer and autumn, changes in precipitation are more complex: the majority of simulations exhibit an increase in the seasonal precipitation totals of up to 10 kg·m$^{-2}$ (4-6%); and mid-century decreases are projected under the RCP2.6 scenario. The higher-resolution EUR-11 projections tend to estimate stronger increases in mean annual precipitation compared to the coarser EUR-44 counterparts in previous studies (Partasenok et al. 2015; Danilovich, Geyer 2018).

ESTIMATES OF THE PROJECTED EXTREMES. The number of precipitation days is projected to increase in the winter and spring by 1-3 days. In the summer and autumn, the deviations in the precipitation days are larger (up to 4 days) than in the cold season but have no clear increasing or decreasing trends during the current century. The largest deviations in the precipitation days during the century are projected under the RCP2.6 scenario.

An increase of 1-2 wet days is expected in the winter and spring under the RCP2.6 scenario and 2-4 days under the RCP4.5 and RCP8.5 scenarios. Negative deviations of up to 1-3 wet days are projected during summer and autumn.
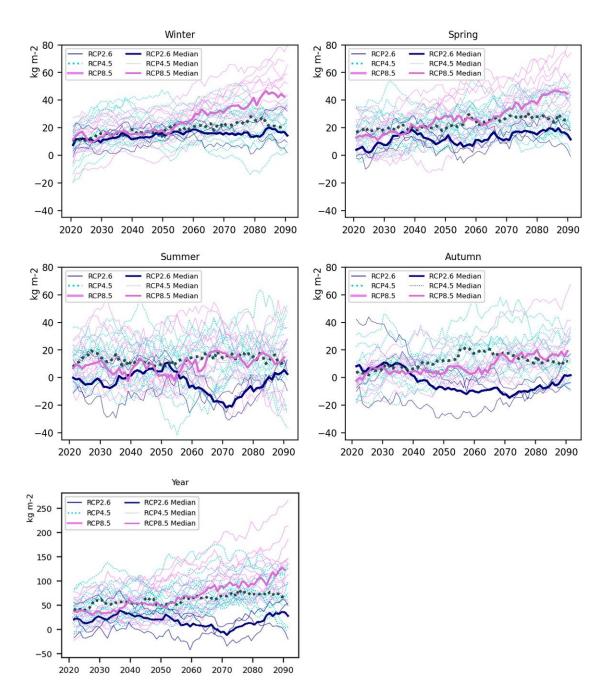
Fig. 7. Projected changes in precipitation for Belarus during the 2021-2099 period with respect to 1971-2000 as 20-year running means.

A substantial increase is particularly apparent for the intense precipitation days, particularly in cold seasons. Signal strengths depend on the forcing and are most distinct for RCP8.5-driven ensemble scenarios.

A projected intensification of extreme precipitation is expected over Belarus. For example, the 95th percentile of precipitation increases in all seasons but is stronger in spring; with a rise of 3-6 kg·m-2 under the RCP4.5 scenario and 3-8 kg·m-2 under the RCP8.5 scenario (Fig. 8).

Fig. 8. The ensemble changes in the 95th percentile of precipitation for 2041-2099 with respect to present conditions (1971-2000) for Belarus. The year on the x-axis represents the start of each 20-year subperiod.

Figure 9 reveals the maximal dry period length changes to be the most complex. No significant trends are observed for the winter season, while the spring exhibits substantial decreases. The largest increase in the maximal dry period length is expected in the summer and autumn (with the exception of several decades) under the RCP2.6 scenario. The largest increase and decrease are projected under the RCP2.6 scenario.

The models project stronger relative increases in single-day rainfall events compared to multiday precipitation spells.



Fig. 9. Ensemble changes in the maximal dry period length for 2041-2099 with respect to present conditions (1971-2000) for Belarus. The year on the x-axis represents the start of each 20-year subperiod.

## 7.3. Snow

PECULIARITIES OF CURRENT CLIMATE CHANGES. The changes in the snow regime strongly depend on cold-period temperature fluctuations. Following the positive tendency of air temperature in Belarus in recent decades, particularly in winter, the duration of solid precipitation has declined in recent decades by 11-26 hours per month or up to 5 days per cold season in the north and by 11-47 hours or up to 3-24 days in central and southern Belarus (Melnik 2019). The largest negative trend in falling snow duration occurs in January, at 20 hours per decade. In contrast, the liquid precipitation duration has increased for the entire country. The snow water equivalent (SWE) tends to decrease by more than 20 mm (25%) per cold season in the north and center, with slight changes in southern Belarus.

ASSESSMENT OF MULTIMODEL MEDIAN CLIMATE CHANGE. The general decrease is distinct for all models and scenarios in Belarus. However, several decades in the second half of the century exhibit increases under the RCP2.6 scenario. In the near-term period (2031-2050), the snow precipitation means is reduced by approximately 20 $kg \cdot m^{-2}$ per season. However, later snowfall is expected to decrease by up to 7-10 $kg \cdot m^{-2}$ per season. A significant reduction of 11-27 $kg \cdot m^{-2}$ per season is detected under the RCP4.5 scenario, and 9-47 $kg \cdot m^{-2}$ per season under the RCP8.5 scenario.

ESTIMATES OF THE PROJECTED EXTREMES. Among the snow precipitation climate indices, significant changes were detected for the numbers of precipitation days and wet days.

The snow precipitation days are expected to change by 1-10 days under the RCP2.6 scenario, with the largest negative deviation in the near-term period of 2031-2050 and at the end of the century, from 2091-2099. The decrease in snow precipitation days is projected to be 8-18 days under the RCP4.5 scenario and 4-32 days under the RCP8.5 scenario.

The number of snow wet days is projected to decrease by 2-5, 4-8 and 3-14 days under the RCP2.6, RCP4.5 and RCP8.5 scenarios, respectively.

## 7.4. Wind

PECULIARITIES OF CURRENT CLIMATE CHANGES. The wind regime in Belarus, which is influenced by atmospheric circulation over Europe and the Atlantic Ocean, is determined by baric center activity. During the cold season, winds from the west and southwest prevail (repeatability 45-50%), whereas those from the east (15%), northwest (9-12%), and north (5-8%) are less dominant. In the summer, westerly (NW+W+SW) winds prevail (50%), with wind repeatability from the east up to 30% and from the south at 12%.

The wind strength has decreased by 0.9-1.0 $m \cdot s^{-1}$ since the 1970s over the territory of Belarus, and the mean annual wind speed varies from 2.5 to 2.8 $m \cdot s^{-1}$. The absolute maximum wind gust has also declined by 1.2 $m \cdot s^{-1}$ in the central and southern regions of the country, while no changes are observed in northern Belarus. The negative trend of the maximum wind gust is approximately equal to 0.1-0.2 $m \cdot s^{-1}$ per decade since the 1970s.

ASSESSMENT OF MULTIMODEL MEDIAN CLIMATE CHANGE. The ensemble reveals slight nonsignificant changes in seasonal and annual wind speeds. The overall change in wind speed varies from 0.2 to −0.4 m·s⁻¹ in all seasons (Fig. 10).
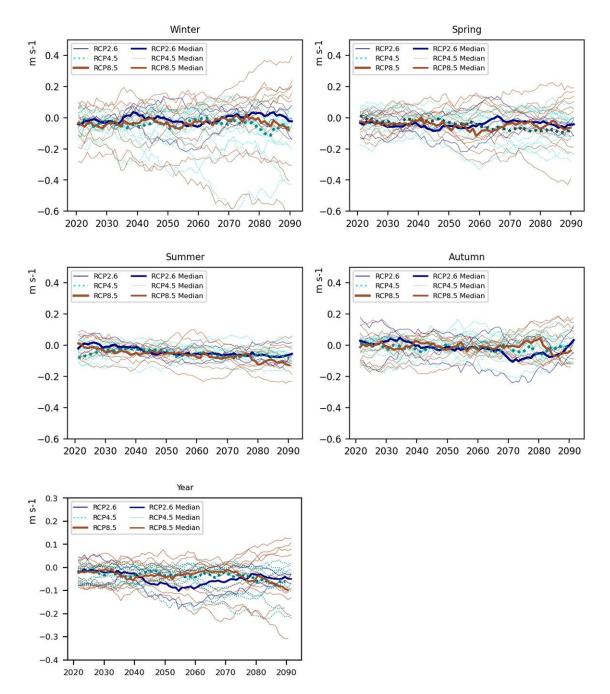


Fig. 10. Projected changes in wind over Belarus for the 2021-2099 period with respect to 1971-2000 as 20-year running means.

The ensemble median is reduced by 0.05 m·s⁻¹ in the winter during the current century, with a more marked decrease of up to 0.1 m·s⁻¹ projected up until the end of the century in spring and summer. The wind speed change in autumn is expected to stay close to the norm (1971-2000) under the RCP4.5 and RCP8.5 scenarios and deviate under the RCP2.6 scenario, growing by 0.05 m·s⁻¹ in the recent decades to

0.15 m·s⁻¹ in the middle of the century. The maximal wind speed is expected to increase in the second half of the century by 0.1-0.2 m·s⁻¹ and decrease in summer by 0.1-0.25 m·s⁻¹. In autumn, the maximal wind speed will vary strongly under RCP2.6, with an increase of 0.25 m·s⁻¹ in the first half of the current century and subsequent reduction of 0.15-0.5 m·s⁻¹. RCP4.5 and RCP8.5 exhibited nonsignificant variations in the maximal wind speed in autumn.

ESTIMATES OF THE PROJECTED EXTREMES. A significant climate change signal is detected for strong-breeze days and storm days.

Under the RCP2.6 scenario, the number of strong breeze days increases by 2 days in winter and autumn, and decreases by 1-3 days in spring and summer. Mid-century strong breeze days are expected to increase in the winter for a short period under the RCP4.5 scenario. Other seasons are projected to experience changes ranging between 1.0 and 1.5 days, with the largest negative values in the summer. The RCP8.5 scenario predicts a gradual increase of up to 2 strong-breeze days in winter and spring, while in the summer, a decrease of 3 days is detected in the second half of the current century.

The climate change signal is stronger for storm days during the current century (2021-2099) under the RCP2.6 scenario. A general decrease in the number of storm days of 0.5-1 days is observed in the winter, spring and autumn, with the largest magnitude in the winter. In autumn, an increase in the number of storm days of 0.5-1 days is expected in the first half of the century. The changes in storm days are nonsignificant under the other scenarios.

## 8. Discussion

This study estimates the current and future changes in mean and extreme values of air temperature, liquid and solid precipitation, and wind over the territory of Belarus. Table 4 summarizes the study results for the territory of Belarus and the comparative climate characteristics for neighboring countries.

Regional climate assessments typically consider the macro-region in order to comprehensively demonstrate the climate change trends in the study domain. However, this may result in the loss of some climate change features in smaller regions (countries).

The air temperature estimates in Europe are robust in their conclusions and indicate a gradual increase over the region. The mean annual air temperature in Europe was observed to rise by 1.3°C in 2002-2011 and 1.6°C in 2009-2019 (C3S 2020). The air temperature increased by 1.3°C during 1989-2018 in Belarus, slightly differing from that in neighboring countries. Similar increasing trends in air temperature are detected (from 1.2 to 1.5°C) in the European part of Russia (Kryshnakova 2008; Roshydromet 2008), Ukraine (Shevchenko 2019) and Poland in spring (Czernecki 2017); while in Latvia (Klavins 2002; Summary Report 2017), Lithuania (Lithuania's 5th National Communication 2010) and Poland (Fortuniak et al. 2001; Kożuchowski, Żmudzka 2001), lower mean yearly air temperature changes of 0.7-0.9°C are observed, yet they were analyzed for a longer period (1961-2010).

The mean annual precipitation changes exhibited nonsignificant and generally positive deviations within 5-10% from climatological norms in all neighboring countries (Latvia`s 4th National Communication 2006; Roshydromet 2008; Summary Report 2017; Tripolskaja 2013; Jaagus 2018; Shevchenko 2019; Szwed 2019) and Belarus, while positive changes in intense precipitation were more marked (Roshydromet 2008; Reckermann 2011; Summary Report 2017; Balabukh 2018a; Pińskwar et al. 2018a).

With regards to precipitation, the territory of Belarus is located in the neutral zone between northern Europe (with a general increase in mean annual precipitation) and southern Europe (where drying conditions have increased since the second part of the 20th century). Despite the nonsignificant changes in the mean annual precipitation across recent decades over Belarus, the maximal precipitation totals have increased significantly in the summer by 15-25%. Moreover, drought frequency has also increased by up to 3-19% across the country (Danilovich 2021). Analysis of drying conditions over Eastern Europe based on the SPI (standardized precipitation index) and SPEI (standardized precipitation evapotranspiration index) revealed nonsignificant changes for the territory of Belarus (Jaagus et al. 2018), while SPI repeatability demonstrated a significant increase in drying conditions on the majority of Belarussian meteorological stations.

Snow precipitation and snow cover have declined in neighboring countries in recent decades due to temperature increases (Latvia`s 4th National Communication 2006; Roshydromet 2008; Rimkus 2014; Szwed 2017; Balabukh 2018).

In terms of wind regime, the mean and maximal speeds decreased in neighboring countries (Roshydromet 2014; Summary Report 2017; Balabukh 2018b), while whirlwinds and tornados in Poland (Project Klimada, Kożuchowski 2011) and extreme squalls in Ukraine (Balabukh 2018b) have become more frequent.

The regional assessments of climate projections for Poland, Lithuania, Latvia, Ukraine, the European part of Russia and Belarus generally confirm that future climate changes will follow current climate changes, which have been recorded since the second part of the previous century (e.g., increases in air temperature by 1 to 6°C over neighboring territories). The projected increase in Belarus territory is expected to be similar to that in Latvia (Summary Report 2017), Lithuania (Kriaučiūniene 2008, 2018) and Ukraine (Christensen 2007; Met Office 2010; Balabukh 2018b), with variations from 2.5 to 5.5°C by the end of the current century. The expected air temperature increases in Poland (Mezghani et al. 2016a) and the European part of Russia (Shkolnik et al. 2006; Kokorev 2013) are smaller than those in other countries by 1.0-3.8°C, with a projected total of 1-4°C.

The mean annual precipitation is projected to exhibit a nonsignificant growth in Lithuania (Kriaučiūniene 2008), while significant increases are expected of up to 10-15% in Poland, Latvia, Ukraine and Belarus, (Christensen 2007; Met Office 2010; Mezghani et al. 2016; Boychenko 2017; Summary Report 2017), and up to 20% in the European part of Russia (Shkolnik et al. 2006). A noticeable increase in intense precipitation is expected for all neighboring countries (Bukantis 2010; Kattsov 2017; Summary Report 2017; Pińskwar, Dobler 2018).

Snow projections demonstrated a substantial reduction in snow cover over the European part of Russia (Mokhov 2008) and in Belarus. Moreover, a complete lack of snow cover is expected in the western and southern neighbors of Belarus (Helcome 2006).

Wind speed projections are diverse among countries, with increases of 5-10% in the Baltic Sea basin (Nikulin 2011), while a rise of 4-13% and 0-6% is estimated in Latvia under the RCP4.5 and RCP8.5 scenarios (Summary Report 2017). At the same time, wind speed will continue to decrease in the future over Belarus and the European part of Russia (Kattsov 2017). This may be explained by northerly cyclone track shifts (Partasenok et al. 2014) and their continuation in the future.

Table 4. Assessments of current and projected climate changes in neighboring countries of Belarus

| Country | Current climate changes | | | | | Projected climate changes to the end of the century | | | | |
|---|---|---|---|---|---|---|---|---|---|---|
| | Annual temperature | Annual precipitation | Intense precipitation in summer | Wind | Snow | Annual temperature | Annual precipitation | Intense precipitation | Snow | Wind |
| Belarus | +1.3°C (1988-2018) | Nonsignificant increase by 5-7% (1988-2018) | Max precipitation increased (1988-2018) | Mean wind speed decreased since 1970s | Snow depth decreased<br><br>SWE decreased by 25% (1989-2018) | Increase: by +0.5-1.5°C (RCP2.6) by +2.8°C (RCP4.5) by +5.2°C (RCP8.5) | Increase by 10-15% (RCP4.5 and RCP8.5) | Increase in 95th percentile by 4-7 mm | Decrease in snow precipitation days by 10-30 days | Nonsignificant decrease in summer and yearly wind, increase in strong-wind days |
| Poland | +0.8°C (second part 21st century)<br><br>+1.4°C (in March-May 1951-2010) | No significant changes (1951-2013) | Max precipitation increased | Increase in whirlwinds and tornados | Mean and max snow depth decreased (1991-2013) | +1-2°C (RCP4.5) up to +4°C (RCP8.5) | Increase by 6–10% (RCP4.5) 8–16% (RCP8.5) | 95th and 99th percentile precipitation increases | Decrease up to a complete lack of snow cover | Increase by 5-10% in BS; strengthening north of 45°N |
| Lithuania | +0.7-0.9°C (1991-2006) | Nonsignificant increase (1991-2006) | Slight increase (1991-2006) | - | Decrease in days with snow cover and max snow depth (1991-2006) | +4.4-4.9°C (A2) +2.6-2.7°C (B1)<br><br>+1.2-6.8°C (RCP4.5 and RCP8.5) | No clear trend<br><br>Nonsignificant changes | Heavy precipitation events increase by up to 30% (A1B) | | |
| Latvia | +0.8-1.4°C (last century)<br><br>+0.7°C (1961-2010) | Increase since 1950s<br><br>6% increase (1961-2010) | Heavy prec. days increased by 2 days in 1961-2010 | Decreased by 8% since 1966 | Decrease (1961-2010) | +3.5°C (RCP4.5) +5.5°C (RCP8.5) | +13-16% (RCP4.5 and RCP8.5) | Heavy prec. days increase by 3-5 days | | Mean wind speed increase: 4-13% (RCP4.5) 0-6% (RCP8.5) |
| Ukraine | +0.7-1.2°C (1991-2010) | +−8% changes | Increased during 1971-2010 | Extreme squalls increased | Snowfalls decreased in 1970s, and increased from 1990s | +2.3-5.3°C (RCP4.5)<br><br>+1.1-1.4°C (A1B) | 0-15% (RCP4.5)<br><br>10-15(±5)% | – | – | – |
| Russia | +1.5°C (1976-2005)<br><br>+1.33°C (1976-2006) | +7.2 mm/10 years for the period 1976-2006 | Increase in the number of days with heavy rainfall (snowfall) | Decrease since 1970s | Decrease in snow depth | +3.2°C (B2)<br><br>+3.5-3.8°C (RCP8.5) | +20% (B2)<br><br>+10-20% (A1B) | Increase in daily precipitation exceeding 90th summer percentile threshold | Substantial reduction in snow cover | Considerable decrease in wind by 2050 |

## 9. Summary

This study presents the results of current and future climate changes over the territory of Belarus. We attempted to connect the regional peculiarities of ongoing climate changes and projected means of air temperature, precipitation and wind. While Belarus is an agrarian country, adaptation to climate change is part of the country's sustainable development strategy. The climate information based on in situ data and numerical modelling in the present study is in high demand. The main tendencies of current and projected climate changes are summarized below.

TEMPERATURE: In recent decades, a temperature increase of 1.3°C has occurred over the territory of Belarus. The largest increase in air temperature (2.1-2.4°C) is detected in the cold season. Increases in minimum temperatures exceed those of maximum temperatures in the winter, while no equivalent difference is observed for summer.

The different ensemble scenarios project an increase of 1-5°C in the mean annual air temperature until the end of the current century. The largest growth (1-6°C) is projected in the cold season, while the growth in the warm season is projected to be 1-4°C. The RCP8.5 scenario demonstrates the largest changes. For winter, spring, and autumn, the temperature is expected to rise until the middle of the century, followed by a subsequent decrease.

TOTAL PRECIPITATION: Mean annual totals were observed to increase by up to 57%, with summer extremes in precipitation of up to 20-25%. However, drying conditions also intensified in Belarus, particularly during the growing season.

An increase in precipitation across Belarus was projected in all seasons. The mean annual precipitation is expected to rise by 30-120 kg·m$^{-2}$ or by 5-15% at the end of the century. Models simulate increases in single rainfall events compared to multiday precipitation events. The 95$^{th}$ percentile of precipitation is observed to rise in all seasons by 4-7 kg·m$^{-2}$. In summer and autumn, the largest increase in maximal dry period length is estimated as 0.5-1.5 days, with the exception of some decades under the RCP2.6 scenario.

The largest deviations in the precipitation days and dry periods during the century are projected for the RCP2.6 scenario.

SNOW: In recent decades, the winter precipitation amount increased in northern Belarus, while no significant changes were observed in the center and south of the country. The duration of solid precipitation decreased by 5-23 days, particularly in the south, and the duration of liquid precipitation in winter increased over the entire territory of Belarus.

The models projected a general decrease in snowfall of 10-45 kg·m$^{-2}$ in Belarus for the current century. However, increases were detected during the second half of the century under the RCP2.6 scenario.

Among the climate indices used for snow precipitation, the most significant negative deviations (by 10-35 days) were detected for the numbers of precipitation days and wet days.

WIND: The wind strength has declined by 0.9-1.0 m·s$^{-1}$ since the 1970s over the territory of Belarus.

The ensemble models reveal slight nonsignificant changes from 0.2 to −0.4 m·s⁻¹ in seasonal and annual wind strength. In addition, a significant climate change signal in the wind regime is detected for strong-breeze days and storm days. In general, all models determined the number of strong-breeze days to increase in winter and summer by 2-2.5 and 3 days, respectively. Furthermore a 1 day decrease in the number storm days was observed in the winter, and a 1 day increase for autumn.

## Acknowledgements

## References

Alisov B.P., 1936, Geographical types of climates, Meteorology and Hydrology, (in Russian), 1, 16-25.

Balabukh V., Lavrynenko O., Bilaniuk V., Mykhnovych A., Pylypovych O., 2018a, Extreme weather events in Ukraine: Occurrence and changes, [in:] Extreme Weather, IntechOpen, 85-106, DOI: 10.5772/intechopen.77306.

Balabukh V., Malytska L., Yagodinets S., Lavrynenko O., 2018b, Projections of changes climatic mean and extreme parameters of thermal regime by the middle of the 21st century in Ukraine, Nature Management, (in Russian), 1, 97-113.

Beck H.E., Zimmermann N.E., McVicar T.R., Vergopolan N., Berg A., Wood E.F., 2018, Present and future Köppen-Geiger climate classification maps at 1-km resolution, Scientific Data, 5 (1), DOI: 10.1038/sdata.2018.214.

Belhydromet, 2019, State climate cadastre of the Republic of Belarus, technical report.

Boychenko S., Voloshchuk V., Movchan Y., Serdjuchenko N., Tkachenko V., Tyshchenko O., Savchenko S., 2016, Features of climate change on Ukraine: scenarios, consequences for nature and agroecosystems, Proceedings of the National Aviation University, 69 (4), 96-113, DOI: 10.18372/2306-1472.69.11061.

Bukantis A., Rimkus E., Kazys J., 2010, Heavy precipitation events in Lithuania, [in:] 10th EMS Annual Meeting, 10th European Conference on Applications of Meteorology (ECAM), Abstracts.

C3S, 2020, European state of the climate 2019, Climate Bulletin, Copernicus Climate Change Service, available online at https://climate.copernicus.eu/ESOTC/2019 (data access 07.07.2021).

Christensen J., Hewitson B., Busuioc A., 2007, Regional climate projections, [in:] Climate Change 2007: The Physical Science Basis, IPCC, available online at https://www.ipcc.ch/report/ar4/wg1/regional-climate-projections/ (data access 07.07.2021).

Çzernecki B., Miętus M., 2017, The thermal seasons variability in Poland, 1951-2010, Theoretical and Applied Climatology, 127 (1), 481-493, DOI: 10.1007/s00704-015-1647-z.

Danilovich I., Kvach A., Zhuravovich L., Piskunovich N., 2021, Current changes of precipitation in warm season and streamflow formation during low-flow period over territory of Belarus, Nature Management, (in Russian), 1, 22-33.

Danilovich I.S., Geyer B., 2018, Assessment of possible future changes of air temperature and rainfall by decades of the current century for the territory of Belarus on the basis of numerical modelling, Natural Resources, (in Russian), 1, 102-114.

Danilovich I.S., Melnik V.I., Geyer B., 2020, The current climate changes in Belarusian Polesje region: factors, consequences, projections, Journal of the Belarusian State University, (in Russian), DOI: 10.33581/2521-6740-2020-1-3-13.

Flato G., Marotzke J., Abiodun B., Braconnot P., Chou S.C., Collins W., Cox P., Driouech F., Emori S., Eyring V., Forest C., Gleckler P., Guilyardi E., Jakob C., Kattsov V., Reason C., Rummukainen M., 2013, Evaluation of climate models, [in:] Climate Change 2013 – The Physical Science Basis, IPCC, DOI: 10.1017/CBO9781107415324.020.

Fotruniak K., Kożuchowski K., Żmudzka E., 2001, Trendy i okresowość zmian temperatury powietrza w Polsce w drugiej połowie XX wieku, Przegląd Geofizyczny, 46 (4), 283-303.

Frich P., Alexander L., Della-Marta P., Gleason B., Haylock M., Klein T., Peterson T., 2002, Observed coherent changes in climatic extremes during second half of the twentieth century, Climate Research, 19, 193-212, DOI: 10.3354/cr019193.

Govorkova V., Kattsov V., Melesko V., Pavlova T., Shkolnik I., 2008, Climate of Russia in 21st century. Part 2. Evaluation of validity of CMIP3 atmosphere-ocean general circulation models for projecting climate changes over Russia, Russian Meteorology and Hydrology, 32 (8), 5-19.

HELCOM, 2007, Climate change in the Baltic Sea area HELCOM thematic assessment in 2007, Baltic Sea Environment Proceedings, 111, 54 pp.

Jaagus J., Briede A., Rimkus E., Sepp M., 2018, Changes in precipitation regime in the Baltic countries in 1966-2015, Theoretical and Applied Climatology, 131, 433-443, DOI: 10.1007/s00704-016-1990-8.

Jacob D., Petersen J., Eggert B., Alias A., Christensen O.B., Bouwer L.M., Braun A., Colette A., Déqué M., Georgievski G., Georgopoulou E., Gobiet A., Menut L., Nikulin G., Haensler A., Hempelmann N., Jones C., Keuler K., Kovats S., Kröner N., Kotlarski S., Kriegsmann A., Martin E., van Meijgaard E., Moseley C., Pfeifer S., Preuschmann S., Radermacher C., Radtke K., Rechid D., Rounsevell M., Samuelsson P., Somot S., Soussana J.-F., Teichmann C., Valentini R., Vautard R., Weber B., Yiou P., 2014, EURO-CORDEX: new high-resolution climate change projections for European impact research, Regional Environmental Change, 14 (2), 563-578, DOI: 10.1007/s10113-013-0499-2.

Kattsov V.M., Shkolnik I.M., Efimov S.V., 2017, Climate change projections in Russian regions: The detailing in physical and probability spaces, Russian Meteorology and Hydrology, 42 (7), 452-460, DOI: 10.3103/S1068373917070044.

Klavins M., Briede A., Rodinov V., Kokorite I., Frisk T., 2002, Long-term changes of the river runoff in Latvia, Boreal Environment Research, 7, 447-456.

Kokorev V., Anisimov O., 2013, Construction of an optimized ensemble of climate projections to assess the impact of climate change in Russia, [in:] Problems in environmental modelling and monitoring of ecosystems, (in Russian), 131-153.

Kotlarski S., Keuler K., Christensen O.B., Colette A., Déqué M., Gobiet A., Goergen K., Jacob D., Lüthi D., van Meijgaard E., Nikulin G., Schär C., Teichmann C., Vautard R., Warrach-Sagi K., Wulfmeyer V., 2014, Regional climate modeling on European scales: A joint standard evaluation of the EURO-CORDEX RCM ensemble, Geoscientific Model Development, 7, 1297-1333, DOI: 10.5194/gmd-7-1297-2014.

Kożuchowski K., 2011, Klimat Polski. Nowe spojrzenie, Wydawnictwo Naukowe PWN, Warszawa, 296 pp.

Kożuchowski K., Żmudzka E., 2001, Ocieplenie w Polsce: skala i rozkład sezonowy zmian temperatury powietrza w drugiej połowie XX wieku, Przegląd Geofizyczny, 46 (1-2), 81-90.

Kriauciuniene J., Meilutyte-Barauskiene D., Kažys E.R.J., Vincevicius A., 2008, Climate change impact on hydrological processes in Lithuanian Nemunas river basin, Baltica, 21 (1-2), 51-61.

Kryshnyakova O.S., Malinin V.N., 2008, Peculiarities of climate warming of the European territory of Russia in modern conditions, Society. Environment. Development, 7 (2), 115-124.

Loginov V., 2008, Global and regional climate changes: drivers and consequences, Minsk, Terra-System, (in Russian), 494 pp.

Loginov V., Mikutskiy V., Kajdan E., 2000, A selection of atmospheric circulation model for regional forecast of climate change, (in Russian), Nature Management, 6, 30-31.

Lysenko S.A., Chernyshev V.D., Kalyada V.V., 2019, A grid archive of meteorological data of the Republic of Belarus and the opportunity of its use in research of spatial-temporal peculiarities of climate changes, Nature Management, (in Russian), 1, 17-28.

Meleshko V., Kattsov V., Govorkova V., Sporyshev P., Shkol'nik I., Shneerov B., 2008, Climate of Russia in the 21st century. Part 3. Future climate changes calculated with an ensemble of coupled atmosphere-ocean general circulation cmip3 models, Russian Meteorology and Hydrology, 33 (9), 541-552.

Melnik V., Buyakov I., Chernyshev V., 2019, Changes in the amount and type of atmospheric precipitation during the cold period on the territory of Belarus in the conditions of modern climate warming, (in Russian), Nature Management, 2, 44-51.

Melnik V., Danilovich I., Kuleshova I., Komarovskaya E., Melchakova N., 2018, Assessment of agroclimatic resources of the territory of Belarus during 1989-2015, (in Russian), Natural Resources, 2, 88-101.

Melnik V., Sokolovskaya Y.A., Komarovskaya E., 2017, Possible changes of climatic and agroclimatic characteristics in the 21st century over territory of Belarus and their influence on agriculture, Natural Resources, (in Russian), 2, 118-125.
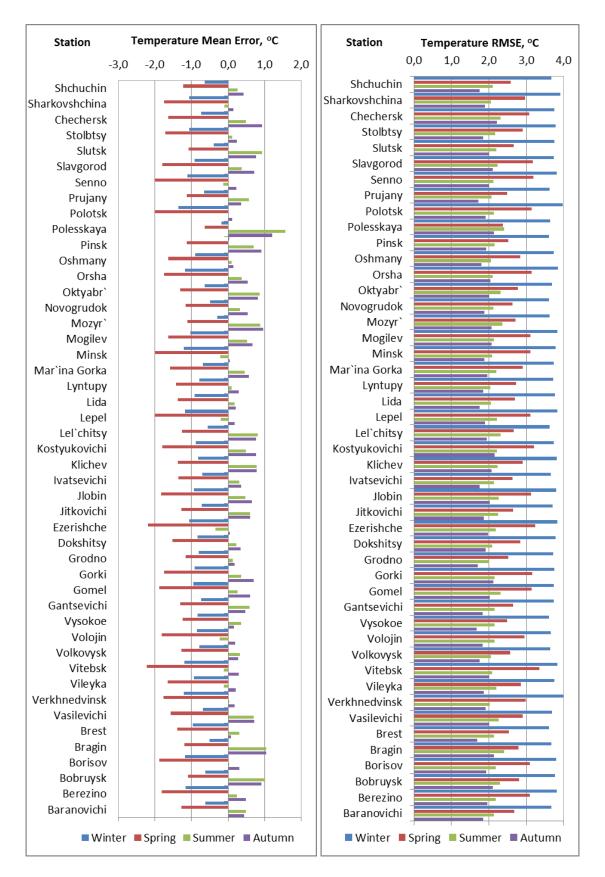
Met Office, 2010, Climate: Observations, projections and impacts. Russia, Report of Met Office Hadley Centre, 138 pp.

Metzger M.J., Bunce R.G.H., Jongman R.H.G., Mücher C.A., Watkins J.W., 2005, A climatic stratification of the environment of Europe, Global Ecology and Biogeography, 14 (6), 549-563, DOI: 10.1111/j.1466-822X.2005.00190.x.

Mezghani A., Dobler A.A., Haugen J.J.E., 2016, CHASE-PL climate projections: 5-km gridded daily precipitation and temperature dataset (CPLCP-GDPT5).

Ministry Latvia, 2006, Fourth National Communication of the Republic of Latvia to the United Nations Framework Convention on Climate Change, Ministry of the Environment of the Republic of Latvia, 160 pp.

Mokhov I., Eliseev A., 2012, Modeling of the global climatic changes in XX-XXIII centuries under new scenarios of anthropogenic forcing (rcp), Proceeding of Russian Academy of Sciences, 443 (6), 732-736.

Mokhov I.I., 2008, Possible regional consequences of global climate changes, Russian Journal of Earth Sciences, 10 (ES6005), DOI: 10.2205/2007ES000228.

Moss R.H., Edmonds J.A., Hibbard K.A., Manning M.R., Rose S.K., van Vuuren D.P., Carter T.R., Emori S., Kainuma M., Kram T., Meehl G.A., Mitchell J.F.B., Nakicenovic N., Riahi K., Smith S.J., Stouffer R.J., Thomson A.M., Weyant J.P., Wilbanks T.J., 2010, The next generation of scenarios for climate change research and assessment, Nature, 463 (7282), 747-756, DOI: 10.1038/nature08823.

Nikulin G., Kjellström E., Hansson U., Strandberg G., Ullerstig A., 2011, Evaluation and future projections of temperature, precipitation and wind extremes over Europe in an ensemble of regional climate simulations, Tellus A: Dynamic Meteorology and Oceanography, 63 (1), 41-55, DOI: 10.1111/j.1600-0870.2010.00466.x.

Partasenok I., Geyer B., Melnik V., 2015, Assessment of climatic changes in Belarus according to the EURO-CORDEX climate models, (in Russian), Collection of articles of the Hydrometeorological Research Center of the Russian Federation, 358, 99-111.

Partasenok I.S., Groisman P.Y., Chekan G.S., Melnik V.I., 2014, Winter cyclone frequency and following freshet streamflow formation on the rivers in Belarus, Environmental Research Letters, 9 (9), 095005, DOI: 10.1088/1748-9326/9/9/095005.

Pavlova V.N., 2013, Agroclimatic resources and agricultural productivity in Russia according to the new climate scenarios in the xxi century, (in Russian), Proceedings of the Main Geophysical Observatory named after A.I. Voyekov, 569, 20-37.

Pinskwar I., Chorynski A., Graczyk D., Kundzewicz Z.W., 2019, Observed changes in extreme precipitation in Poland: 1991-2015 versus 1961-1990m Theoretical and Applied Climatology, 135 (1), 773-787, DOI: 10.1007/s00704-018-2372-1.

Podgornaya E., Melnik V., Komarovskaya E., 2015, The peculiarities of climate change over territory of Belarus during last decades, (in Russian), The Proceedings of the Hydrometeorological Research Center of the Russian Federation, 358, 112-120.

Reckermann M., Langner J., Omstedt A., von Storch H., Keevallik S., Schneider B., Arheimer B., Meier H.E.M., Hünicke B., 2011, BALTEX – an interdisciplinary research network for the Baltic Sea region, Environmental Research Letters, 6 (4), 045205, DOI: 10.1088/1748-9326/6/4/045205.

Republic of Lithuania, 2010, Lithuania's Fifth National Communication under the United Nations Framework Convention on Climate Change, 134 pp.

Rimkus E., Kažys J., Butkute S., Gecaite I., 2014, Snow cover variability in Lithuania over the last 50 years and its relationship with large-scale atmospheric circulation, Boreal Environment Research, 19, 337-351.

Roshydromet, 2008, Assessment report on climate change and its consequences in Russian Federation. General Summary, Moscow.

Roshydromet, 2014, Second Roshydromet assessment report on the climate change and its consequences in Russian Federation, (in Russian), Moscow.

Shevchenko O., Snizhko S., 2019, Climate change and Ukrainian cities: Manifestations and projections on 21st century based on RCP-scenatios, (in Ukrainian), Bulletin of Taras Shevchenko National University of Kyiv, 2 (75), 11-18, DOI: 10.17721/1728-2721.2019.75.2.

Shkolnik I., Meleshko V., Kattsov V., 2006, MOPossible climate changes in European Russia and neighboring countries by the late 21st century: calculation with the MGO regional model, Russian Meteorology and Hydrology, 3, 1-10.

Siegmund P., Abermann J., Baddour O., Canadell P., Cazenave A., Derksen C., Garreau A., Howell S., Huss M., Isensee K., Kennedy J., Mottram R., Nitu R., Ramasamy S., Schoo K., Sparrow M., Tarasova O., Trewin B., Ziese M., 2019, The global climate in 2015-2019, WMO, available online at https://library.wmo.int/doc_num.php?explnum_id=9936 (data access 07.07.2021).
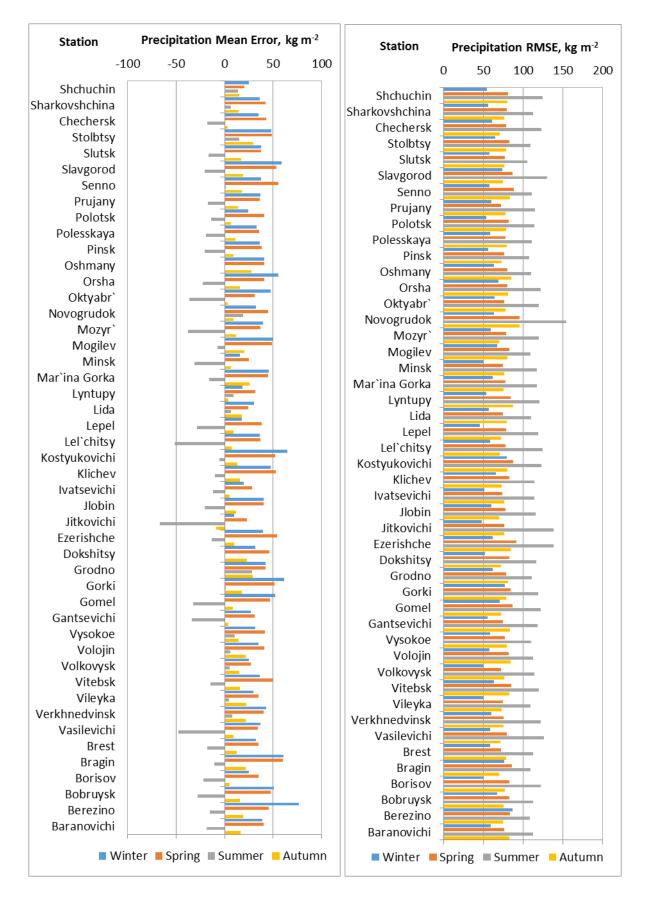
Snezhko S., Obodovsky A., Lopukh P., 2017, Long-term forecast of mountain and lowland runoff to assess their hydropower potential (on the example of the Ukrainian Carpathians and Belarus), (in Russian), Journal of the Belarusian State University. Geography and Geology, 1, 50-61.

Summary Report, 2017, Climate change scenarios for Latvia, Project "Development of Proposal for National Adaptation Strategy, Including Identification of Scientific Data, Measures for Adapting to Changing Climate, Impact and Cost Evaluation", Riga, 17 pp.

Szwed M., 2019, Variability of precipitation in Poland under climate change, Theoretical and Applied Climatology, 135 (3), 100301015, DOI: 10.1007/s00704-018-2408-6.

Szwed M., Pinskwar I., Kundzewicz Z.W., Graczyk D., Mezghani A., 2017, Changes of snow cover in Poland, Acta Geophysica, 65 (1), 65-76, DOI: 10.1007/s11600-017-0007-z.

Taylor K.E., Stouffer R.J., Meehl G.A., 2011, An overview of CMIP5 and the experiment design, Bulletin of the American Meteorological Society, 93 (4), 485-498, DOI: 10.1175/BAMS-D-11-00094.1.

Tripolskaja L., Pirogovskaja G., 2013, Impact of climate variability in Lithuania and Belarus on atmospheric precipitation infiltration: lysimetric study, Zemdirbyste-Agriculture, 100 (4), 369-376, DOI: 10.13080/z-a.2013.100.047.

Van Den Besselaar E.J.M., Klein Tank A.M.G., Van Der Schrier G., Abass M.S., Baddour O., Van Engelen A.F., Freire A., Hechler P., Laksono B.I., Jilderda R., Foamouhoue A.K., Kattenberg A., Leander R., Güingla R.M., Mhanda A.S., Nieto J.J., Suwondo A., Swarinoto Y.S., Verver G., 2015, International climate assessment & dataset: Climate services across borders, Bulletin of the American Meteorological Society, 96 (1), 16-21, DOI: 10.1175/BAMS-D-13-00249.1.

Van Der Linden P., Mitchell J., 2009, Ensembles: Climate change and its impacts: Summary of research and results from the ensembles project, technical report, Met Office Hadley Centre, FitzRoy Road, Exeter EX1 3PB, UK.

Šarauskiene D., Akstinas V., Kriauciuniene J., Jakimavicius D., Bukantis A., Kažys J., Povilaitis A., Ložys L., Kesminas V., Virbickas T., Pliuraite V., 2018, Projection of Lithuanian river runoff, temperature and their extremes under climate change, Hydrology Research, 49 (2), 344-362, DOI: 10.2166/nh.2017.007.

WMO, 2017, WMO Guidelines on the Calculation of Climate Normal, WMO-No. 1203, available at https://library.wmo.int/doc_num.php?explnum_id=4166 (data access 07.07.2021).
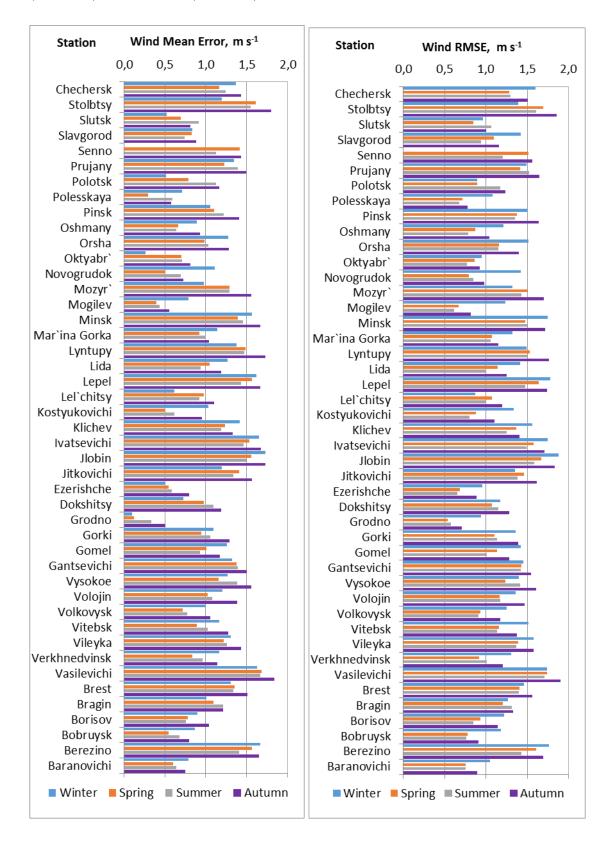
## Appendix A

Evaluation of EURO-CORDEX regional climate model simulations over Belarus for mean air temperature by the root mean square error (right) and mean error (left). Analysis is provided for 14 historical GCM-driven RCMs (1971-2000) and 42 stations (1971-2000).

Evaluation of EURO-CORDEX regional climate model simulations over Belarus for mean precipitation by the root mean square error (right) and mean error (left). Analysis is provided for 14 historical GCM-driven RCMs (1971-2000) and 42 stations (1971-2000).

Evaluation of EURO-CORDEX regional climate model simulations over Belarus for mean wind by the root mean square error (right) and mean error (left). Analysis is provided for 15 historical GCM-driven RCMs (1971-2000) and 42 stations (1971-2000).

# Hydrodynamic flow modeling and effect of roughness on river stage forecasting

Ajaykumar Ramdas Kambekar, Shweta A Patil

Sardar Patel College of Engineering Mumbai

Abstract

In recent times, undesirable climatic conditions have been attributed to climate change. The intensity of rainfall has amplified extremely, causing floods in many areas worldwide. It is desirable to regulate and minimize the consequences of floods and excess downpour. Using geospatial data for the development of hydraulic models and mapping of simulation results has become standard practice for floodplain assessment. The objective of the current investigation is to use one-dimensional floodplain modeling of the Bhima River between Lonikand and Rahu using the RAS-mapper tool (HEC-RAS). The modeled river reach is about 67 km long, near the Pune administrative division of Maharashtra, India. The hydrodynamic flow computations were carried out for the years 2005 and 2017. A total of 595 cross sections along the main river was employed for hydrodynamic flow simulations. In this study, cross-sections and past observed flood data have been used to develop a 1-D integrated hydraulic model of the Bhima River. The simulated water levels are also validated with observed water levels and found to be reasonably correlated.

## 1. Introduction

In recent years the hydrological cycle has been escalating and hastening because of climate change, with consequences that include increasing frequency and magnitude of floods (Kvočka et al. 2015). Floods are the most common and extreme catastrophes in a tropical country like India. Floods cannot be completely avoided, but the accompanying threats could be minimized, if flood prone areas are known in advance (Sahoo, Sreeja 2015). Therefore, recognizing flood risk zones and flood inundation mapping (FIM) are key steps for framing flood management strategies (Sahoo, Sreeja 2015). Correct geometry and flow data inputs are basic requirements of a good hydraulic model, but the performance of the simulations also varies by model type, e.g., one dimensional (1-D), two dimensional (2-D) or combined (1-D & 2-D) types. 1-D models are used extensively to simulate flow in the main river channel and in certain cases very effective in predicting flood extent (Vozinaki et al. 2016). Computational effectiveness and simple parameterization in dealing with flows in large and complex networks have been established by 1-D modelling (Ahmad, Hassan 2011). Horritt and Bates (2002) checked performance of 1-D modelling for hydraulic simulation by carrying out numerous studies and concluded that 1-D models have sufficient skill for good estimation of flood level and flood travel time, so that it can be used for prediction of flood extent. Timbadiya et al. (2012) developed a calibrated HEC-RAS-based model using flood peaks of observed and simulated floods; root mean squared error (RMSE) demonstrated that predicted flood levels were satisfactory. In the present study, a 1-D hydrodynamic model has been developed by using the Hydrologic Engineering Center's River Analysis System (HEC-RAS, V. 5.0.7) developed by the U.S. Army Corps of Engineers (USACE).

## 2. Governing equations

$$\frac{\delta A}{\delta t} + \frac{\delta Q}{\delta x} - q = 0 \qquad \qquad \text{Continuity equation} \qquad (1)$$

$$\frac{\delta Q}{\delta t} + \frac{\delta}{\delta x}\left(\frac{\beta Q^2}{A}\right) + g * A * \left(\frac{\delta h}{\delta x} + S_f\right) = 0 \qquad \text{Momentum equation} \qquad (2)$$

where: $Q$ – discharge [m³/sec]; $A$ – cross-sectional area [m²]; $g$ – acceleration due to gravity [m/sec²]; $\beta$ – momentum correction factor; $h$ – elevation of the water surface(stage) in meters above a specified datum; $s_o$ – bed slope (Longitudinal channel bottom slope); $t$ – temporal coordinate; $x$ – longitudinal coordinate.

## 3. Numerical solution methods

Numerical techniques for the solution of expanded Saint-Venant equations can be given by implicit finite difference techniques with the most widely used Preissmann technique. In this technique all derivative terms and other parameters are calculated by using unknowns at the forward timeline $(j+1)$ in $x$-$t$ grid as shown below.



Fig. 1. The distance-time grid to developed implicit finite difference scheme.

In this scheme, grid size is taken as $(i, j)$ where: $i$ is the space interval; $j$ is the time interval, and the four grid points from the $(j)$th and $(j+1)$th timelines are taken to approximate for the differential equation. A weighing factor, $(\theta = 0.5)$ is used in the approximation of all terms of the equation except for the time derivatives in order to adjust the influence of the points $(i)$ and $(i+1)$. Partial differential equations of continuity and momentum are obtained as a result of approximation by the Preissmann implicit finite difference scheme.

Water level $(h) = f(A, B)$, where $A$ is the cross-sectional area; $B$ is the channel top width

$$h_N^{j+1} - h(t) = 0$$

Where $h_N^{j+1}$ is the stage to be computed at downstream and $h(t)$ is the stage hydrograph value input to the model.

Discharge, water level, and area of cross-section are stated at nodes of grid and $S_o$, $S_f$, $S_e$ i.e. bed slope, friction slope and energy line slope are stated at reaches.

Space derivatives of the Saint-Venant equations are:

$$\frac{\partial Q}{\partial x} = \theta \frac{Q_{i+1}^{j+1} - Q_i^{j+1}}{\Delta x_{i+1/2}} + (1 - \theta) \frac{Q_{i+1}^j - Q_i^j}{\Delta x_{i+1/2}} \tag{3}$$

$$\frac{\partial h}{\partial x} = \theta \frac{h_{i+1}^{j+1} - h_i^{j+1}}{\Delta x_{i+1/2}} + (1 - \theta) \frac{h_{i+1}^j - h_i^j}{\Delta x_{i+1/2}} \tag{4}$$

$$\frac{\partial (\frac{\beta Q^2}{A})}{\partial x} = \theta \frac{\frac{\beta Q^2}{A}_{i+1}^{j+1} - \frac{\beta Q^2}{A}_i^{j+1}}{\Delta x_{i+1/2}} + (1 - \theta) \frac{\frac{\beta Q^2}{A}_{i+1}^j - \frac{\beta Q^2}{A}_i^j}{\Delta x_{i+1/2}} \tag{5}$$

Time derivatives of the Saint-Venant equations are:

$$\frac{\partial A}{\partial t} = 0.5 \frac{A_{i+1}^{j+1} - A_{i+1}^j}{\Delta t^j} + 0.5 \frac{A_i^{j+1} - A_i^j}{\Delta t^j} \tag{6}$$

$$\frac{\partial Q}{\partial t} = 0.5 \frac{Q_{i+1}^{j+1} - Q_{i+1}^j}{\Delta t^j} + 0.5 \frac{Q_i^{j+1} - Q_i^j}{\Delta t^j} \tag{7}$$

Other factors, $A$, $Sf$, q are approximated as follows:

$$q = \theta q_{i+1/2}^{j+1} + (1 - \theta) q_{i+1/2}^j \tag{8}$$

$$Sf = Sfq_{i+1/2}^{j+1} + (1 - \theta) Sf_{i+1/2}^j \tag{9}$$

$$A = \theta A_i^{-j+1} + (1 - \theta) A_i^{-j} \tag{10}$$

Substituting all values into the continuity equation yields,

$$0.5 \frac{A_{i+1}^{j+1} - A_{i+1}^j}{\Delta t^j} + 0.5 \frac{A_i^{j+1} - A_i^j}{\Delta t^j} + \theta \frac{Q_{i+1}^{j+1} - Q_i^{j+1}}{\Delta x_{i+1/2}} + (1 - \theta) \frac{Q_{i+1}^j - Q_i^j}{\Delta x_{i+\frac{1}{2}}} - q_{i+\frac{1}{2}}^{j+1} + (1 - \theta) q_{i+\frac{1}{2}}^j = 0$$

Putting all values into the momentum equation yields,

$$0.5 \frac{Q_{i+1}^{j+1} - Q_{i+1}^j}{\Delta t^j} + 0.5 \frac{Q_i^{j+1} - Q_i^j}{\Delta t^j} + \theta \frac{\frac{\beta Q^2}{A}_{i+1}^{j+1} - \frac{\beta Q^2}{A}_i^{j+1}}{\Delta x_{i+1/2}} + (1 - \theta) \frac{\frac{\beta Q^2}{A}_{i+1}^j - \frac{\beta Q^2}{A}_i^j}{\Delta x_{i+\frac{1}{2}}} + g * (\theta A_i^{-j+1} + (1 - \theta) A_i^{-j}) \left[ \theta \frac{h_{i+1}^{j+1} - h_i^{j+1}}{\Delta x_{i+1/2}} + (1 - \theta) \frac{h_{i+1}^j - h_i^j}{\Delta x_{i+\frac{1}{2}}} + Sfq_{i+1/2}^{j+1} + (1 - \theta) Sf_{i+1/2}^j \right] = 0$$

These equations are solved by the Newton-Raphson iterative technique to calculate water level and discharge at $(j+1)^{th}$ timeline at nodes $(i)$ and $(i+1)$.

## 4. Methodology adopted

A hypothetical, rectangular river section was established, assuming a width of 800 m, an average longitudinal bed slope of 0.0005, and Manning's roughness coefficient of bed slope changing with time and distance.

The study area is strategically important, and the upper Bhima River basin catchment (45,678 km²) is one of the important tributaries of the Krishna River in the upstream part of the basin in western Maharashtra state in India. The catchment is located between 16.5°-19.5° latitude and 73.0°-76.5° longitude. The elevation ranges from 414 m in the east to 1,458 m in the western Ghat mountains; 95% of the catchment is below 800 m and relatively flat. The location of Bhima basin in Pune is shown in Figure 2.
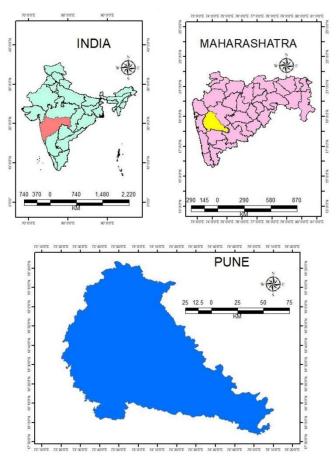


Fig. 2. Location of study area.

The Hydrologic Engineering Center's River Analysis System (HEC-RAS, V. 5.0.7) developed by the USACE is generally used for the study of flood analysis of numerous return periods. 1-D HEC-RAS hydrodynamic modeling is an applicable tool for deriving 1-D river hydraulic parameters including total discharge, water surface elevations (WSE), energy gradient elevation (EG), energy gradient slope, velocity, flow area, and Froude number at different channel sections, which help for better analysis. The applica-

tions are specifically planned for flood plain management and flood-insurance studies to estimate flood-way interruption and to reproduce estimated flood inundation in the study area. HEC-RAS demands a number of input variables for hydraulic analysis of the stream channel geometry and water flow. These parameters are used to create a series of cross-sections along the stream. In each cross-section, the locations of the stream banks are identified and used to divide the cross-section into segments of left floodway, main channel, and right floodway. At every cross-section various input parameters are used to define elevation, shape, and relative position at a river station number, including lateral and elevation coordinates for all terrain points, left and right bank locations, downstream reach lengths between the left floodplain, stream center-line, and right floodplain of every adjacent cross-section, and Manning's roughness coefficients for left, main channel, and right floodplains. Further, geometric descriptions of any hydraulic structures, such as bridges, culverts, and weirs for current study in flood modeling data for flood events of 2005 and 2017 were considered. A Bhima River stretch 67 of km with 595 cross-sections, each approximately 800 m long, was modeled. The primary data required for this modeling was collected from the Water Resource Department (WRD), Pune, Government of Maharashtra, National Hydrology Project (NHP)[1], Nasik Maharashtra, and Central Water Commission (CWC) water books. Manning's roughness coefficients were selected according to Central Water Commission (CWC) guidelines; bank stations were marked with the help of RAS-Mapper and ArcGIS world imagery. Reach length data was also collected from WRD[2] at Pune in Maharashtra. River geometry was created as shown in Figure 3.
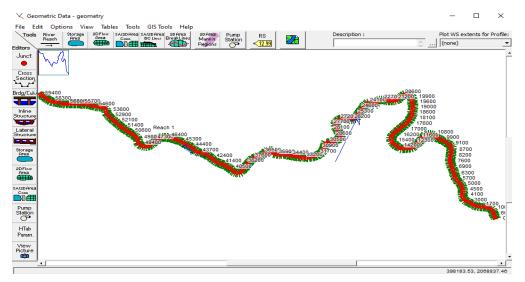


Fig. 3. Geometry of Bhima River.

Manning's coefficient reach lengths and bank stations were also used for each cross-section as shown in Figure 4. For hydrodynamic flow analysis, stage hydrographs for the period of July and August 2005 were used as downstream boundary conditions, and the flow hydrograph for the same period was used as the upstream boundary condition.

---

[1] https://www.mahahp.gov.in/HDUG
[2] https://wrd.maharashtra.gov.in

Fig. 4. Cross-section details of the Bhima River channel.

The flow data, and flow category with regime conditions are used to build up the model for the desired outcomes. The methodology followed is expressed in a flow chart (Figure 5).
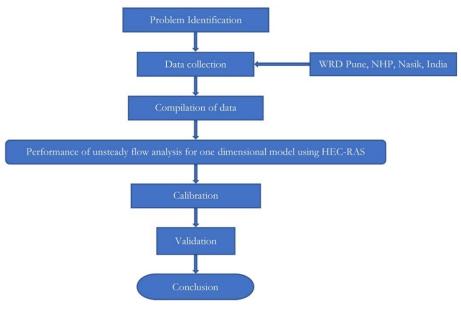


Fig. 5. Flowchart of methodology.

## 5. Data availability

Table 1 below gives the details of data types and sources of data used in this research paper on hydrodynamic flow modeling and the effect of roughness on river stage forecasting.

Table 1. Data type and source of data.

| DATA TYPE | SOURCE |
|---|---|
| Flood hydrographs | 1. National Hydrology Project (NHP), Nasik Maharashtra, India.<br>2. Central Water Commission (CWC) water books, India. |
| River Geometry data | Water Resource Department (WRD), Pune, Government of Maharashtra, India. |

## 6. Hydrodynamic model calibration

Calibration is the adjustment of a model's parameters so that it reproduces observed data to an acceptable accuracy. Roughness coefficients, i. e. Manning's roughness coefficient (n) in this case, are among the main variables used in calibrating a hydraulic model. It is known that for a free-flowing river, roughness decreases with increased stage, and flow. However, if the banks of a river are rougher than the channel bottom, then the composite value of the roughness coefficient (n) will increase with increased stage. Deposits and debris can also play an important role in the roughness. When Manning's n is increased in a particular area, then stage will increase locally, the peak discharge will decrease (attenuate) as the flood wave moves downstream, and the travel time will increase. The hydrodynamic model is calibrated using the flow hydrograph for the period of 20 July 2005 to 8 August 2005 as the upstream boundary condition and the stage hydrograph from 20 July 2005 to 8 August 2005 as the downstream boundary condition. Flow data from 2005 has been used for calibration of Manning's roughness coefficient 'n' at a time step of 24 hours. The flow and stage have been simulated using the daily hydrograph for two months from 20 July to 8 August 2005. Calibrations have been done using Manning's roughness coefficient for values ranging from 0.015 to 0.040. Subsequently, final control parameters obtained from calibration have been used for validation in the Bhima River basin. Manning's roughness coefficient (*n*)was fixed as 0.025 for the main channel, 0.03 for the left floodplain, and 0.035 for the right floodplain. The comparison of observed and simulated stage hydrograph at Phulgaon gauging station (Latitude: 18°40'01", Longitude: 74°00'08)[3], using the specified values of *n*, are shown in Figure 6.
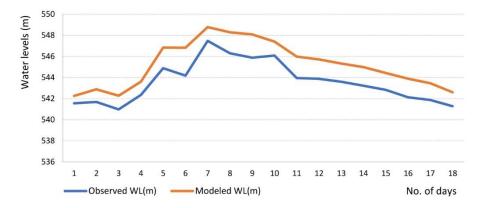
Fig. 6. Calibrated water level profiles (stages) at Phulgaon gauging station (from 20 July 2005 to 8 August 2005).

## 7. Hydrodynamic flow validation

Model validation involves testing of a model with observed field data. This data set is an independent source for channel flow, distinct from the data used to calibrate the model. The calibrated hydraulic model has been used to validate the flow for the year 2017[4]. The comparison of observed and simulated flow hydrographs at Phulgaon gauging station in the basin is shown in Figure 7.

---

[3] http://cwc.gov.in/sites
[4] http://cwc.gov.in/water-year-book

Fig. 7. Validation water level profiles (stages) at Phulgaon gauging station (from 20 July 2005 to 8 August 2005).

## 8. Model performance evaluation

Performance of the hydraulic simulation model has been evaluated using the statistical performance indicators coefficient of determination ($R^2$) (Equation 11) and root mean square error (RMSE) (Equation 12). The $R^2$ statistic describes the degree of agreement between simulated and measured water levels in the analysis. $R^2$ ranges from 0 to 1, with higher values indicating less error variance; typically values greater than 0.5 are considered acceptable in flow modeling (Legates, McCabe 1999; Moriasi et al. 2007).

$$R^2 = 1 - \frac{\text{sum of squares of errors (SSE)}}{\text{total sum of squares (SST)}}$$

$$R^2 = 1 - \frac{\sum_{i=1}^{n}(yi - \hat{y}i)^2}{\sum_{i=1}^{n}(yi - \bar{y})^2} \tag{11}$$

where $yi$ – actual/observed data at i$^{th}$ value; $\hat{y}i$ – simulated result at ith value; $n$ – total number of data; $\bar{y}$ – mean value of $n$ data.

The root-mean-square deviation (RMSD) or root-mean-square error (RMSE) is a commonly used to express the quantity of the differences between values predicted by a model and the values observed.

$$\text{RMSE} = \sqrt{\frac{\sum_{i=1}^{N}(X_i - X_i^-)}{N}} \tag{12}$$

where: i$^{th}$ variable, $N$ – number of data points; $X_i$ – observed values; $X_i^-$ – simulated values.

In calibration of the model, the coefficient of determination $R^2$ and lowest root mean square error (RMSE) were 0.9568 (Fig. 8) and 0.3099, respectively, which indicate that the simulated river stages are close to the observed stages.
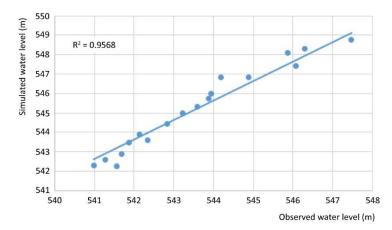
Fig. 8. Simulated river stages versus observed river stages.

## 9. Concluding remarks

This paper discusses 1-D hydrodynamic modeling developed using the Hydrologic Engineering Center's River Analysis System (HEC-RAS) and a geographical information system. The model is calibrated for the Phulgaon gauging station using the flow hydrograph during 20 July 2005 to 8 August 2005. Calibrations and validations for various values of Manning's roughness coefficient ($n$) were done, and observed and simulated water levels were compared. Values of $n = 0.025$ for the main channel, 0.03 for the left flood-plain and 0.035 for the right floodplain gave optimum results for simulated water levels. The hydrodynamic flow model validation has the highest $R^2$ and lowest RMSE. These statistics indicated that the simulated values of water levels are in close agreement with the observed value of water levels. hydrodynamic flow modelling of the Bhima River basin in India using HEC-RAS demonstrates satisfactory validity for the selected values of $n$.

References

Ahmad B., Hassan Z.A., 2011, Flood map of Tupai River using combined 1D and 2D modelling, [in:] 3rd International Conference on Managing Rivers in the 21st Century: Sustainable Solutions for Global Crisis of Flooding, Pollution and Water Scarcity, 491-496, available online at http://redac.eng.usm.my/html/publish/2011_33.pdf (data access 16.07.2021).

Hicks F., Peacock T., 2005, Suitability of HEC-RAS for flood forecasting, Canadian Water Resources Journal, 30 (2), 159-174, DOI:10.4296/cwrj3002159.

Horritt M.S., Bates P.D., 2002, Evaluation of 1D and 2D numerical models for predicting river flood inundation, Journal of Hydrology, 268 (1-4), 87-99, DOI: 10.1016/S0022-1694(02)00121-X

Khattak M.S., Anwar F, Saeed T.U., Sharif M., Sheraz K., Ahmed A., 2016, Floodplain mapping using HEC-RAS and ArcGIS: a case study of Kabul River, Arabian Journal for Science and Engineering, 41, 1375-1390, DOI: 10.1007/s13369-015-1915-3.

Kvocˇka D., Falconer R.A., Bray M., 2015, Appropriate model use for predicting elevations and inundation extent for extreme flood events, Natural Hazards, 79, 1791-1808, DOI: 10.1007/s11069-015-1926-0.

Legates D.R., McCabe Jr. G.J., 1999, Evaluating the use of "goodness-of-fit" measures in hydrologic and hydroclimatic model validation, Water Resources Research, 35 (1), 233-241, DOI: 10.1029/1998WR900018.

Moriasi D.N., Arnold J.G., Van Liew M.W., Bingner R.L., Harmel R.D., Veith T.L., 2007, Model evaluation guidelines for systematic quantification of accuracy in watershed simulation, Transactions of the ASABE, 50 (3), 885-900, DOI: 10.13031/2013.23153.

Sahoo S.N., Sreeja P., 2015, Development of flood inundation maps and quantification of flood risk in an urban catchment of Brahmaputra River, Journal of Risk and Uncertainty in Engineering Systems. Part A: Civil Engineering, 3 (1), DOI: 10.1061/AJRUA6.0000822.

Salajeghah A., Bakhshaei M., Chavoshi S., Keshtkar A.A., Najafi Hajivar M., 2009, Floodplain mapping using HEC-RAS and GIS in semi-arid regions of Iran, DESERT, 14 (1), 83-93, DOI: 10.22059/JDESERT.2010.21750.

Timbadiya P.V., Patel P.L., Porey P.D., 2012, HEC-RAS based hydrodynamic model in prediction of stages of lower Tapi River, ISH Journal of Hydraulic Engineering, 17 (2), 110-117, DOI: 10.1080/09715010.2011.10515050.

US Army Corps of Engineers, 2016, Hydrologic Engineering Requirements for Reservoirs, EM 1110-2-1420, available online at https://www.publications.usace.army.mil/Portals/76/Users/182/86/2486/EM_1110-2-1420.pdf?ver=CjRXa4pEi5SXva0UuneAZQ%3d%3d (data access 16.07.2021).

Vozinaki A.-E.K., Morianou G.G., Alexakis D.D., Tsanis I.K., 2016, Comparing 1D and combined 1D/2D hydraulic simulations using high resolution topographic data a case study of the Koiliaris basin, Greece, Hydrological Sciences Journal, 62 (4), 642-646, DOI: 10.1080/02626667.2016.1255746.

Yang J., Townsend R.D., Daneshfar B., 2006, Applying the HEC-RAS model and GIS techniques in floodplain delineation, Canadian Journal of Civil Engineering, 33, 19-28, DOI: 10.1139/l05-102.

Yerramilli S., 2012, A hybrid approach of integrating HEC-RAS and GIS towards the identification and assessment of flood risk vulnerability in the city of Jackson, MS, American Journal of Geographic Information System, 1 (1), 7-16, DOI: 10.5923/j.ajgis.20120101.02.

# Prediction of flood hydrograph using the modified Cunge-Muskingum method in an ungauged basin: a case study in the Kulsi River basin, India

Biswadeep Bharali [ID]

[1]Civil Engineering Department, Assam Engineering College, India, [2]Assam down town University, India

Utpal Kumar Misra

Civil Engineering Department, Assam Engineering College, India

Abstract

The Cunge-Muskingum routing model is one of the most popular and widely used models for hydrologic channel flood routing. The application of Cunge-Muskingum model to an ungauged basin is hindered by the lack of hydro-meteorological data. In the present study, a method is proposed to predict the outflow hydrograph of an ungauged basin as a solution to this problem. The Cunge-Muskingum method is modified, considering the non-prismatic complex natural channel. The Soil Conservation Service Curve Number rainfall-runoff model is employed to obtain the inflow and lateral inflow hydrographs of the ungauged basins, and the Modified Cunge-Muskingum model is employed to anticipate the flood hydrograph at the outlet of the ungauged basin. The proposed approach is employed to the Kulsi River Basin, India, hypothetically treated as an ungauged basin, and the results are compared with the observed data at the outlet of the basin. The performance of the model is evaluated based on RMSE (50.34 m³/s), peak flow error (39.73%), peak flow time error (–3.44%), total volume error (7.36%), relative error (7.36%), mean absolute error (33.5%), correlation coefficient (0.785), coefficient of efficiency (0.59) and Kling-Gupta efficiency (0.66).The results reveal that the proposed Modified Cunge-Muskingum model is an efficient predictor of the flood hydrograph at the outlet of the ungauged basin.

## 1. Introduction

Flood routing is a mechanism to ascertain the timing and magnitude of flow at a point on a watershed from known or assumed hydrographs at one or more points upstream (Fread 1981; Tewolde, Smithers 2006). Hydraulic structures are constructed across the rivers to prevent flood damage. To ensure ample protection from floods and to obtain viable solutions to flooding, we required flood routing. Flood routing helps in designing a proper hydraulic structure for flood control (Barati 2010). Two main approaches, one based on hydrologic routing and the other based on hydraulic routing, are typically used to guide flood waves to natural channels. The hydrological method is based on the equation of storage continuity, while the hydraulic method is based on the equations of continuity and momentum consisting of the Saint-Venant equations (Choudhury et al. 2002; Barati 2010). The outflow hydrograph at the downstream location can be estimated using a flood routing model by routing a flood event from an upstream gauging station, but in developing countries, most of the basins are ungauged.

Various simplified routing models were created in the 20th century. Most of these models have been successfully applied to rivers and reservoirs (Hashmi 1993). Due to the adequacy and reliable relationship

between their parameters and channel properties, the Muskingum method (McCarthy 1938) and the Muskingum-Cunge method (Cunge 1969) are widely adopted and used in flood routing models (Fread 1983; Haktanir, Ozmen 1997). The Muskingum model investigates a method of parameter estimation to determine the weight coefficient $X$ and wave travel time $K$. Yoo et al. (2017) proposed a methodology to determine the Muskingum parameters, using the basin characteristics which represents the inlet and outlet of the channel reach. Most of the methods are optimization techniques, including trial and error, recession analysis (Yoon, Padmanabhan 1993), least-squares (Al-Humoud, Esen 2006), feasible sequential quadratic programming (Kshirsagar et al. 1995), chance-constrained optimization (Das 2004, 2007), genetic algorithm (Chen, Yang 2007), particle swarm optimization (Chu, Chang 2009), harmony search (Kim et al. 2001), Broyden-Fletcher-Goldfarb-Shanno technique (Geem 2006), immune clonal selection algorithm (Luo, Xie 2010), and hybrid algorithm (Lu et al. 2007; Yang, Li 2008). However, because they need large amounts of observed data, these studies and methods are more applicable to flood routing in gauged basins.

It is difficult to predict flow characteristics in ungauged basins (Sivapalan et al. 2003), because streamflow time series are usually not long enough for parameter calibration. Two common ways to address this problem are: (a) the use of physically-based models, and (b) regionalization of model parameters according to the physical characteristics of basins (Yadav et al. 2007). To improve the prediction accuracy of streamflow in an ungauged basin, several regionalization models have been developed, including parametric regression, the nearest neighbor method, and the method of hydrological similarity (Li et al. 2010). Physically-based models are strongly linked to the basin's observed physical characteristics. Many physically based distributed hydrological models have been created and used in ungauged basins to simulate and predict runoff hydrographs. However, differences in scale, over-parameterization, and model structural error remain impediments, and some calibration criteria are generally required. Bharali and Misra (2020a-b, 2021) proposed hydraulic routing methods to estimate the flood hydrograph at the outlet of the ungauged basin. For flood routing models used in ungauged basins, the relationships between physical characteristics and model parameters of gauged basins are useful (Tewolde, Smithers 2006). Consequently, the modification and interpretation of the Muskingum model's parameters in terms of physical properties extends the model's applicability to ungauged basins, as observed by Kundzewicz and Strupczewski (1982).

The Muskingum method is one of the most popular and commonly used hydrologic methods for flood routing. McCarthy introduced it in 1938 for management of the Muskingum River basin in Ohio by the Army Corps of Engineers (Chow 1959; Henderson 1966; Roberson et al. 1988; Li et al. 2019). The original formulation of the method was strictly empirical, with two coefficients that worked together to control translation and attenuation. Initially, it was recognized that one of the coefficients, often referred to as $X$, was associated with the weight factor, which had the most significant impact on attenuation, whereas the second coefficient, often referred to as $K$, was related to the time of travel or the translation

of the wave through the channel. The $X$ coefficient was limited to the range 0 to 0.5, and to estimate it from calibration data, graphical techniques were developed (Roberson et al. 1988; Fenton 2019).

Long-term discharge observations are usually not available at the appropriate location, and, for various reasons, these records often contain missing data. As a result, many hydrological models have been developed to obtain runoff from rainfall due to the easy availability of rainfall data for longer periods at various locations (Singh, McCann 1980; Singh, Frevert 2005). The Soil Conservation Service Curve Number (SCS-CN) model has been widely used to calculate surface runoff. A theoretical framework for validating the SCS method has been provided (Yu 1998). Yu (2012) showed that the proportionality in the SCS equation would follow retention and runoff if the temporal distribution of rainfall intensity and spatial distribution of the highest infiltration rate were independent and illustrated by an exponential probability distribution. In particular, 'Yu' demonstrated that the highest retention $S$ could be seen as the product of the highest average infiltration rate and effective rainfall duration. Changes were made to the original SCS-CN method by replacing $(P-I_a)$ with $0.5*(P-I_a)$ (Mishra, Singh 1999). They made comparisons between the current SCS-CN system and the proposed modification, and the new version was found to be more reliable than the existing version. The flood prediction was carried out using the curve number method in the geographical information system (GIS) at the North Karun River field (Akhondi 2001).

The current SCS-CN method was modified and named the MS model by Mishra et al. (2004); the proposed model was based on the SCS-CN method and also incorporated the antecedent moisture while calculating the direct surface runoff. The modified version was evaluated and compared with the existing SCS-CN method, with the observation that the modified MS model's performance was much better than the existing SCS-CN model. In 2005, by considering a large set of rainfall-run-off events, they used the MS model with its eight variants in the field and revealed that the performance of the current version of the SCS-CN method was remarkably poor compared to all model variants. To increase the applicability of the model for complex watersheds with high temporal and spatial variability of soil and land use, some researchers have incorporated the SCS-CN model into the GIS/RS system (Zhan, Huang 2004; Geetha et al. 2007). Many researchers have used the GIS technique to determine curve numbers and quantities of runoff in different world regions. Using the SCS-CN based unit hydrograph method, Reshma et al. (2010) proposed a hydrological model to simulate runoff from the sub-watershed. They also developed another hydrological model using the Muskingum-Cunge technique to route the runoff from sub-watersheds to the outlet of watersheds. Few mechanisms are used to estimate the spatial differences in hydrological parameters, namely remote sensing and GIS techniques, and it has been found that the developed model has correctly simulated runoff hydrographs at the outlet of the watershed. Zlatanovic and Gavric (2013) computed the morphometric properties for each catchment, first using the topographical map manually, and then automatically using pre-processed DEM based on SRTM data and scripting capabilities of GIS. The conversion of excess rainfall into direct runoff was triggered using a modified SCS dimensionless unit

hydrograph, and the flow rates obtained by the automated method proved to be slightly higher than that obtained manually.

Xiao et al. (2011) studied the applicability of the SCS-CN model to a small watershed with high spatial variability on the Loess Plateau, China. By using the inverse method, they scaled the most suitable $I_a/S$ values. A modification was made to the value of $I_a/S$ to ensure that the model yielded the best performance; this ratio was traditionally set at 0.2. This value of the initial abstraction ratio was eventually assumed for the runoff estimate. They found that when $I_a/S$ was between 0.15 and 0.30, the relative error was almost constant, but when it was less than 0.15, the relative error rapidly decreased with the increase in $I_a/S$. Gupta et al. (2012) changed the SCS-CN method to correct it for steep slopes to overcome the slope limitations of the SCS-CN method. Antecedent moisture has been included using the Mishra. et al. (2005) approach. There should also be two essential components in a hydrological model of runoff modeling, namely, runoff generation and runoff routing. The SCS-CN is a static model and does not take account of the runoff routing phase. Gupta et al. (2012) used a hybrid technique that combined a modified version of SCS-CN with a physically distributed two-dimensional (2D) overland flow model to extend SCS-CN to account for the runoff routing stage.

Soulis and Valiantzas (2012) proposed two CN systems by considering a theoretical analysis of SCS-CN. Based on a systematic investigation using synthetic data, and a detailed case study, they conclude that the correlation between the calculated CN values and the depth of rainfall in a watershed can be attributed to the watershed's land cover and soil's spatial variability. Therefore, the two proposed CN systems can adequately describe the changes in CN rainfall observed in natural watersheds. Assumptions of proportionality of the SCS method have been examined to validate the foundation of the method (Yu 2012). It was found that the product of effective storm duration and maximum infiltration rate is a good predictor of maximum retention parameters in SCS. This interpretation provides an effective method for determining the extent of storm runoff, which predicts runoff volume and peak runoff. In order to quantitatively study and forecast the runoff outcome caused by precipitation, Panahi (2013) performed a scientific evaluation analysis and proposed a model for estimating runoff and obtaining potential sites of study area runoff production using experimental methods. For precision and effectiveness, an experimental version of SCS-CN was used. The potential of the region's runoff production was determined through the preparation of the CN.

In the present study, the Cunge-Muskingum method is modified, considering both temporal and spatial variation, to predict the outflow hydrograph at the outlet of an ungauged basin. In the modified Cunge-Muskingum method, lateral inflows are considered. The inflow and the lateral inflows are obtained using the SCS-CN rainfall-runoff model. The proposed Modified Cunge-Muskingum method is employed in the Kulsi River Basin, northeast India, and the results obtained are compared with the observed data.

## 2. Study area and database

## 2.1. Study area

In this study, the Kulsi River Basin, a part of the Brahmaputra sub-basin, was selected and was treated as a hypothetically ungauged basin. A total area of 2822.99 km² drains through the Kulsi River Basin, covering the Kamrup District of Assam, the Western Khasi Hills, and the Ri Bhoi district of Meghalaya in northeast India. Because of its strategic location (encompassing two states in northeast India) and the fact that the region experiences large floods, the basin is an ideal target for flood routing. The study area is situated on the south bank of the mighty Brahmaputra River. It is located at latitudes 25°30'N to 26°10'N and longitudes 89°50'E to 91°50'E (Fig. 1).
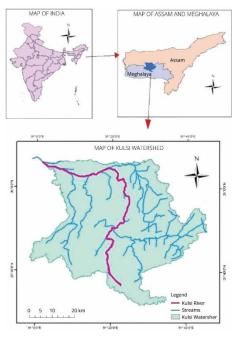


Fig. 1. Location of Kulsi River Watershed.

## 2.2. Data

Daily rainfall data for 2010 were collected from the Indian Metrological Department (IMD), Guwahati. Daily discharge data for 2010 at the basin outlet were collected from the National Institute of Hydrology, Guwahati. Digital elevation models (DEM) are being widely used for watershed delineation, extraction of stream networks, and characterization of watershed topography (elevation map, slope map, and aspect map) by using a watershed delineation tool in ArcGIS software. The DEM used in this project was collected from CartoSat 1_V3_R1. CartoDEM version_3R1 is a national DEM developed by the Indian Space Research Organization (ISRO) with the accuracy of 3.6-4 m (RMSE). CartoDEM version_3R1 has resolution of 30.87 m × 30.87 m (or 1 arc sec). For the delineation of the Kulsi River Watershed, the GeotiffCartoDEMs are ng46g, ng46h, ng46m, and ng46n. In this study, soil data were obtained from the Harmonized World Soil Database v 1.2 of the Food and Agriculture Organization (FAO) soil portal. The Kulsi River Watershed soil texture consists of clay loam, loam, and sandy loam. The study area's soils are categorized into four hydrological classifications (A, B, C, and D) depending on the infiltration rate and other traits. The important soil features affecting the hydrological classification of soils are effective depth

of soil, average clay content, infiltration rate, and the soil's absorbing capacity. Group A is low runoff potential, Group B is moderately low runoff potential, Group C is moderately high runoff potential, and Group D is high runoff potential.

## 2.3. Land Use and Land Cover (LULC)

The LULC for the Kulsi River Watershed was developed by Maximum Likelihood Supervised Image Classification as per the required class sample using ArcGIS 10.1 software. A Linear Imaging Self Scanning Sensor (LISS)-III Satellite image is used in this project to perform supervised image classification. The LISS-III image operates in three spectral bands in Visible and Near Infrared (VNIR) and one band in Short Wave Infrared (SWIR) with 23.5 m spatial resolution and a swath of 141 km. The LISS-III image was downloaded from Bhuvan.

## 2.4. Sub-Basins of Kulsi River Basin

Eight lateral inflows have been identified as contributing to the mainstem Kulsi River. Sub-basins for lateral inflows are delineated using ArcGIS 10.1, and the details of each sub-basin are presented in Table 1.

## 2.5. Rainfall data distribution

Rainfall distribution over the study area was estimated by the interpolation method using ArcGIS software. Inverse Distance Weighted (IDW), Kriging, and Spline are the three general methods available in Arc GIS 10.1 for interpolation. In this study, the IDW method was used for rainfall interpolation as IDW is the best for the point data format.

The field rainfall data is collected from seven numbered rain gauge stations around the Kulsi Watershed. In 2010, the month of June experienced a maximum amount of rainfall. For this study, daily rainfall for the month of June 2010 is distributed over the study area using IDW using ArcGIS 10.1. The minimum and maximum daily rainfall data for the month of June are presented in Figure 2.
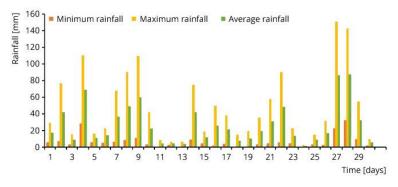


Fig. 2. Rainfall Data over Kulsi River Watershed.

## 3. Methodology

## 3.1. SCS-CN method

In this study, SCS-CN is used as a rainfall-runoff model to obtain an inflow hydrograph upstream of the

ungauged basin. This method is a simple, predictable, and stable conceptual technique for estimating direct runoff depth based on storm precipitation depth. It relies on only one parameter, the Curve Number (CN). Currently, it is a well-established method, having been widely accepted for use in India and many other countries.

The SCS-CN method is based on the water balance equation and two fundamental hypotheses. The first hypothesis is that the ratio of the amount of direct surface runoff $Q$ to the total precipitation $P$ (or maximum potential surface runoff) is equal to the ratio of the amount of infiltration $F_c$ to the amount of the maximum potential retention $S$. The second hypothesis is that the initial abstraction $I_a$ is some fraction of the maximum potential retention '$S$' (Subramanya 2008).

Water balance equation:

$$P = I_a + F_c + Q \tag{1}$$

Proportional equality hypothesis:

$$\frac{Q}{(P-I_a)} = \frac{F_c}{S} \tag{2}$$

$I_a$ is some fraction of the potential maximum retention ($S$):

$$I_a = \lambda S \tag{3}$$

where: $P$ is the total precipitation; $I_a$ the initial abstraction; $F_c$ the cumulative infiltration excluding $I_a$; $Q$ the direct surface runoff; $S$ the potential maximum retention or infiltration, and $\lambda$ the regional parameter dependent on geological and climatic factors $(0.1 < \lambda < 0.3)$.

Solving Equation (2):

$$Q = \frac{(P - I_a)^2}{P - I_a + S} \text{ if } P > I_a, \text{ otherwise } Q = 0 \tag{4}$$

$$Q = \frac{(P - \lambda S)^2}{P - (\lambda - 1) S} \tag{5}$$

By analyzing the rainfall and runoff data from small experimental watersheds, the relationship between $I_a$ and $S$ was established and expressed as $I_a = 0.2S$. Combining the water balance equation and proportional equality hypothesis; the SCS-CN method is represented as:

$$Q = \frac{(P - 0.2S)^2}{P + 0.8S} \tag{6}$$

A Curve Number (CN), which is a function of land use, land treatments, soil type, and antecedent

moisture condition of the watershed, is correlated with the potential maximum retention storage $S$ of the watershed. The Curve Number is dimensionless and ranges from 0 to 100 in magnitude. Using equation (7), the $S$-value can be obtained from CN in mm.

$$S = \frac{25400}{CN} - 254 \tag{7}$$

### 3.1.1. Curve Number (CN)

The hydrological classification is adopted in the determination of CN. Based on the infiltration and other characteristics, soils are classified into classes A, B, C, and D in order of increasing runoff potential. Effective soil depth, average clay content, infiltration characteristics, and permeability are the important soil characteristics which influence the hydrological classification of soils. In this study, the variation of curve number for various land conditions and for different hydrological classification is obtained from Chow et al. (1988).

### 3.2. Modified Cunge-Muskingum method

Cunge (1969) proposed the Cunge-Muskingum method based on the Muskingum method, a method traditionally applied to linear hydrologic storage routing. Referring to the time-space computational grid shown in Figure 3, the Muskingum routing equation is modified and written as equation (8), for the discharge at $x = (i + 1)\Delta x$ and $t = (j + 1)\Delta t$:

$$Q_{i+1}^{j+1} = C_0 Q_i^{j+1} + C_1 Q_i^j + C_2 Q_{i+1}^j \tag{8}$$

Where $C_0$, $C_1$, and $C_2$ are the routing coefficients.

$$C_0 = (\Delta t + 2KX)/m \tag{9}$$

$$C_1 = (\Delta t - 2KX)/m \tag{10}$$

$$C_2 = [2K(1 - X) - \Delta t]/m \tag{11}$$

where $m = [2K(1 - X) + \Delta t]$ \tag{12}

$$\frac{\partial Q}{\partial x} = \frac{Q_{i+1}^{j+1} - Q_i^{j+1}}{\Delta x}$$

$$\frac{\partial Q}{\partial t} = \frac{Q_{i+1}^{j+1} - Q_{i+1}^{j}}{\Delta t}$$

$$Q = \frac{Q_i^{j+1} + Q_{i+1}^{j}}{2}$$
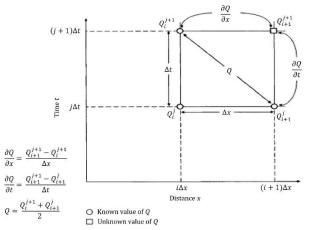
○ Known value of $Q$
□ Unknown value of $Q$

Fig. 3. Time-Space computational grid for the proposed model.

In equation (9) through (11), $K$ is a storage constant having dimensions of time and $X$ is a factor expressing the relative influence of inflow on storage levels. Equation 8 gives an approximate solution of a modified diffusion equation:

$$K = \frac{\Delta x}{c_k} = \frac{\Delta x}{dQ/dA} \tag{13}$$

$$X = \frac{1}{2} 1 - \left(\frac{Q}{Bc_k S_0 \Delta x}\right) \tag{14}$$

Where $c_k$ is the celerity of wave corresponding to $Q$ and $B$, and $B$ is the top width of the surface water. Cunge (1969) showed that for numerical stability, it is required that $0 \leq X \leq 1/2$. Figure 4 shows the procedure for the modified Cunge-Muskingum method adopted in the present study.
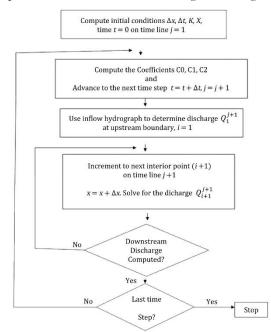


Fig. 4. Flowchart for the Modified Cunge-Muskingum method.

## 4. Results and discussion

## 4.1. SCS-CN Rainfall-Runoff Model in the Kulsi River Basin

Flood routing is a process to determine the outflow hydrograph at a point on a watercourse from the known inflow hydrograph at the upstream gauged station. The flood routing process is difficult in ungauged basins due to a lack of data. In this study, the SCS-CN model is used to obtain the inflow hydrograph at the upstream section (Ukiam Dam Site). Similarly, the lateral inflows of the eight sub-basins contributing to the Kulsi River are also obtained by SCS-CN. The runoff discharge hydrograph for each sub-basin is presented in Figure 5. The figure shows that the peak runoff discharge for each sub-basin occurred on 28 June, 2010. Sub-basin C shows a maximum peak discharge of 95.35 m³/s, whereas sub-basin H shows a minimum peak discharge of 4.31 m³/s. It is also observed that all the lateral inflow hydrographs follow the same trend.
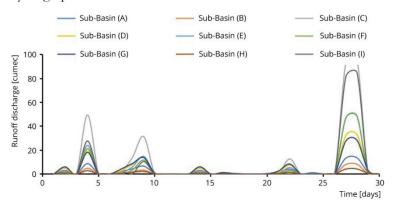


Fig. 5. Inflow hydrographs of Kulsi River Sub-basins.

## 4.2. Criteria for evaluation of model performance

The following criteria were used to evaluate the performance of the model:

1). In order to compare the proposed model output to the data observed, the criteria for making such a comparison must first be identified (Green, Stephenson 1985). In the present study, the difference between the observed and the computed hydrograph was analyzed by root-mean-square error (RMSE). The RMSE evaluates the magnitude of the error in the computed hydrographs (O'Donnell 1985; Schulze et al. 1995) and is given by:

$$RMSE = \sqrt{\frac{\sum_{i=1}^{n}(Q_{comp} - Q_{obs})^2}{n}}, \text{i} = 1, 2, 3, ..., n \tag{15}$$

In this equation, $Q_{comp}$ represents the computed outflow, and $Q_{obs}$ represents the observed outflow.

2). The criterion for the difference between computed and observed peak discharge ($E_{peak}$) (Green, Stephenson 1985) is given by:

$$E_{peak} = \frac{Q_{p,comp} - Q_{p,obs}}{Q_{p,obs}} \cdot 100 \tag{16}$$

The above equation shows the percentage of error in the peak discharge. In the present study, the peak flood discharge at the outlet of the basin obtained from the computed flood hydrograph was compared with the observed flood hydrograph. In equation 16, $Q_{p,comp}$ is the computed peak flows in m³/s, and $Q_{p,obs}$ is the observed peak flows in m³/s.

3). The criterion for the difference between computed and observed peak discharge time ($E_{time}$) is given by:

$$E_{time} = \frac{t_{p,comp} - t_{p,obs}}{t_{p,obs}} \cdot 100 \tag{17}$$

The above equation shows the percentage of error in peak discharge time. In the present study, the peak flow time for the computed and observed flood hydrograph was compared. In the above-mentioned equation, $t_{p,comp}$ is the time taken by the computed hydrograph to reach the peak flow in hours, and $Q_{p,obs}$ is the time taken by the observed hydrograph to reach the peak flow in hours.

4). The criterion for the difference between the computed and observed total volume ($E_{volume}$) is given by:

$$E_{volume} = \frac{V_{comp} - V_{obs}}{V_{obs}} \cdot 100 \tag{18}$$

The above equation shows the percentage of error in the total volume of the computed hydrograph. In the present study, the total volume was compared for computed and observed flood hydrographs. In the above-mentioned equation, $V_{comp}$ is the total volume of the computed hydrograph in m³ and $V_{obs}$ is the total volume of the observed hydrograph in m³.

5). Relative error ($RE$) is given by:

$$RE = \frac{|Q_o - Q_p|}{Q_o} \cdot 100\% \tag{19}$$

The above equation shows the relative error in percentage. In the above-mentioned equation, $Q_o$ is the observed data at the time $t$ and $Q_p$ is the predicted value at the time $t$. The relative error is used to determine the percentage of samples belonging to one of the three groups (Corzo, Solomatine 2007):

- $RE \leq 15\%$        low relative error
- $15\% < RE \leq 35\%$    medium error
- $RE > 35\%$         high error

6). Mean absolute error ($MAE$) (Cheng et al. 2017) is given by:

$$MAE = \frac{1}{n} \sum_{i=1}^{n} |Q_o - Q_p| \tag{20}$$

In the above-mentioned equation $n$ is the number of samples, $Q_o$ is the observed data at the time $t$, and $Q_p$ is the predicted value at the time $t$.

7). Correlation coefficient ($r$) is given by:

$$r = \frac{\sum_{i=1}^{n}(Q_o - Q_m)(Q_p - Q_{mp})}{\sqrt{\sum_{i=1}^{n}(Q_o - Q_m)^2}\sqrt{\sum_{i=1}^{n}(Q_p - Q_{mp})^2}} \tag{21}$$

In the above-mentioned equation $n$ is the number of samples, $Q_o$ is the observed discharge at the time $t$, $Q_p$ is the predicted discharge at the time $t$, $Q_{mp}$ is the mean of predicted discharge, and $Q_m$ is the mean of observed discharge.

8). Coefficient of efficiency (CE) (Nash, Sutcliffe 1970) is given by:

$$CE = 1 - \left[\frac{\sum_{i=1}^{n}(Q_o - Q_p)^2}{\sum_{i=1}^{n}(Q_o - Q_m)^2}\right] \tag{22}$$

In the above-mentioned equation $n$ is the number of samples, $Q_o$ is the observed data at the time $t$ and $Q_p$ is the predicted value at the time $t$, and $Q_m$ is the mean of observed discharge. Moriasi et al. (2007) recommended the following model performance ratings:

- $CE \leq 0.50$         unsatisfactory
- $0.50 < CE \leq 0.65$    satisfactory
- $0.65 < CE \leq 0.75$    good
- $0.75 < CE \leq 1$       very good

9). Kling-Gupta efficiency (*KGE*).

Gupta et al. (2009) developed this goodness-of-fit measure to provide a diagnostically interesting decomposition of the efficiency of Nash-Sutcliffe efficiency, which facilitates the analysis of the relative importance of its various components. In the context of the hydrological modelling Kling et al. (2012), proposed a revised version of this index to ensure that the bias and variability ratios are not cross-correlated.

$$KGE = 1 - \left[\sqrt{(CC - 1)^2 + (\frac{cd}{rd} - 1)^2 + (\frac{cm}{rm} - 1)^2}\right] \tag{23}$$

where: *CC* is the Pearson correlation coefficient; *rm* is the average of observed values; *cm* is the average of predicted values; *rd* is the standard deviation of observation values; and *cd* is the standard deviation of predicted values. Rogelis et al. (2016) consider model performance to be 'poor' for $0.5 > KGE > 0$. Schönfelder et al. (2017) consider negative *KGE* values as 'not satisfactory.'

## 4.3. Application of the Modified Cunge-Muskingum method in the Kulsi River Basin

The method was coded in MATLAB software and the Cunge-Muskingum parameters $K$ and $X$ were determined. The computed outflow hydrograph using the proposed model and the observed data

(hydrograph) collected from the National Institute of Hydrology (NIH), Guwahati, are presented in Figure 6. From the figure, it can be seen that the shape of the computed outflow hydrograph is very much similar to that of the observed data at the outlet of the Kulsi River Basin.

The quantitative comparison of the proposed model with the observed data is presented in Table 2. From the table, the computed peak outflow was on the 28th day, 24 hr prior to the observed peak outflow. The computed peak outflow discharge was greater than the observed outflow discharge. The computed peak discharge was 370.53 m³/s, whereas the observed peak discharge was 265.17 m³/s. The performance of the model is evaluated by nine different criteria, with results presented in Table 2.
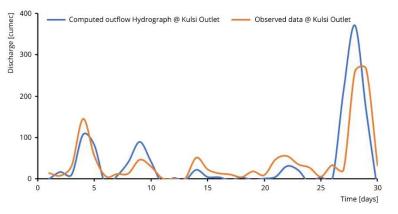


Fig. 6. Comparison graph of the observed outflow and the calculated outflow at the Kulsi River outlet for the Cunge-Muskingum method.

Table 1. Details of the sub-basins of the study area.

| Parameters | Sub-Basin I | Sub-Basin H | Sub-Basin G | Sub-Basin F | Sub-Basin E | Sub-Basin D | Sub-Basin C | Sub-Basin B | Sub-Basin A |
|---|---|---|---|---|---|---|---|---|---|
| Area [km²] | 1180.3 | 8.97 | 63.15 | 385.57 | 274.25 | 101.24 | 485.67 | 26.77 | 30.43 |
| Agricultural area [km²] | 6.63 | 8.63 | 49.03 | 37.33 | 43.3 | 13.01 | 112 | 3.34 | 1.16 |
| Open space area [km²] | 0.12 | 0.07 | 0.83 | 14.26 | 10.36 | 2.36 | 56.79 | 0.05 | 0.73 |
| Open forest area [km²] | 93.7 | -- | 0.52 | 34.88 | 42.11 | 18.81 | 48.70 | 7.21 | 3.08 |
| Dense forest area [km²] | 1076.78 | -- | 0.006 | 272 | 135.72 | 49.48 | 200.92 | 14.19 | 24.62 |
| Residential area [km²] | 3.12 | 0.25 | 12.76 | 27.1 | 42.76 | 17.57 | 67.21 | 1.97 | 0.81 |
| Hydrological Classification | A, D | B | B | A, B, D | A, B, D | B, D | A, B, D | B, D | D |
| Curve Number (CN) | 52.3 | 80.6 | 78.8 | 57.9 | 62.1 | 72.5 | 63.8 | 71.8 | 78.5 |

## 4.4. Sensitivity analyses

The significance of sensitivity studies in modelling is generally acknowledged. Sensitivity analyses allow for the evaluation of the consequences of input errors, and the sensitivity of model parameters relative to other parameters allows for an understanding of the significance of the corresponding inputs (Akbari, Barati 2012).

The Kulsi River Basin was selected to test the sensitivity of the input variables on the output of the proposed model. For this purpose, the upstream hydrograph must be developed for the upstream

boundary condition. Figure 7 shows the upstream hydrograph generated in this study using SCS-CN. The sensitivity of the proposed model was determined by varying individual input parameters such as river length, roughness coefficient, bed slope, inflow peak discharge, channel width, and then evaluating the effects on outflow peak discharge, time to peak, velocity, depth corresponding to peak discharge, and volume of the hydrograph.
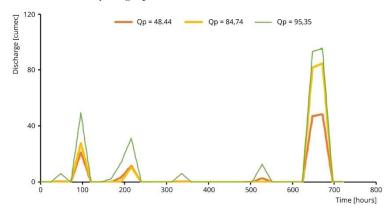


Fig. 7. Upstream hydrographs for Kulsi River used in sensitivity analysis.

Sensitivity analysis requires basic values for the parameters, which are then adjusted within a given range; the model variance is evaluated for each set of parameter values. Table 3 shows the range of parameter variations based on the features of the Kulsi River and the uncertainty of the model's input parameters. The Sensitivity Index $SI$ (percent) is used for a comprehensive analysis of the impact of changing input parameters on output outcomes in an ungauged basin.

$$SI = \frac{(O_2-O_1)/(O_2+O_1)}{(I_2-I_1)/(I_2+I_1)} \cdot 100, \text{ (Akbari, Barati 2012)} \tag{24}$$

Where $I_1$ and $I_2$ are the smallest and largest values of input parameters, and $O_1$ and $O_2$ are output values corresponding to $I_1$ and $I_2$, respectively. $SI$ is used to compare parameter sensitivities. A negative $SI$ indicates an inverse relationship between input and output parameters (i.e., the output value of the model decreases as the input value increases) (Akbari, Barati 2012). The results of the performance of varied input parameters are presented in Table.4. The $SI$ values for the proposed model were evaluated based on changing one input parameter and evaluating the effect on the selected output result (Table 5). The effects of variations in river length $L$, roughness n, and bed slope $S_0$ on the output hydrographs are illustrated in Figures 8 to 10, respectively. The figures indicate that river length is the most influential parameter with regard to the shape of the output hydrograph.

Table 2. Comparison of the performance of the proposed model with the observed data at the outlet of the Kulsi River Basin.

| Evaluation Criteria | Units | Modified Cunge Muskingum method | Remarks |
|---|---|---|---|

| | | | |
|---|---|---|---|
| Root Mean Square Error (*RMSE*) | m³/s | 50.34 | -- |
| Peak Flow Error (*E_peak*) | % | 39.73 | -- |
| Peak Flow Time Error (*E_time*) | % | -3.44 | -- |
| Total Volume Error (*E_volume*) | % | 7.36 | -- |
| Relative Error (*RE*) | % | 33.5 | Medium error |
| Mean Absolute Error (*MAE*) | -- | 31.57 | -- |
| Correlation coefficient (*r*) | -- | 0.785 | -- |
| Coefficient of efficiency (*CE*) | -- | 0.59 | Satisfactory |
| Kling-Gupta efficiency (*KGE*) | -- | 0.66 | Not poor |

Table 3. Values of parameters for sensitivity analysis of the Modified Cunge-Muskingum method.

| Parameters | Peak flow [m³/s] | Length [km] | Roughness [S/m.^(1/3)] | Bed Slope [m/km] |
|---|---|---|---|---|
| Lower bound | 48.44 | 5 | 0.03 | 2 |
| Base Value | 84.74 | 15 | 0.035 | 3 |
| Upper bound | 95.35 | 30 | 0.04 | 5 |

Table 4. Performance of the different input parameters.

| Parameter | Bound | Time to Peak [h] | Peak Outflow [m³/s] | Velocity [m/s] | Depth [m] | Volume [cubic meter] |
|---|---|---|---|---|---|---|
| Roughness Coefficient | Lower | 672 | 76.02 | 0.22 | 5.10 | 1765.90 |
| | Base | 672 | 75.47 | 0.20 | 5.66 | 1684.20 |
| | Upper | 672 | 75.17 | 0.18 | 6.21 | 1608.90 |
| Bed Slope | Lower | 672 | 76.42 | 0.24 | 4.75 | 1811.10 |
| | Base | 672 | 76.66 | 0.25 | 4.58 | 1816.40 |
| | Upper | 671 | 77.60 | 0.29 | 3.98 | 1825.10 |
| Peak flow | Lower | 672 | 42.13 | 0.14 | 4.46 | 1012.70 |
| | Base | 672 | 76.02 | 0.19 | 5.08 | 1765.90 |
| | Upper | 672 | 88.09 | 0.22 | 5.78 | 2937.30 |
| River Length | Lower | 671 | 79.18 | 0.23 | 5.17 | 1992.30 |
| | Base | 672 | 76.02 | 0.22 | 5.09 | 1989.90 |
| | Upper | 673 | 70.68 | 0.22 | 5.07 | 1980.90 |

Table 5. Values of sensitivity index [%].

| | Peak Inflow | Roughness Coefficient | Bed Slope | River Length |
|---|---|---|---|---|
| Peak outflow | 108.18 | –3.94 | 1.78 | –7.94 |
| Time of Peak | 0.00 | 0.00 | –0.17 | 0.21 |
| Volume | 149.35 | –32.56 | 0.90 | –0.40 |
| Depth | 39.54 | 68.70 | –20.77 | –1.34 |
| Velocity | 71.76 | –73.36 | 22.56 | –1.86 |

Table 6. Sensitivity rankings of the inputs to the MDWMP: P, peak inflow; n, roughness coefficient; L, river length; S, bed slope.

| Order of importance | Peak outflow | Time to peak | Volume | Depth | Velocity | All parameters |
|---|---|---|---|---|---|---|

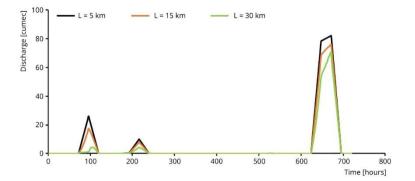| 1 | P | L | P | n | n | P |
|---|---|---|---|---|---|---|
| 2 | L | n | n | P | P | n |
| 3 | n | -- | S | S | S | S |
| 4 | S | -- | L | L | L | L |



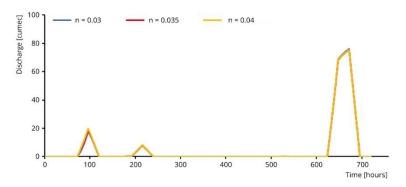Fig. 8. Effect of variation in river length on outflow hydrograph.



Fig. 9. Effect of variation of roughness on outflow hydrograph.
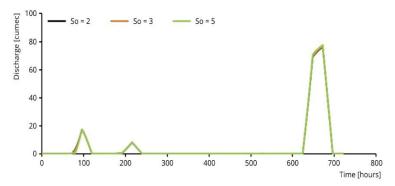


Fig. 10. Effect of variation of bed slope on outflow hydrograph.

### 4.4.1. Discussion of results

Sensitivity index

Based on the Modified Cunge-Muskingum method sensitivity assessments, this section highlights the relevant input parameters for each of the output outcomes. Table 6 shows the result of the parameter importance rankings.

According to the *SI* findings for peak outflow, the following parameters are ranked in order of importance: peak inflow, river length, roughness coefficient, and bed slope. Although the *SI* of the peak outflow is modest for bed slope, it is substantial for the other parameters. According to the sensitivity index, the peak discharge has an inverse connection with the roughness coefficient and river length.

The *SI* results for the period of peak show that river length and bed slope are the most important parameters. For peak inflow and roughness coefficient, however, the *SI* of the peak time is insignificant. In contrast to the bed slope, the river length has a direct relationship with the time of the peak. The *SI* results show that peak input, roughness coefficient, bed slope, and river length are the most important parameters for flood volume. In contrast to the roughness coefficient and river length, the peak inflow and bed slope have a direct connection with volume. The *SI* results show that the roughness coefficient, peak inflow, bed slope, and river length are the most important parameters for the depth corresponding to the peak discharge. The peak inflow and roughness coefficient, unlike the other parameters, have a direct connection with depth. The *SI* findings for the velocity corresponding to the peak discharge show that the following parameters are ranked in order of importance: roughness coefficient, peak inflow, bed slope, and river length. Peak inflow and bed slope were shown to have a direct connection with velocity, but roughness coefficient and river length had an inverse association with velocity.

If all output parameters are considered at the same time, the rankings of parameters important for the absolute *SI* mean are peak inflow (73.76%), roughness coefficient (35.71%), bed slope (9.24%), and river length (2.34%). The strongest effects of the input parameter related to flood characteristics (i.e., peak inflow) are on the volume of the floods and peak outflow, and the strongest effects of the input parameter related to bed surface (i.e., bed slope) are on the velocity and depth, according to the analysis of the *SI* values. The peak outflow, velocity, and depth are the most affected by the input parameters relating to river geometry (i.e. river length).

Effect of grid size

Numerical tests are used to examine the impacts of grid size (i.e., space and time steps) on the output results in terms of the dimensionless peak discharge. The impacts of changing time and spatial steps on the proposed model's performance were explored in these experiments. This method was carried out using the inflow hydrograph at the Kulsi River's entrance. Figures 11 and 12 show variations in the peak of the outflow hydrograph ordinate $Q_{po}$, which was dimensionless, and the peak of the inflow hydrograph ordinate $Q_{pi}$ with variations in space and time steps.
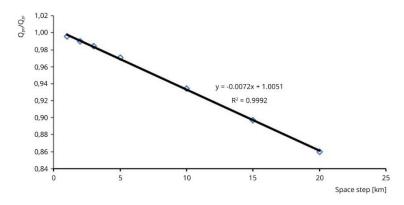
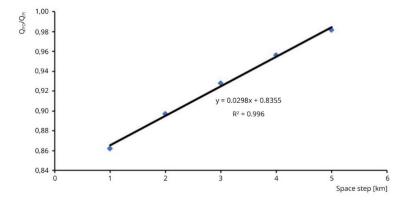Fig. 11. Effect of variation in space step on dimensionless peak discharge.



Fig. 12. Effect of variation in time step on dimensionless peak discharge.

Both the space step and the time step with the peak discharge were found to have a linear connection with a high correlation coefficient. Based on the numerical data, it can be said that differences in time step have only a little influence on peak discharge and have no effect on time to peak. The effects of changes in the space step on the peak discharge are more substantial than the impacts of variations in the time step.

## 5. Conclusion

In the present study, the inflow hydrograph and lateral inflow hydrographs of the Kulsi River Basin are obtained using the SCS-CN rainfall-runoff model. The modified Cunge-Muskingum model is employed to anticipate the outflow hydrograph at the outlet of the Kulsi River Basin. One of the advantages of the proposed approach is that the outflow hydrograph is obtained through a linear algebraic equation instead of a finite difference scheme or characteristic approximation. This allows the entire hydrograph to be obtained at the required cross-section, whereas in the other models, requiring a solution over the entire length of the channel for each time step. The modified Cunge-Muskingum method allows more flexibility to choose time and space increments for the computations. The results obtained by using the proposed model shows good agreement between the computed and observed outflow hydrograph at the outlet of the Kulsi River Basin. The performance of the model is also assessed considering nine statistical parameters namely *RMSE* (50.34 m³/s), peak flow error (39.73%), peak flow time error (–3.44%), total volume error (7.36%), relative error (7.36%), mean absolute error (33.5%), correlation coefficient (0.785),

Coefficient of efficiency (0.59) and Kling-Gupta efficiency (0.66). Based on the performance of the proposed model, it is concluded that the model can be efficiently used to predict the outflow hydrograph in an ungauged basin. A sensitivity analysis of the proposed model was performed to understand the reliability of the computed outputs in order to make effective decisions when developing a model to simulate the natural process. This study demonstrated that in the selection of input parameters, parameters with a high sensitivity index (*SI*) must be identified. The impact of grid size on output outcomes has also been studied. The results demonstrate that differences in space step have a greater influence on peak discharge than variations in time step. Some of the improvements which can be incorporated in the proposed model are summarized below.

1). In the present study an established mathematical equation is used for estimating the Muskingum Coefficient. Linear programming, genetic algorithms, fuzzy inference system, radial basis function, and other advanced neurocomputing techniques can be explored to improve the performance of the proposed model.
2). The present study employed rainfall of June 2010. More rainfall events may be analyzed as and when sufficient data become available to make the forecasting more robust and reliable.
3). The proposed model can be improved by using the modified SCS-CN method as a rainfall-runoff model.

**Declarations**

Funding: Not applicable.

Conflicts of interest: On behalf of all authors, the corresponding author states that there is no conflict of interest.

Availability of data and material: Data that support the findings of the study will be available from the corresponding author upon reasonable request.

Code availability: Codes that support the findings of the study will be available from the corresponding author upon reasonable request.

Author Contributions: All authors contributed to the study conception and design. Material preparation, data collection and analysis were performed by [Biswadeep Bharali]. The first draft of the manuscript was written by [Biswadeep Bharali] and all [Dr. Utpal Kr. Misra] commented on previous versions of the manuscript and supervised the work. All authors read and approved the final manuscript.

**Acknowledgement**

The authors are thankful to the Civil Engineering Department, Assam Engineering College, Guwahati, Assam.

References

Akbari G.H., Barati R., 2012, Comprehensive analysis of flooding in unmanaged catchments, Proceedings of the Institution of Civil Engineers: Water Management, 165 (4), 229-238, DOI: 10.1680/wama.10.00036.

Akhondi E., 2001, Analyzing curve number model in estimating flood by using geographical information systems, MA dissertation, The Faculty of Natural Resources and Maritime Sciences, Tarbiat-e-Modarres University.

Al-Humoud J.M., Esen I.I, 2006, Approximate methods for the estimation of the Muskingum flood routing parameters, Water Resources Management, 20 (6), 979-990, DOI: 10.1007/s11269-006-9018-2.

Barati R., 2010, Investigation of flood routing methods in natural waterways, (in Persian), Master's Thesis, The University of Sistan and Baluchestan Graduate School.

Bharali B., Misra U.K, 2020a, Development of a diffusive wave food routing model for an ungauged basin: a case study in Kulsi River Basin, India, Modeling Earth Systems and Environment, 7, 1053-1069, DOI: 10.1007/s40808-020-00952-1.

Bharali B., Misra U.K., 2020b, Investigation of flood routing using Variable Parameter Kinematic Wave Model (VPKWM) for non-prismatic natural channel in an ungauged basin, Journal of Applied Engineering Sciences, 10 (23), 111-118, DOI: 10.2478/jaes-2020-0017.

Bharali B., Misra U.K., 2021, An approach for prediction of flood hydrograph at outlet of an ungauged basin using modified dynamic wave model, ISH Journal of Hydraulic Engineering, DOI: 10.1080/09715010.2021.1901250.

Chen J.J., Yang X.H., 2007, Optimal parameter estimation for Muskingum model based on Gray-encoded accelerating genetic algorithm, Communications in Nonlinear Science and Numerical Simulation, 12 (5), 849-858 DOI: 10.1016/j.cnsns.2005.06.005.

Cheng K.-S., Lien Y.-T., Wu Y.-C., 2017, On the criteria of model performance evaluation for real-time flood forecasting, Stochastic Environmental Research and Risk Assessment, 31, 1123-1146, DOI: 10.1007/s00477-016-1322-7.

Choudhury P., Shrivastava R.K., Narulkar S.M., 2002, Flood routing in river networks using equivalent Muskingum inflowm Journal of Hydrologic Engineering, 7 (6), 413-419, DOI: 10.1061/(ASCE)1084-0699 (2002)7:6(413).

Chow V.T., 1959, Open channel hydraulics, McGraw-Hill, 680 pp.

Chow V.T., Maidment D.R., Mays L.W., 1988, Applied hydrology, McGraw-Hill Book Company, 572 pp.

Chu H.-J., Chang L.-C., 2009, Applying particle swarm optimization to parameter estimation of the nonlinear Muskingum model, Journal of Hydrologic Engineering, 14 (9), 1024-1027, DOI: 10.1061/(ASCE)HE.1943-5584.0000070.

Corzo G., Solomatine D., 2007, Baseflow separation techniques for modular artificial neural network modelling in flow forecasting, Hydrological Sciences Journal, 52 (3), 491-507, DOI: 10.1623/hysj.52.3.491.

Cunge J.A., 1969. On the subject of a flood propagation computational method (Muskingum method), Journal of Hydraulic Research, 7 (2), 205-230, DOI: 10.1080/00221686909500264.

Das A., 2004, Parameter estimation for Muskingum models, Journal of Irrigation and Drainage Engineering, 130 (2), 140-147, DOI: 10.1061/(ASCE)0733-9437(2004)130:2(140).

Das A., 2007, Chance-constrained optimization-based parameter estimation for Muskingum models, Journal of Irrigation and Drainage Engineering, 133 (5), DOI: 10.1061/(ASCE)0733-9437(2007)133:5(487).

Fenton D.J., 2019, Flood routing methods, Journal of Hydrology, 570, 251-261, DOI: 10.1016/j.jhydrol.2019.01.006.

Fread D.L., 1981, Flood routing: a synopsis of past, present, and future capability, [in:] Rainfall-runoff relationship, Proceedings of the International Symposium on Rainfall-runoff Modelling, V.P. Singh (ed.), Mississippi State University, U.S.A.

Fread D.L., 1983, A "Unified" Coefficient Routing Model, available at https://www.nws.noaa.gov/ohd/hrl/hsmb/docs/hydraulics/papers_before_2009/hl_173.pdf (data access 21.10.2021).

Geem Z.W., 2006, Parameter estimation for the nonlinear Muskingum model using the BFGS technique, Journal of Irrigation and Drainage Engineering, 132 (5), 474-478, DOI: 10.1061/(ASCE)0733-9437(2006)132:5(474).

Geetha K., Mishra S.K., Eldho T.I., Rastogi A.K., Pandey R.P., 2007, Modifications to SCS-CN method for long-term hydrologic simulation, Journal of Irrigation and Drainage Engineering, 133 (5), 475-486, DOI: 10.1061/(ASCE)0733-9437(2007)133:5(475).

Green I., Stephenson D., 1985, Comparison of urban drainage models for use in South Africa, WRC Report No 115/6/86, Water Research Commission, Pretoria, RSA.

Gupta H.V., Kling H., Yilmaz K.K., Martinez G.F., 2009, Decomposition of the mean squared error and NSE performance criteria: Implications for improving hydrological modelling, *Journal of Hydrology*, *377* (1-2), 80-91, DOI: 10.1016/j.jhydrol.2009.08.003.

Gupta P.K., Punalekar S., Panigrahy S., Sonakia A., Parihar J.S., 2012, Runoff modeling in an agro-forested watershed using remote sensing and GIS, Journal of Hydrologic Engineering, 17 (11), 1255-1267, DOI: 10.1061/(ASCE)HE.1943-5584.0000466.

Haktanir T., Ozmen H., 1997, Comparison of hydraulic and hydrologic routing on three long reservoirs, Journal of Hydraulic Engineering, 123 (2), 153-156, DOI: 10.1061/(ASCE)0733-9429(1997)123:2(153).

Hashmi D., 1993, Flow routing model for Upper Indus River (Pakistan), Ph.D. Dissertation, The University of British Columbia.

Henderson F.M., 1966, Open channel flow, Prentice Hall, New Jersey, 522 pp.

Kim J.H., Geem Z.W., Kim E.S., 2001, Parameter estimation of the nonlinear Muskingum model using harmony search, Journal of the American Water Resources Association, 37 (5), 1131-1138, DOI: 10.1111/j.1752-1688.2001.tb03627.x.

Kling H., Fuchs M., Paulin M., 2012. Runoff conditions in the upper Danube basin under an ensemble of climate change scenarios, Journal of Hydrology, 424-425, 264-277, DOI: 10.1016/j.jhydrol.2012.01.011.

Kshirsagar M.M., Rajagopalan B., Lal U., 1995, Optimal parameter estimation for Muskingum routing with ungauged lateral inflow, Journal of Hydrology, 169 (1-4), 25-35, DOI: 10.1016/0022-1694(94)02670-7.

Kundzewicz Z.W., Strupczewski W.G., 1982, Approximate translation in the Muskingum model, Hydrological Sciences Journal, 27 (1), 19-27, DOI: 10.1080/02626668209491082.

Li M., Shao Q., Zhang L., Chiew F.H.S., 2010, A new regionalization approach and its application to predict flow duration curve in ungauged basins, Journal of Hydrology, 389 (1), 137-145, DOI: 10.1016/j.jhydrol. 2010.05.039.

Li W., Lin K., Zhao T., Lan T., Chen X., Du H., Chen H., 2019, Risk assessment and sensitivity analysis of flash floods in ungauged basins using coupled hydrologic and hydrodynamic models, Journal of Hydrology, 572, 108-120, DOI: 10.1016/j.jhydrol.2019.03.002.

Lu F., Jiang Y.Z., Wang H., Niu C.W., 2007, Application of multi-agent genetic algorithm to parameter estimation of Muskingum model, Journal of Hydraulic Engineering, 39 (3), 289-294.

Luo J.G., Xie J.C., 2010, Parameter estimation for nonlinear Muskingum model based on immune clonal selection algorithm, Journal of Hydrologic Engineering, 15 (10), 844-851, DOI: 10.1061/(ASCE)HE.1943-5584.0000244.

McCarthy G.T., 1938, The unit hydrograph and flood routing, Conference of North Atlantic Division, US Army Corps of Engineers, New London, CT.

Mishra S.K., Geetha K., Rastogi A.K., Pandey R.P., 2005, Long-term hydrologic simulation using storage and source area concepts, Hydrological Processes, 19 (14), 2845-2861, DOI 10.1002/hyp.5735.

Mishra S.K., Jain M.K., Singh V.P., 2004, Evaluation of the SCS-CN-based model incorporating antecedent moisture, Water Resources Management, 18, 567-589, DOI: 10.1007/s11269-004-8765-1.

Mishra S.K., Singh V.P., 1999, Another look at SCS-CN method, Journal of Hydrologic Engineering, 4 (3), 257-264, DOI: 10.1061/(ASCE)1084-0699(1999)4:3(257).

Moriasi D.N., Arnold J.G., Liew M.W.V., Bingner R.L., Harmel R.D., Veith T.L., 2007, Model evaluation guidelines for systematic quantification of accuracy in watershed simulations, Transactions of the American Society of Agricultural and Biological Engineers, 50 (3), 885-900, DOI: 10.13031/2013.23153.

Nash J.E., Sutcliffe J.V., 1970, River flow forecasting through conceptual models. Part I. A discussion of principles, Journal of Hydrology 10 (3), 282-290, DOI: 10.1016/0022-1694(70)90255-6.

O'Donnell T., 1985, A direct three-parameter Muskingum procedure incorporating lateral inflow, Hydrologic Science Journal, 30 (4), DOI: 10.1080/02626668509491013.

Panahi A., 2013, Evaluating SCS-CN Method in Estimating the Amount of Runoff in Soofi Chay basin Using GIS, Life Science Journal, 10 (5s), 271-277.

Reshma T., Kumar P.S., Babu M.J.R.K., Kumar K.S., 2010, Simulation of runoff in watersheds using SCS-CN AND Muskingum-Cunge methods using remote sensing and geographical information systems, International Journal of Advanced Science and Technology, 25, 31-42.

Roberson J.A., Cassidy J.J., Chaudhry M.H., 1988, Hydraulic engineering, Houghton Mifflin Company, Boston, 662 pp.

Rogelis M.C., Werner M., Obregón N., Wright N., 2016, Hydrological model assessment for flood early warning in a tropical high mountain basin, Hydrology and Earth System Sciences. Discussions, DOI: 10.5194/hess-2016-30.

Schönfelder L.H., Bakken T.H., Alfredsen K., Adera A.G., 2017, Application of HYPE in Norway, SINTEF Energy Research Report, available at http://hdl.handle.net/11250/2499427 (data access 21.10.2021).

Schulze R., 1995, Hydrology and agrohydrology: a text to accompany the ACRU 3.00 agrohydrological modelling system, [in:] WRC Report No TT 69/95, Water Research Commission, Pretoria, RSA.

Singh V.P., Frevert D.K. (eds.), 2005, Watershed models, CRC Press, Boca Raton, 687 pp.

Singh V.P., McCann R.C., 1980, Some notes on Muskingum method of flood routing, Journal of Hydrology, 48 (3-4), 343-361, DOI: 10.1016/0022-1694(80)90125-0.

Sivapalan M., Takeuchi K., Franks S.W., Gupta V.K., Karambiri H., Lakshmi V., Liang X., McDonnell J.J., Mendiondo E.M., O'Connell P.E., 2003. IAHS decade on predictions in ungauged basins (PUB), 2003-2012: Shaping an exciting future for the hydrological sciences, Hydrological Sciences Journal, 48 (6), 857-880, DOI: 10.1623/hysj.48.6.857.51421.

Soulis K.X., Valiantzas J.D., 2012, SCS-CN parameter determination using rainfall-runoff data in heterogeneous watersheds – the two-CN system approach, Hydrology and Earth System Sciences, 16 (3), 1001-1015, DOI: 10.5194/hess-16-1001-2012.

Tewolde M.H., Smithers J.C., 2006, Flood routing in ungauged catchments using Muskingum methods, Water SA, 32 (3), 379-388, DOI: 10.4314/wsa.v32i3.5263.

Xiao B., Wang Q.-H., Fan J., Han F.-P., Dai Q.-H., 2011, Application of the SCS-CN model to runoff estimation in a small watershed with high spatial heterogeneity, Pedosphere, 21 (6), 738-749, DOI: 10.1016/S1002-0160(11)60177-X.

Yadav M., Wagener T., Gupta H., 2007, Regionalization of constraints on expected watershed response behaviour for improved predictions in ungauged basins, Advances in Water Resources, 30 (8), 1756-1774, DOI: 10.1016/j.advwatres.2007.01.005.

Yang X.H., Li J.Q., 2008, Chaos high efficient genetic algorithm for parameter optimization of Muskingum routing model, Journal of Hydrologic Engineering, 27 (2), 40-44.

Yoo C., Lee J., Lee M., 2017, Parameter estimation of the Muskingum channel Flood-Routing model in ungauged channel reaches, Journal of Hydrologic Engineering, 22 (7), DOI: 10.1061/(ASCE)HE.1943-5584.0001507.

Yoon J., Padmanabhan G., 1993, Parameter estimation of linear and nonlinear Muskingum models, Journal of Water Resources Planning and Management, 119 (5), 600-610, DOI: 10.1061/(ASCE)0733-9496(1993)119:5(600).

Yu B., 1998, Theoretical justification of SCS method for runoff estimation, Journal of Irrigation and Drainage Engineering, 124 (6), 234-238, DOI: 10.1061/(ASCE)0733-9437(1998)124:6(306).

Yu B., 2012, Validation of SCS method for runoff estimation, Journal of Hydrologic Engineering, 17 (11), 1158-1163, DOI: 10.1061/(ASCE)HE.1943-5584.0000484.

Zhan X., Huang M.L., 2004, ArcCN-Runoff: an ArcGIS tool for generating curve number and runoff maps, Environmental Modelling and Software, 19 (10), 875-879, DOI: 10.1016/j.envsoft.2004.03.001.

Zlatanović N., Gavrić S., 2013, Comparison of an automated and manual method for calculating storm runoff response in ungauged catchments in Serbia, Journal of Hydrology and Hydromechanics, 61 (3), 195-201, DOI: 10.2478/johh-2013-0025.

# Air temperature in high-altitude areas as exemplified by the Tatra Mountains

Krzysztof Jurczak [ID]

Institute of Meteorology and Water Management – National Research Institute, Poland

Stanisław Kędzia [ID]

Institute of Geography and Spatial Organization, Polish Academy of Sciences

Abstract

The climate of a high-altitude postglacial cirque, such as Kozia Dolinka, is conducive to the occurrence of permafrost. Both the depth of permafrost and the area it covers, as well as the presence of year-round snow patches, can serve as indicators for assessing the impact of global warming on the climate of mountains, including the Tatras. With few meteorological stations to survey the remote and inaccessible high-altitude areas of the Tatra Mountains, any research must rely on measurements spanning limited time periods. Against this background, the 5-year series of temperature measurements from the Kozia Dolinka cirque obtained by the Institute of Geography and Spatial Organization of the Polish Academy of Sciences (IGiPZ PAN) can be used to analyze air temperature patterns on concave and convex terrain forms in the alpine climate zone if compared to the results of measurements from stations of the State Hydrological and Meteorological Service located nearby, i.e. the Kasprowy Wierch High-Mountain Meteorological Observatory and the Hala Gąsienicowa Nival Research Station of the Institute of Meteorology and Water Management, National Research Institute (IMGW-PIB). This study confirms that there is a relationship between air temperature and the formation and duration of snow cover on concave and convex terrain forms. It also reveals a hitherto unknown fact that concave terrain forms, i.e. postglacial cirques, of the alpine zone have milder thermal conditions in winter than convex terrain forms. The analyses highlight the need for further, more detailed research using modern automated meteorological stations.

## 1. Introduction

The last Tatra glaciers were small glaciers situated in, and often hanging, postglacial cirques at high altitudes (Fig. 1, 3) and melted at the end of the Venediger period, i.e. about 8.3 ka BP (Baumgart-Kotarba, Kotarba 2001a-b). Currently, these cirques only contain glacierets and perennial or seasonal snow patches (e.g. Gadomski 1926; Wdowiak 1959, 1961a-b; Kondracki 1978; Jania 1988; Wiślińscy 1991, 1993; Kędzia 1993; Gądek 2002). In some of them, e.g. the Kozia Dolinka cirque, the presence of permafrost has been found (e.g. Kędzia et al. 1998; Mościcki, Kędzia 2001; Kędzia 2004). Glacierets and perennial snow patches are mainly supplied by avalanches and the transportation of snow from rock faces by the wind. Altitude and shading also play a role in contributing to permafrost. Although research on perennial snow patches has been conducted for at least 70 years (Milata 1949) and that on permafrost for about 25 years (Dobiński 1996a-c), measurements of air temperature in high-altitude cirques are rare. A short series of air temperature measurements were recorded in the Kozia Dolinka valley in the 1960s by Hess and his students (Kłapa 1963). In the following years, research into the microclimate, this time of the Mięguszowiecki Kocioł cirque, was conducted by geographers from the University of Warsaw Scientific Society (Gutry-Korycka 1967; Wdowiak 1961a-b), followed by Lublin geographers under the leadership of

Wiśliński (Wiślińscy 1991). However, there are no known publications by these authors which compare the temperature of postglacial cirques with convex forms located at similar altitudes (e.g. Kasprowy Wierch High-Mountain Meteorological Observatory). Only Hess (1965) found that large-scale concave forms, such as intramontane basins, have a lower average annual temperature (by about 1°C) than convex forms at a similar altitude. When investigating the climatic conditions of patches of permanent snow in 1991, Kędzia (1993) completed two several-day series of measurements of air temperature in the Kocioł Mięguszowiecki cirque and compared them with data from the Kasprowy Wierch High-Mountain Meteorological Observatory. He found that in the absence of clouds in the morning, when direct radiation reached the bottom of the cirque, the air temperature in the cirque was higher than that recorded on Kasprowy Wierch. The Kocioł Mięguszowiecki cirque was also warmer than Kasprowy Wierch at times of persistence of high or complete cloud cover and moderate or strong wind. In the remaining times of the day, air temperature in the cirque in question was lower than that on Kasprowy Wierch. The air temperature in the Kocioł Mięguszowiecki cirque was also strongly influenced by three patches of firn ice (Kędzia 1993). In 2011, Gądek initiated air temperature measurements in the Kocioł Mięguszowiecki cirque (oral information in 2019), but no study of these measurements has been released to date. In 2004, Mościcki (2010a-b) began measuring air temperatures in the Kozia Dolinka and Świnicki Kocioł cirques. Unfortunately, owing to the non-standard measurement method employed (at a height of below 2 m), it cannot be compared with other measurements, which are typically taken at 2 m above the ground.



Fig. 1. Tatra Mountains in Europe.

The climate of a high-altitude postglacial cirque, such as Kozia Dolinka, is also conducive to the formation and retention of permafrost (Li et al. 2016; Wang et al. 2018). Both the depth of such permafrost and the area it covers, as well as the presence of year-round snow patches, can serve as indicators for assessing the impact of global warming on the climate of the mountains, including the Tatras (IPCC 2001, 2007, 2013, 2014, 2019).

Despite an array of publications focusing on the various forms of ground relief and the processes present in high-altitude postglacial Tatra cirques (Dąbrowska 2015), their microclimate has not yet been properly investigated. The short series of measurements that exist are insufficient for accurate determination of the average annual air temperature and for a detailed comparison of postglacial cirques with convex forms

(ridges, peaks), as represented by the Kasprowy Wierch High-Mountain Meteorological Observatory, a benchmark station for the High Tatras. Previous attempts to characterize the microclimate of high-altitude postglacial cirques have amounted to estimates – rather than actual determinations – of average annual air temperatures on the basis of a set of measurements restricted by major terrain-related difficulties. When covered by snow, the Kocioł Mięguszowiecki cirque is not only frequented by avalanches from above, but – due to its low slope angle – also accumulates large amounts of snow that spills in avalanches moving further downslope. The constant slow movement of the snow cover down the slope further complicates obtaining measurements, especially in spring. Even masts made of thick aluminum pipes with a diameter of c. 5 cm are bent and knocked down. Additionally, the bottoms of the postglacial cirques and the lower sections of slopes tend to accumulate a deep snow cover up to several meters thick (e.g. approx. 6 m in the Kozia Dolinka valley). As a result of such substantial accumulations of snow, for several winter months sensors measure the temperature of the snow, opposed to that of the air, and regular maintenance of the sensors in wintertime is practically impossible. Comparing temperatures supplied by automatic stations installed within postglacial cirques, with data from the Kasprowy Wierch High-Mountain Meteorological Observatory (Fig. 2), must be preceded by quality control, otherwise it may can lead to erroneous conclusions. The reason may be limitations in the possibility of supervising the conditions of exposure of instruments and the frequency of service activities in an unguarded place (postglacial cirque) and in a meteorological station with specialist staff.



Fig. 2. IMGW-PIB Kasprowy Wierch High-Mountain Meteorological Observatory: a) meteorological instruments in winter setting, b) meteorological instruments in summer setting, c) observatory building (source IMGW-PIB).

In this paper, air temperatures of the Kozia Dolinka cirque measured in 2004-2008 are compared to those from the Kasprowy Wierch High-Mountain Meteorological Observatory. Although the series of measurements from the Kozia Dolinka cirque has numerous gaps in the warm period of the year, it is the only

such long series of data from a small Tatra postglacial cirque that has been studied to date. The purpose of this paper is to more accurately define the microclimate of small high-altitude postglacial cirques, and to compare it with the microclimate of convex landforms, namely peaks. The paper also attempts to determine to what extent standard air temperature measurements reflect the actual variability of the microclimate in this type of high-mountain area.

## 2. Study area

A postglacial cirque approximately 500 m and 100 m wide in the Sucha Woda Valley, namely Kozia Dolinka, whose bottom lies at an altitude of 1930-1950 m (Fig. 3), was selected as the study area. The cirque opens towards the north-east, and the peaks that surround it reach c. 2300 m. The rocky slopes and walls are incised by deep gullies with large, but poorly fragmented talus cones formed at their mouths (Fig. 4). The snow cover, both on the bottom and in the lower sections of the slope, is several meters thick, and only disappears in the first half of June.

In the depressions, firn patches persist until July, and occasionally until August. Very small patches of firn ice may persist in gully mouths and at the interface between rock faces and screes until September. Permafrost occurs in the talus cones under Kozi Wierch and Kozie Czuby (Kędzia et al. 1998; Mościcki, Kędzia 2001; Kędzia 2004).

Finding the right spot to install the station posed a huge problem. The most interesting place for measuring air temperatures is the lower area of the scree near Kozi Wierch, where the permafrost is the thickest. This area is only exposed to direct solar radiation for roughly half of the year. However, given the proximity of the tourist trail, great thickness of the snow cover and likelihood of snow avalanches, the idea of positioning the station there was abandoned. After observing the formation of the snow cover in Kozia Dolinka for several years it was concluded that the only spot where the station would last and measure air, rather than snow temperature was a rocky outcrop between the upper sections of the talus cones beneath the Kozi Wierch and the Kozie Czuby peaks. The outcrop lies at about 2010 m a.s.l. and around 60 m above the bottom of the adjacent valley. Kędzia installed an air temperature measuring station here in 2014. Even though the area has no permafrost and its location, at 60 m above the bottom of the cirque, implies that it is not the coldest spot during temperature inversion period, the area nevertheless reflects the thermal conditions of the concave landform, and is suitable for studying differences in thermal conditions with the neighboring peaks and ridges. This includes the conditions that prevail at the Kasprowy Wierch High-Mountain Meteorological Observatory.

The results of temperature measurements from Kozia Dolinka were compared with the measurements of the Kasprowy Wierch High-Mountain Meteorological Observatory, which lies at an altitude of 1991 m, c. 20 m below the Kozia Dolinka station, but at the top of a peak (a convex form). The temperature is measured in a meteorological cage mounted on the roof of the building (Fig. 2).
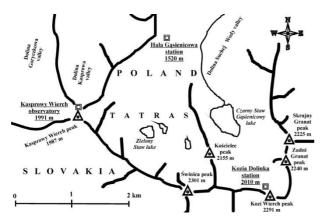
Fig. 3. Study area (ridge map): Kozia Dolinka – Kasprowy Wierch – Hala Gąsienicowa.



Fig. 4. Kozia Dolinka station.

## 3. Research methods

Air temperatures in the Kozia Dolinka valley were measured at a height of 2 m above the ground, using Onset Computers digital HOBO Pro data loggers, fitted with thermistors with a measurement uncertainty of ±0.2°C and resolution of 0.02°C (Fig. 4). Before they were installed onsite, each logger had been calibrated to an accuracy of 0.1°C, and checked after it was removed from the measuring site. The measurements spanned the period from 14 October 2004 to 29 January 2009. Measurements were logged daily on an hourly basis. The thermistor (digital thermometer) was placed in a radiation shield, which protected it against precipitation and direct solar radiation. The maximum thickness of the snow cover at the measuring site (in the years 2004-2009) usually remained below 1 m as a result of snow being blown away by the wind. Despite the relatively low snow cover in spring (twice in June and once in May), the mast of the station would be knocked down and destroyed by the dense snow that moved downslope. As a consequence, there are gaps in the data series in each year.

Temperatures at the IMGW-PIB Kasprowy Wierch High-Mountain Meteorological Observatory were measured by Vaisala temperature sensors integrated into an automatic MAWS 301 weather station. The sensors were placed in a meteorological cage mounted on the roof of the building 2 m above its surface (Fig. 2). They had valid calibration certificates and were additionally checked using portable calibration standards at six-month intervals. The measurement results were recorded in one-minute steps. This paper

uses the data recorded at each full hour. The sensor's exposure was checked on an ongoing basis and adjusted throughout the day, if necessary, by observers in the observatory.

The data on snow cover duration were based on the measurements at the Hala Gąsienicowa Nival Research Station of the IMGW-PIB. Unlike the Kasprowy Wierch High-Mountain Meteorological Observatory, the Hala Gąsienicowa Station is free of disturbances to the thickness of the snow cover resulting from the transportation of snow by winds. The Hala Gąsienicowa Station, which has the status of a second-order synoptic station (from 1 January 2019, previously a third-order climate station) is the highest situated IMGW-PIB station in the Tatras (1520 m a.s.l.), and the snow cover is measured in a meteorological garden.

## 4. Results

Despite the gaps in the data series, mainly in the summer, there is clear seasonality in the average monthly temperatures between Kozia Dolinka and Kasprowy Wierch (Figs. 5, 6). In late autumn, winter and early Spring (Fig. 5) Kozia Dolinka is generally warmer. The difference in the average monthly air temperature between these two sites increases with the number of days with snow cover and decreases as the snow cover recedes. The greatest difference in average monthly temperatures was recorded in March 2006, when Kozia Dolinka was warmer than Kasprowy Wierch by 0.8°C. The situation reversed in September (from June to August, the station was damaged after heavy snowfall in late May and the first decade of June). At that time the snow cover had already melted on the ridges and peaks, while the shaded slopes in Kozia Dolinka were still snow-covered, the Kozia Dolinka cirque was 0.2°C colder. It was the coldest in April 2007, when the difference in the average monthly temperatures between Kozia Dolinka and Kasprowy Wierch reached 0.6°C. This was associated with very early thawing of the winter snow cover across the Tatras, where snow could only be found in high lying and shaded concave landforms. A similar situation occurred in June-August 2008, when the temperature difference reached 0.5°C. The least pronounced differences in temperature between the stations in question were recorded in autumn 2005. This was likely driven by snowfall in August and the following months, as well as the early formation of snow cover throughout the Tatras. This eliminated temperature differences arising from the influences of active surfaces, which normally behave in different ways in autumn (especially in connection with the presence of snow patches in concave forms and the absence thereof on convex ones).
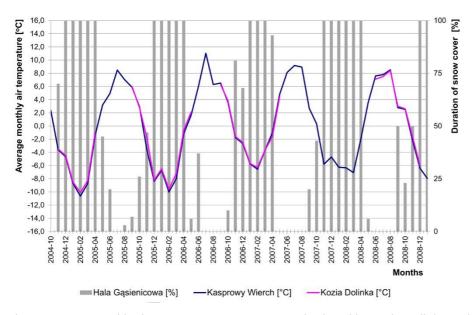
Fig. 5. Average monthly air temperature on Kasprowy Wierch and in Kozia Dolinka, and duration of snow cover on Hala Gąsienicowa.
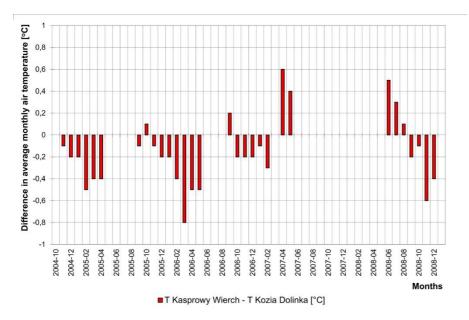


Fig. 6. Difference in average monthly air temperature between Kasprowy Wierch and Kozia Dolinka. Negative values occur when the temperature in Kozia Dolinka is higher than on Kasprowy Wierch.

While the most pronounced differences between Kozia Dolinka and Kasprowy Wierch in the average monthly air temperature were mainly recorded in the second half of the winter (February-March), the largest differences in the average monthly minimum temperature were chiefly observed in autumn and in the first part of winter (October-November). The most noticeable differences in the average monthly minimum temperature in the study period were recorded in autumn 2005 and winter 2006 (Figs. 7, 8). In absolute terms, the largest difference and duration of snow cover on Hala Gąsienicowa was recorded in November 2005, when the average monthly minimum temperature in the Kozia Dolinka cirque was higher

and amounted to –4.7°C, while that on Kasprowy Wierch was –5.6°C. By contrast, the smallest differences in the average monthly minimum temperature were recorded in the winter of 2004. Lower values of the average monthly minimum temperature in Kozia Dolinka were chiefly recorded in winter and spring. The difference did not exceed 0.3°C.
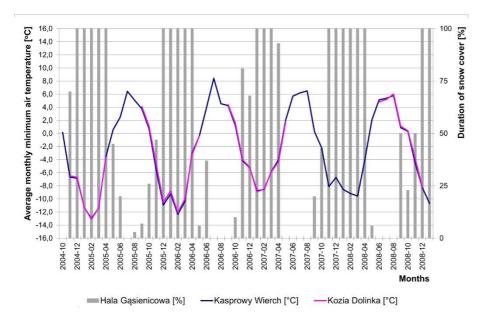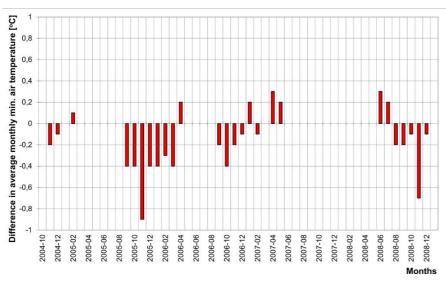


Fig. 7. Average monthly minimum air temperature on Kasprowy Wierch and in Kozia Dolinka, and duration of snow cover on Hala Gąsienicowa.



Fig. 8. Difference in average monthly minimum air temperature between Kasprowy Wierch and Kozia Dolinka. Negative values occur when the temperature in Kozia Dolinka is higher than on Kasprowy Wierch.

However, the largest differences between Kozia Dolinka and Kasprowy Wierch were observed for the average monthly maximum temperature (Figs. 9, 10). In April 2006, the average monthly maximum temperature in Kozia Dolinka was 3.1°C higher than on Kasprowy Wierch, while the year before, i.e. in April

2005, this was 2.5°C. In the winter of 2007, the greatest differences reached 0.6°C. Large differences between the stations were also observed in September 2006 and 2008, when the average monthly maximum temperatures in the Kozia Dolinka cirque were 1.1°C and 0.7°C higher, respectively. Values of average monthly maximum temperature which were lower than on Kasprowy Wierch occurred twice in the warm season (in September and October 2005 and in June-August 2008), and once in winter (April 2007). The difference in recorded values fluctuated around 0.5°C.
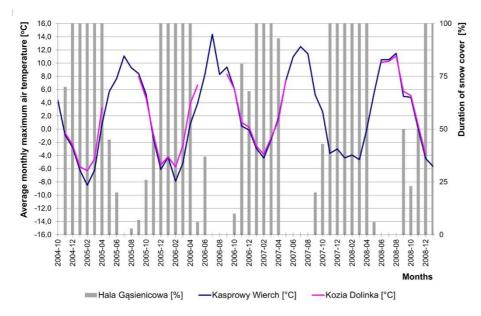


Fig. 9. Average monthly maximum air temperature on Kasprowy Wierch and in Kozia Dolinka, and duration of snow cover on Hala Gąsienicowa.
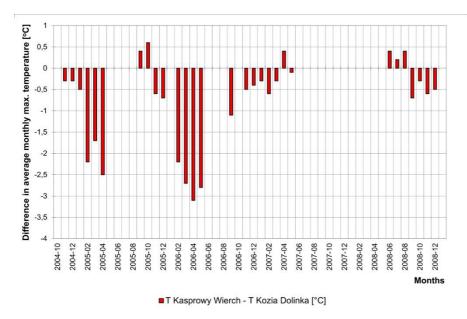


Fig. 10. Difference in average monthly maximum temperature between Kasprowy Wierch and Kozia Dolinka. Negative values occur when the temperature in Kozia Dolinka is higher than on Kasprowy Wierch.

## 5. Discussion

Our analysis of the trend in the average monthly air temperature and the average monthly maximum and minimum temperatures, as well as of periods when snow cover builds up and disappears, has revealed that the Kozia Dolinka cirque is warmer than Kasprowy Wierch for most of the year, except for the period when the snow cover retreats. At such times, the very thick snow cover, formed by snow blown into Kozia Dolinka from rock faces, lasts until June with some snow patches remaining in place until September. By contrast, at the summit of Kasprowy Wierch, where the IMGW-PIB High-Mountain Meteorological Observatory is located, the snow cover is much thinner and disappears faster than in Kozia Dolinka as a result of the snow blowing away. There are no long-lying snow patches on Kasprowy Wierch, which would have a cooling effect on the environment and thus lower the air temperature by absorbing energy for the melting and sublimation of snow. The long duration of the snow cover and snow patches in Kozia Dolinka causes the air temperature to be lower here than on Kasprowy Wierch in late spring and early summer, when the winter snow cover has already melted on Kasprowy Wierch. Kozia Dolinka is cooler than Kasprowy Wierch during the thawing of the winter snow cover. There are situations when fresh snow cover forms after the winter cover has already disappeared, e.g. at the end of May or at the beginning of June. During the thawing of such 'summer' snow cover, Kozia Dolinka remains much cooler than Kasprowy Wierch.

The most substantial differences in average monthly minimum temperature between the stations occur in autumn: in October or November, when higher minimum temperatures are observed in Kozia Dolinka. It is difficult to determine the underlying causation without additional research. Apart from the increased effect of the foehn wind, the most likely reason is the dissipation of heat by the rocky slopes surrounding the Kozia Dolinka valley, which are yet to be covered by an insulating layer of snow cover, whilst the snow cover on Kasprowy Wierch has already been formed.

Surprisingly, the highest temperature differences between Kozia Dolinka and Kasprowy Wierch are characterized in the average monthly maximum temperature. The temperature at the warmest time of the day is crucial for the duration of snow patches in Kozia Dolinka. However, it must be remembered that this is caused by feedback since, on the one hand, the presence of snow patches decreases the temperature in connection with the utilization of energy to melt and sublime the snow, and on the other, lowered temperatures slow down these processes and cause the snow cover to persist. A clear inverse relationship is observable, namely that the persistence of snow cover in Kozia Dolinka when it is absent on Kasprowy Wierch. This usually happens in spring and early summer; as snow cover is formed– an increase in the difference in maximum temperature between the stations and generally in higher maximum temperatures on Kasprowy Wierch are initiated.

Current knowledge of the climate of high-altitude postglacial cirques in the Tatras suggests that the air temperature in such concave, strongly shaded landforms with long-lying snow cover is significantly lower

all year round than the air temperature on convex landforms. This was the conclusion, *inter alia*, of research by Hess (1965). Admittedly, two series of several-day-long measurements in the Kocioł Mięguszowiecki cirque carried out by Kędzia (1993) demonstrated that in some weather situations high-altitude postglacial cirques may be warmer than convex forms, but it seemed unlikely for a concave feature to be warmer than a convex one for over half a year, and even less so in the cold half of the year. That Kasprowy Wierch would be cooler during winter by as much as 0.8°C than Kozia Dolinka seemed even more unlikely. Based on the series of several-year-long measurements used in the present study, which is, unfortunately, incomplete, it is difficult to clearly ascertain the underlying causes. The likely reason is the fact that the station in Kozia Dolinka is situated about 60 m above the bottom of the valley, i.e. above the area where cold air is likely to stand. Another relevant factor could be the location where the air temperature is measured on Kasprowy Wierch, with the thermometers placed on the roof of a two-story building, i.e. about 8 m above the ground. Positioning the thermometers in this way, especially on the top of a mountain, may lower the value of the measured air temperature. Temperature differences may also be caused by natural conditions, including the albedo of snow-covered vertical rock faces and the inflow of warmth from the heated vertical rocks towards the valley. This culminates in small, high-altitude and concave forms to have a higher temperature in winter than unprotected convex forms, namely peaks.

## 6. Conclusions

In the cool half of the year, the IMGW-PIB High-Mountain Meteorological Observatory located on the summit of Kasprowy Wierch records lower thermal indicators than the station in Kozia Dolinka – a small glacial cirque located at a similar altitude, as reflected by the average monthly air temperature and the average monthly maximum and minimum temperatures.

The pattern of average monthly air temperature in the warm season of the year shows a relationship with periods of thawing of winter and seasonal snow cover.

With no additional measurements of the heat balance, standard measurements of air temperatures in high mountains are not sufficient to unambiguously explain the observed patterns. Consequently, there is a need for further and more detailed investigation of the topoclimate of postglacial high-altitude cirques and convex forms, such as peaks and ridges, in order to confirm differences in temperature between these forms and identify the underlying causes. In particular, this applies to summer periods, for which the longest gaps in the data series occurred.

The present study confirms the results of previous research, which has corroborated the presence of conditions conducive to the persistence of permafrost in the Kozia Dolinka cirque. Even though Kozia Dolinka is warmer in the cold season than Kasprowy Wierch, the temperature of the warm season and especially the maximum temperature is the key factor in determining permafrost. In Kozia Dolinka, the impact of air temperature on ground temperature in winter is weakened by the presence of a very thick (several meters thick) snow cover that insulates the ground. In the summer, when permafrost undergoes

ablation, Kozia Dolinka is colder than Kasprowy Wierch, which leads to a conclusion that high altitude postglacial cirques offer more favorable conditions for permafrost than convex forms.

# References

Baumgart-Kotarba M., Kotarba A., 2001a, Deglacjacja Doliny Suchej Wody w Tatrach Wysokich, [in:] Funkcjonowanie geoekosystemów w zróżnicowanych warunkach morfoklimatycznych – monitoring, ochrona, edukacja, A. Karczewski, A.Z. Zwoliński (eds.), Stowarzyszenie Geomorfologów Polskich, Poznań, 73-84.

Baumgart-Kotarba M., Kotarba A., 2001b, Deglaciation in the Sucha Woda and Pańszczyca Valleys in the Polish High Tatras, Studia Geomorfologica Carpatho-Balcanica 35, 7-38.

Dąbrowska K., 2015, Atlas Tatr – Przyroda nieożywiona, TPN, Zakopane, 28 pp.

Dobiński W., 1996a, Poszukiwanie zmarzliny w Tatrach z zastosowaniem metod geofizycznych i analizy klimatycznej, [in:] Osady i formy czwartorzędowe współczesnego i plejstoceńskiego zlodowacenia pólkuli pólnocnej - sympozjum, Poznań, 16-17.

Dobiński W., 1996b, Problem występowania wyspowej zmarzliny w Dolinie Pięciu Stawów Polskich i okolicy w świetle pomiarów temperatury u spodu zimowej pokrywy śnieżnej (BTS), Geographia Studia et dissertationess, 20, Prace Naukowe Uniwersytetu Śląskiego 1552, 15-22.

Dobiński W., 1996c, Występowanie zmarzliny w alpejskim piętrze Tatr Wysokich w świetle badań geofizycznych i analiz klimatycznych, Przyroda Tatrzańskiego Parku Narodowego a Człowiek, 1, Nauki o Ziemi, 140-143.

Gadomski A., 1926, Morfologia glacjalna pólnocnych stoków Wysokich Tatr, Nakład B. Kotuli, Cieszyn, 140 pp.

Gądek B., 2002, Mass circulation of Mięguszowiecki glacieret in the period 1998-1999, [in:] Przemiany Środowiska Przyrodniczego Tatr, Tatrzański Park Narodowy, Polskie Towarzystwo Przyjaciól Nauk o Ziemi Oddział Kraków, Kraków-Zakopane, 71-75.

Gutry-Korycka M., 1967, Temperatura potoków Tatrzańskich o różnych źródłach zasilania, Przegląd Geograficzny, 39 (3), 577-584.

Hess M., 1965, Vertical climatic zones in the Polish Western Carpathians, Zeszyty Naukowe Uniwersytetu Jagiellońskiego, Prace Geograficzne, 11, 268 pp.

IPCC, 2001, Climate Change 2001: The Scientific Basis, [in:] Contribution of the Working Grup I to the Third Assessment Report of the Intergovernmental Panel on Climate Change, J.T. Houghton et al. (eds.), Cambridge University Press, Cambridge, United Kingdom and New York, NY, USA., 881 pp.

IPCC, 2007, Climate Change 2007: The Physical Science Basis, [in:] Contribution of Working Group I to the Fourth Assessment Report of the Intergovernmental Panel on Climate Change, S. Solomon et al. (eds.), Cambridge University Press, Cambridge, United Kingdom and New York, NY, USA, 996 pp.

IPCC, 2013, Climate Change 2013: The Physical Science Basis, [in:] Contribution of Working Group I to the Fifth Assessment Report of the Intergovernmental Panel on Climate Change, T.F. Stocker et al. (eds.), Cambridge University Press, Cambridge, United Kingdom and New York, NY, USA, 1535 pp.

IPCC, 2014, Climate Change 2014: Synthesis Report, [in:] Contribution of Working Groups I, II and III to the Fifth Assessment Report of the Intergovernmental Panel on Climate Change, R.K. Pachauri, L.A. Meyer (eds.), IPCC, Geneva, Switzerland, 151 pp.

IPCC, 2019, Climate Change and Land: an IPCC special report on climate change, desertification, land degradation, sustainable land management, food security, and greenhouse gas fluxes in terrestrial ecosystems, P.R. Shukla, J. Skea, E. Calvo Buendia, V. Masson-Delmotte, H.-O. Pörtner, D. C. Roberts, P. Zhai, R. Slade, S. Connors, R. van Diemen, M. Ferrat, E. Haughey, S. Luz, S. Neogi, M. Pathak, J. Petzold, J. Portugal Pereira, P. Vyas, E. Huntley, K. Kissick, M. Belkacemi, J. Malley (eds.), 864 pp. (in press).

Jania J., 1988, Zrozumieć lodowce, Wydawnictwo Śląsk, 240 pp.

Kędzia S., 1993, Klimatyczne uwarunkowania płatów wiecznego śniegu w Tatrach na przykładzie śnieżnika w Kotle Mięguszowieckim, Uniwersytet Jagielloński, Zakład Klimatologii Instytutu Geografii, Kraków, 69 pp.

Kędzia S., 2004, Klimatyczne i topograficzne uwarunkowania występowania wieloletniej zmarzliny w Tatrach Wysokich (na przykładzie Koziej Dolinki), Ph.D. thesis, Instytut Geografii i Przestrzennego Zagospodarowania Polskiej Akademii Nauk, Warszawa, 124 pp.

Kędzia S., Mościcki J., Wróbel A., 1998, Studies on the occurrence of permafrost in Kozia Valley (The High Tatra Mts.), [in:] Relief, Quaternery Paleogeography and Changes of the Polar Environment, Polar Session, UMCS Lublin, J. Repelewska-Pękalowa, (ed.), 51-57.

Kłapa M., 1963, Prace Stacji Badawczej Instytutu Geografii PAN na Hali Gąsienicowej w latach 1960 i 1961, Przegląd Geograficzny, 35 (2), 221-237.

Kondracki J., 1978, Geografia fizyczna Polski, Państwowe Wydawnictwa Naukowe, Warszawa, 464 pp.

Li J., Sheng Y., Wu J., Feng Z., Ning Z., Hu X., Zhang X., 2016, Landform-related permafrost characteristics in the source area of the Yellow River, eastern Qinghai-Tibet Plateau, Geomorphology, 269, 104-111, DOI: 10.1016/j.geomorph.2016.06.024.

Milata W., 1949, Badania nad polami śnieżnymi w Tatrach, Wierchy, 19, 220-222.

Mościcki J.W., Kędzia S., 2001, Investigation of mountain permafrost in the Kozia Dolinka valley, Tatra Mountains, Poland, Norwegian Journal of Geography, 55 (4), 235-240, DOI: 10.1080/00291950152746586.

Mościcki W.J., 2010a, Temperatura na NE stoku Świnicy i w Koziej Dolince w Tatrach w okresie 2007-2009, [in:] Przyroda Tatrzańskiego Parku Narodowego a Człowiek, Nauki o Ziemi, 1, A. Kotarba (ed), Wydawnictwa Tatrzańskiego Parku Narodowego, Zakopane, 95-102.

Mościcki W.J., 2010b, Temperature regime on northen slopes of Hala Gąsienicowa in the Polish Tatra Mountains and its relationship to permafrost, Studia Geomorphologica Carpatho-Balcanica, 42, 23-40.

Wang S., Sheng Y., Li J., 2018, An estimation of ground ice volumes in permafrost layers in Northeastern Qinghai-Tibet Plateau, China, Chinese Geographical Science, 28 (1), 61-73, DOI: 10.1007/s 11769-018-0932-z.

Wdowiak S., 1959, Współczesne resztkowe lodowce firnowe Wysokich Tatr, Przegląd Geologiczny, 7/8, 375-376.

Wdowiak S., 1961, Contemporary cirque glacier in the Grand Mięguszowiecki Cirque at Morskie Oko Lake in the Tatra Mountains, Biuletyn Geologiczny, 1 (1), 87-92.

Wdowiak S., 1961, Współczesny lodowiec karowy w Wielkim Kotle Mięguszowieckim nad Morskim Okiem w Tatrach, Biuletyn Geologiczny, 1/1, 87-92.

Wiślinscy Z.A., 1991, Lubelscy geografowie badają firn i lód w Tatrach, Tatry, 2, 10-13.

Wiślinscy Z.A., 1993, Tatrzański firn i lód w liczbach, Tatry, 4, 26-28.